



# Stability of viscous sheets in open flow

Claude Perdigou

## ► To cite this version:

Claude Perdigou. Stability of viscous sheets in open flow. Mechanics [physics]. Université Pierre et Marie Curie - Paris VI, 2015. English. NNT : 2015PA066136 . tel-01192979

**HAL Id: tel-01192979**

**<https://theses.hal.science/tel-01192979>**

Submitted on 4 Sep 2015

**HAL** is a multi-disciplinary open access archive for the deposit and dissemination of scientific research documents, whether they are published or not. The documents may come from teaching and research institutions in France or abroad, or from public or private research centers.

L'archive ouverte pluridisciplinaire **HAL**, est destinée au dépôt et à la diffusion de documents scientifiques de niveau recherche, publiés ou non, émanant des établissements d'enseignement et de recherche français ou étrangers, des laboratoires publics ou privés.

# THÈSE

PRÉSENTÉE À

**L'UNIVERSITÉ PIERRE ET MARIE CURIE**

ÉCOLE DOCTORALE : 391 (EDSMAER)

Par **Claude PERDIGOU**

POUR OBTENIR LE GRADE DE

DOCTEUR

SPÉCIALITÉ : MÉCANIQUE

## **Stabilité des nappes visqueuses en écoulement ouvert**

Directeur de thèse : Basile AUDOLY

Soutenance le : 17 Mars 2015

devant la commission d'examen formée de :

M. Olivier DOARÉ, Professeur .....	<u>Rapporteur</u>
M. François GALLAIRE, Assistant professeur .....	<u>Examineur</u>
Mme. Anne JUEL, Professeure .....	<u>Examinatrice</u>
M. Michel POTIER-FERRY, Professeur .....	<u>Rapporteur</u>
M. Neil RIBE, Directeur de recherche .....	<u>Examineur</u>
M. Maurice ROSSI, Directeur de recherche .....	<u>Examineur</u>
M. Basile AUDOLY, Directeur de recherche .....	<u>Directeur de thèse</u>



## Abstract

We consider a vertical sheet made up of a viscous fluid and falling into a bath. This curtain is formed by an inlet injecting viscous fluid at the top of the domain and creating an open flow. The resulting thin structure is falling under the effect of gravity, and develops regions of compressive stress. Those can drive a mechanical instability in the structure as the sheet can buckle under compression, losing its planar geometry and deforming in the out-of-plane direction. We carry a numerical and analytical study of this instability by using tools from both the solid and fluid mechanics fields.

In previous studies, buckling of a viscous sheet that leads to surface wrinkles was associated with flows having a direction of invariance. We will be considering a genuinely two-dimensional stress state. The open nature of the flow imposes that analytical approaches to its stability take into account the advective effects.

We first introduce stability methods on a simple solid mechanics problem, obtaining equations in weak form and using a finite elements solver to obtain its buckled configurations. We will then study both the modelling of the falling curtain as a viscous membrane and its numerical resolution. We will derive a model with kinematics mixing velocities and displacements and use a viscous membrane model. Inspired by the solid mechanics of thin structures it uses the Stokes-Rayleigh analogy to transpose the concepts of stretching and bending stress to viscous flows. Equations for the out-of-plane equilibrium are of high order and require a specific numerical scheme. Capillary effects can be taken into account in the model and we will assess their influence. We finally present a stability analysis hoping to improve our analytical understanding of the buckling phenomenon. We adapt a framework developed for the study of open shear flows instabilities to the out-of-plane equilibrium equations.

**Keywords:** viscous sheet, nonlinear elasticity, weak formulation, buckling, Stokes-Rayleigh analogy, thin structure, wrinkling, finite elements, open shear flows.



## Résumé

Nous étudions un rideau visqueux en écoulement vertical. Un injecteur situé en haut du domaine d'étude forme un écoulement ouvert composé d'un liquide visqueux homogène. Ce fin rideau de liquide s'écoule dans un bain et est accéléré dans son mouvement vertical par l'effet de l'attraction terrestre. Sous l'effet de la gravité, des zones présentant des taux de contrainte compressifs peuvent apparaître au sein de l'écoulement. Le rideau visqueux est alors susceptible de flamber, perdant sa géométrie plane suite à des déplacements orthogonaux au plan de l'écoulement. Nous mènerons une étude numérique et théorique de cette instabilité en flambage d'une membrane visqueuse en faisant appel des outils provenant la fois de la mécanique des solides et de la mécanique des fluides.

Le flambage d'une structure composée d'un liquide visqueux et menant à des fronces ou à des plis a précédemment été étudié dans le contexte d'un écoulement de base présentant une direction d'invariance. Le problème que nous étudions présente un état précontraint purement bidimensionnel. L'étude portant sur un écoulement ouvert, la modélisation théorique de l'état de base comme de l'équilibre de flambage doit prendre en compte les effets advectifs provenant d'une dérivée matérielle.

Nous commencerons par introduire des outils théoriques et numériques que nous appliquons un problème classique de la mécanique des solides. Nous obtiendrons ainsi la formulation faible de l'Elastica d'Euler, qui sera implémentée numériquement en éléments finis. Nous utiliserons ensuite ces mêmes méthodes théoriques et numériques pour le rideau tombant. Nous obtenons un modèle de plaque visqueuse dont la cinématique mélange les vitesses planaires et un déplacement hors du plan. Les termes membranaires sont inspirés de la mécanique des structures fines élastiques et obtenus au travers de l'analogie Stokes-Rayleigh, qui permet de transposer aux écoulements visqueux les notions d'étirement et de flexion d'une plaque. Les équations d'équilibre de l'instabilité de flambage étant d'ordre élevé, nous aurons recours une implémentation numérique particulière. Les effets de la capillarité peuvent être pris en compte dans le modèle et seront étudiés. Nous concluons par une approche théorique de la stabilité de l'écoulement de base obtenu numériquement. Nous adapterons une méthode d'analyse de stabilité des écoulements ouverts instables en cisaillement à l'équilibre de flambage du rideau visqueux.

**Mots-clés :** nappes visqueuses, élasticité non linéaire, formulation faible, flambage, analogie Stokes-Rayleigh, structure fine, plissement, éléments finis, écoulements ouverts en cisaillement.

## Remerciements

Je tiens tout d'abord à remercier Basile Audoly pour son encadrement durant les trois années (et quelques !) de ma thèse. Il a dû, parfois à de nombreuses reprises, m'expliquer patiemment quantité de notions de mécanique des solides, domaine qui m'était étranger au commencement de ma thèse... Grâce à son soutien j'ai pu explorer de nombreux sujets, et il m'a aidé à développer les compétences essentielles au travail de recherche. Découvrir de nouveaux domaines est très enrichissant, mais il m'a aussi appris à aller en profondeur, et à comprendre précisément les différentes thématiques abordées. Sans faire la liste de ces compétences dont il m'aura appris l'importance, je retiendrai tout particulièrement la rigueur qu'il m'a appris à appliquer à ma manière d'écrire du code informatique. Sur ce point, je retiendrai en particulier l'intérêt qu'il a su me transmettre pour les langages fonctionnels, à la syntaxe si puissante et exigeante. Je me dois aussi de mentionner l'élégance mathématique exceptionnelle qu'il sait appliquer à la résolution de problèmes, et dont j'espère continuer à m'inspirer ! Merci !

Je remercie Olivier Doaré et Michel Potier-Ferry d'avoir accepté d'être les rapporteurs de cette thèse, et ce dans des délais relativement courts.

Je remercie de même François Gallaire, Anne Juel, Neil Ribe et Maurice Rossi d'avoir accepté d'être les membres de mon jury de thèse. Remerciements redoublés à Anne Juel, qui a accepté d'assurer la présidence de mon jury.

Je tiens à remercier Patrick Huerre pour sa collaboration extrêmement enrichissante et son expertise de l'analyse de stabilité locale des écoulements ouverts. Son enthousiasme pour notre problème de structure fine et sa capacité à dresser les ponts nécessaires à la communication entre mécaniciens "fluides" et "solides" ont permis des échanges toujours passionnants et constructifs, parfois par-delà l'Atlantique.

Merci aux chercheurs et personnels permanents ainsi qu'aux doctorants de l'Institut avec qui j'ai pu échanger régulièrement durant le déroulement de ma thèse. Joël, vieux loup de mer, ker-skippeur et mandarin de la mécanique. La mafia roumaine, Anca, Diana (pour les enseignements et plus) et Simona (pour tout !) , toujours enthousiastes et attentionnées. Arnaud, amateur de puzzles en mécanique, et pas né de la dernière pluie. Arnaud et Thomas, expérimentateurs en sciences et en arts. Christophe, ministre des affaires étrangères. PYL, aviateur (!!). Corrado et la mafia italienne. Les anciens du bureau 306, Thomas (un Erdős-Bacon-Sabbath de 12, ça impose le respect), Maria-Paola et Bertrand, les nouveaux aussi qui m'y survivront Aurélie (je n'ai cassé aucun de tes échantillons...) et BB (Burger Bro, Bonne Bière, Bad Berkampf). Les voisins du troisième, Zazou la piplette, Etienne le sale nerd, Estelle (et Arthur !) pros du PPP, incroyable Hervé, Claire "l'aventurière" et Omar "Agar" mes co-thsards et les anciens, Diego, Pierre Thomas, Marcello... Les voisins du quatrième, Julieng, Canzhu, Gou', les italiens Valentina, Luca et Andres.

Je remercie particulièrement Djimédo et Stéphane, directeurs de l'ED toujours à l'écoute et très impliqués, malgré la quantité de travail que cela demande ils donnent toujours la priorité à cette mission.

Merci au laboratoire et à mon directeur de thèse de nouveau pour les moyens qui ont été mis à ma disposition, en particulier de m'avoir permis d'assister à plusieurs écoles d'été et conférences. À l'étranger ou à proximité du laboratoire, ce sont toujours des opportunités exceptionnelles scientifiquement, mais aussi humainement et qui m'ont menées à de formidables rencontres, dont une merveilleuse !

J'aimerais remercier toutes les personnes qui m'ont soutenu durant cette thèse, en particulier ma famille, qui a connu l'arrivée de deux adorables nouveaux membres pendant son déroulement, Loréline et Maxime. Je remercie aussi tous mes amis, ceux que je connaissais avant de commencer et ceux que j'ai pu rencontrer au fil de l'eau. Merci aussi aux them colocs Oscar et Charles qui m'ont supporté au quotidien et avec qui nous avons fièrement sorti inSynch.

À ce sujet, je remercie toutes les personnes membres des multiples projets auxquels j'ai participé en parallèle de mon travail de thèse, ces belles années n'auraient pas été les mêmes, ni aussi enrichissantes, sans vous. Dans le désordre, biologie, électronique, jeux vidéos, hacking, médiation scientifique, roller, conférences et j'en passe, que de beaux projets menés à bien et qui me rendent fier.

Enfin, merci Stéphanie, pour ton soutien et pour tout ce que l'on a eu, et aura, la chance de partager.

*We have normality. I repeat, we have normality. Anything you still can't cope with is  
therefore your own problem.*  
*Douglas Adams*



# Contents

Table of contents	xi
Introduction	5
<b>I Euler’s Elastica, the archetypal problem in nonlinear elasticity</b>	<b>5</b>
<b>Euler’s Elastica</b>	<b>7</b>
<b>1 Description of the Elastica</b>	<b>9</b>
1.1 Kinematics . . . . .	9
1.1.1 Assumptions for the linear elastic response . . . . .	9
1.1.2 Nonlinear strain . . . . .	10
1.2 Constitutive laws . . . . .	11
1.2.1 Linear elastic material . . . . .	11
1.2.2 Hyper-elastic materials . . . . .	12
1.3 Weak formulation . . . . .	13
1.4 Boundary conditions . . . . .	15
1.4.1 Natural and kinematic boundary conditions . . . . .	15
1.4.2 Examples of boundary conditions . . . . .	16
1.5 Equilibrium of the Elastica . . . . .	16
1.5.1 Moment balance . . . . .	16
1.5.2 Weak formulation of the Elastica with nonlinear strains . . . . .	17
<b>2 Numerical implementation of the Elastica</b>	<b>19</b>
2.1 Short introduction to the finite element method . . . . .	19
2.1.1 Discretization . . . . .	20
2.1.2 Scheme order . . . . .	20
2.1.3 The <code>libmesh</code> finite elements library . . . . .	21
2.2 First variation . . . . .	22
2.2.1 Base solution . . . . .	22
2.3 Stability analysis by calculation of eigenmodes . . . . .	23
2.3.1 Second variation with base solution . . . . .	23
2.3.2 Eigenvalue problem . . . . .	25
<b>II Stability of a falling viscous curtain</b>	<b>31</b>
<b>Viscous flows and the elastic analogy</b>	<b>33</b>

<b>3</b>	<b>Falling viscous curtain</b>	<b>37</b>
3.1	Glass sheet forming apparatus . . . . .	37
3.1.1	Industrial application and motivation . . . . .	37
3.1.2	Geometry of the curtain . . . . .	38
3.2	Problem definition . . . . .	39
3.2.1	Kinematics . . . . .	40
3.2.2	Constitutive laws . . . . .	43
3.2.3	Kinematic boundary conditions . . . . .	43
3.2.4	Applied volume forces . . . . .	45
3.2.5	Dimensionless quantities . . . . .	46
3.3	Weak formulation . . . . .	47
3.3.1	Strong form of the equations . . . . .	48
3.3.2	Summary of the equations . . . . .	49
3.3.3	Weak form for the base solution . . . . .	50
3.3.4	Linearized weak form for the stability analysis . . . . .	51
<b>4</b>	<b>Numerical implementation</b>	<b>55</b>
4.1	Base planar solution . . . . .	55
4.1.1	Reconstruction of particle trajectories . . . . .	56
4.1.2	Extensional and compressive flow . . . . .	59
4.2	Wrinkled curtain . . . . .	60
4.2.1	Linear stability analysis . . . . .	60
4.2.2	Simplified discontinuous Galerkin method . . . . .	61
4.2.3	Numerical buckling modes . . . . .	61
4.3	Phase diagram . . . . .	64
4.4	Effect of capillarity . . . . .	66
4.4.1	Influence of capillarity on the base solution . . . . .	67
4.4.2	Phase diagram . . . . .	68
<b>III</b>	<b>Open flow instabilities</b>	<b>71</b>
	<b>Open flows and their stability</b>	<b>73</b>
<b>5</b>	<b>Open shear flows instabilities</b>	<b>77</b>
5.1	Method introduction . . . . .	77
5.1.1	Geometry and definitions . . . . .	77
5.1.2	Noise amplifiers and flow oscillators . . . . .	78
5.1.3	Convective and absolute instabilities . . . . .	78
5.1.4	Stream functions and dispersion relation . . . . .	79
5.2	The linear complex Ginzburg-Landau equation . . . . .	80
5.2.1	Temporal framework . . . . .	81
5.2.2	Spatial framework . . . . .	82
5.2.3	Space time analysis . . . . .	84
5.2.4	Method summary . . . . .	85
5.3	Local to global step . . . . .	88
5.3.1	Complex analytical continuation . . . . .	89

<b>6</b>	<b>The falling viscous curtain as an unstable open flow</b>	<b>91</b>
6.1	Local stability analysis of the averaged flow . . . . .	92
6.1.1	Slice averaging of the flow . . . . .	92
6.1.2	Width averaged equation of motion . . . . .	94
6.1.3	Stability analysis: temporal and spatial frameworks . . . . .	95
6.1.4	Stability analysis: spatiotemporal framework . . . . .	97
6.1.5	Phase diagram . . . . .	103
6.2	Local stability analysis of the two-dimensional flow . . . . .	105
6.2.1	Boundary value problem . . . . .	105
6.2.2	Stretched base flow and predicted global mode . . . . .	106
	 <b>Conclusion</b>	 <b>115</b>
	 <b>IV Appendices</b>	 <b>115</b>
	<b>A Program structure of the finite elements solver</b>	<b>117</b>
	<b>B Article draft</b>	<b>119</b>
	 <b>Bibliography</b>	 <b>137</b>



## Notations (1/2)

### General notations

Symbol	Description
$\phi_{,x}$	Derivation of the function $\phi$ with respect to variable $x$
$x', \dot{x}$	(Part I) Spatial and time derivatives (in a 1D problem only)
$\frac{D\phi}{Dt}$	Comoving derivative of function $\phi$
$\hat{x}$	Virtual quantity
$x^{(0)}$	Base solution
$x^{(1)}$	First order perturbation
$\underline{V}$	Vector V
$V_\alpha$	Components of vector V of size 2 (in the two spatial directions $x$ and $y$ )
$\underline{M}$	Matrix M
$M_{\alpha\beta}$	Components of matrix M of dimensions 2*2
$M_{(\alpha\beta)}$	Parentheses denote a symmetrized tensor $M_{(\alpha\beta)} = \frac{1}{2} (M_{\alpha\beta} + M_{\beta\alpha})$
$\delta_{\alpha\beta}$	Kronecker delta
$\underline{a} \cdot \underline{b} = a_\alpha b_\alpha$	Dot product of vectors $\underline{a}$ and $\underline{b}$
$C^k$	Denotes a function with k continuous derivatives
$\text{Re}(a) = a_r,$	Real and imaginary parts of a scalar $a$
$\text{Im}(a) = a_i$	

## Notations (2/2)

### Physical quantities

Symbol	Description
$(x, y, z)$	Directions of space
$k, q$	Wavenumbers (in $x$ and $y$ directions)
$t$	Time
$\omega$	Angular frequency (pulsatance)
$E$	Young's modulus
$\nu$	Poisson's ratio
$\rho$	Volumetric mass density
$g$	Gravity's acceleration
$\gamma$	Surface tension
$\mu$	Viscosity modulus
$h$	Thickness
$(u, w)$	(Part I) Horizontal and vertical displacements
$\delta$	(Part I) Displacement
$(u_x, u_y)$	(Part II) In plane velocities
$H$	(Part II) Out of plane deflection
$\mathcal{E}$	Energy
$W$	Work
$\epsilon$	(Part I) Stretching strain
$\underline{\underline{d}}$	(Part II) Stretching strain rate
$\underline{\underline{N}}$	Stretching stress tensor
$\kappa$	(Part I) Curvature
$\underline{\underline{\dot{K}}}$	(Part II) Bending strain rate
$\underline{\underline{M}}$	Bending stress tensor
$\underline{F}$	Force vector (finite elements)
$\underline{\underline{K}}$	Stiffness matrix (finite elements)
$\psi$	(Part III) Stream function
$\mu$	(Part III) Instability parameter
$c_d$	(Part III) Dispersion coefficient
$D(k, \omega; R)$	(Part III) Dispersion relation between $\omega$ and $k$
$v_\phi$	(Part III) Phase velocity



# Introduction

The inspiration for the viscous sheet problem we study originates from an industrial process developed by two scientists at Corning inc., an American manufacturer of glass and ceramics for the industrial sector. In this method, developed through experiment by Stuart Dockerty and Clint Shay [Doc67], molten glass flows down both sides of a triangular funnel and rejoins at the bottom to form a single sheet of glass. Because the two flows of liquid glass combine perfectly at the bottom of the injector, this method was dubbed the fusion process. Unfortunately for the two inventors, their procedure to form perfectly flat, thin glass with an exterior surface untouched by anything but the atmosphere did not initially find its industrial application. Indeed, by the late 1960s, Corning inc. hoped that this ultra flat glass would become the material of choice in car windshields. But a competitor emerged, a British going by the name of Pilkington who invented at that time the float-glass process, a much cheaper method of making windows, and beat them to the market. Without an application for their process and after this first industrial setback, the two inventors and their research colleagues were left waiting. In the 1980s, the development of LCD displays demanded precisely flat glass, of optical quality and free of alkalis that would contaminate the liquid crystals. These requirements were perfectly met by the combination of Corning's fusion process and some earlier discoveries about how to create thin panels of glass, unaltered by heat and devoid of internal defects. The glass in an LCD panel is typically 0.7 mm thick. By the middle of the 1990s, fusion process glass panels could already be found in a variety of appliances like watches, personal organizers, video cameras, medical imaging devices, aircraft navigation panels, televisions... This process is still in use to this day and was most certainly employed to manufacture the glass screen of the computer or the tablet you may be using to read this manuscript.

Viscous sheet not only have an important role in industrial applications, they are also under study in the context of geophysics. An alternative model to plate tectonics based on viscous plates was developed to account for smaller scale motions of continents that are not well explained by the global scale approach at the origin of plate tectonics. A simplified mechanical model for Earth's crust is to consider a thin shell lying on a thick layer of viscous fluid, the mantle. This kind of model can be used to predict the shape of subduction zones [MBL10], the appearance of a flow in the mantle [RSRvdH07] or the buckling instability of two colliding tectonic plates[SGB<sup>+</sup>10].

The important question motivating the study presented in this PhD work is the stability of the industrial process of glass manufacture exposed earlier. A thin curtain of molten glass is created by a slit permanently injecting fluid, and is falling into a bath (see figures 3.1 and 3.2 p. 38-39). The resulting sheet is accelerated downwards by the effect of gravity, which generates a two-dimensional flow in the plane of the curtain, that in turn gives rise to regions of extensional and compressive stresses. Because the molten glass panel has a very small thickness compared to its spatial extent, it is sensitive to a buckling instability that leads to out-of-plane deformations, thwarting the formation of a flat glass panel. Glass is well known to exhibit a viscosity strongly dependent on the temperature. We can expect the glass panel to cool down as it falls, and thus become less viscous, however we will ignore in our study thermal effects and consider an homogeneous viscosity.

Buckling is often associated to the field of solid mechanics, in which thin structures can undergo very large deformations under relatively small strains, because of the coupling between stretching and bending phenomena. Buckling is a mechanical instability related to the apparition of a new static equilibrium, a beam compressed beyond the buckling threshold has two equilibrium configurations, a straight compressed state, and a buckled configuration displaying lateral deformations. Buckling is much less common in the field of fluid mechanics, in part because thin structures free to deform laterally are not the most common geometries, but mainly because stress doesn't build up as easily in fluids as it does in solids, except for very viscous fluids. There is a fundamental difference between (Newtonian) fluids and (elastic) solids, as a fluid under stress will flow and give rise to velocities while a solid under stress deforms, giving rise to displacements. Buckling of a fluid flow requires an accumulation of stresses on macroscopic time scales, and this is only possible for viscous fluids.

Models describing viscous membranes have been established, and help transpose to viscous fluids notions usually associated with thin elastic structures like plates and shells. By taking into account deformations in stretching and bending, these models are able to predict mechanical instabilities such as buckling for a viscous system. The buckling of a thin viscous structure has been observed in various geometries. One dimensional thin structures like viscous rods are observed to buckle when they fall on a solid surface. Think about a thread of honey falling on a table, it will coil on itself with a certain frequency [Rib04]. Buckling of the rod is due to its own weight and the reaction of the support, this phenomenon was also observed in two-dimensional sheets [SM07] and is called folding, as no coils are formed and the liquid folds on itself. It is also possible to induce compressive stresses in a viscous layer by imposing shear. Shear is the superposition of extensional and compressive stresses in orthogonal directions, this means that if the imposed shear strain rate is large enough, important compressive stresses will develop along one direction of the viscous layer. This has been observed experimentally to lead to buckling in two different geometries. In a cylindrical container counter-rotating walls can be used to create shear, if their velocity is large enough, ripples will appear on the surface of the viscous layer because of buckling [Tay58, BM88]. Parallel counter-moving walls can also be used to generate shear in a viscous layer [STM12], with numerical analysis leading to ripples on the surface. This geometry possesses a longitudinal direction of invariance, while the cylindrical geometry was invariant along the orthoradial direction.

The falling viscous curtain is a two-dimensional structure subject to buckling, with a geometry close to some problems studied in solid mechanics. A thin rectangle of elastic material clamped on its short edges can be forced to buckle by simply stretching it [CRCM02, FRF00]. This very elegant experiment is a manifestation of the Poisson effect, when an elastic material is deformed in a direction, strains also appear in the orthogonal directions. A material with a Poisson ratio of  $\frac{1}{2}$  is incompressible, if stretched in a direction, it will contract in the two other in order to maintain its total volume. In the case of the elastic sheet, clamped boundary conditions on its edges prevents it from contracting and maintaining its volume, thus creating a biaxial state of stress. Transverse stress becomes compressive in the central region of the sheet, which leads to the appearance of wrinkles. Scaling analyses were proposed for this problem, and extensive numerical investigation has taken place [KPF12, Zhe09, NRCH11], however it is not entirely solved to date. Plate buckling problems involving a genuinely two-dimensional distribution of stress are difficult because of their spatial inhomogeneities.

Viscous membrane models are mainly developed in the domain of fluid mechanics,

but the weak formulations they help deriving are particularly adapted to a numerical implementation in finite elements. This numerical method is more common in the field of solid mechanics, and we will adopt this point of view in order to study numerically the global stability of the falling viscous curtain. Note that we will limit our study to a linear global stability analysis that only predicts the onset of the instability because a direct numerical method is not currently available for simulating the dynamics of viscous plates. Current direct numerical schemes [BUAG12] have not yet been through a complete process of validation for viscous plates, and the open nature of the flow makes the simulations harder.

Many specificities related to the fluid mechanical aspect of the falling viscous curtain are still present, and in particular the open nature of the flow. Stability analysis of open flows is an important research topic in fluid mechanics. The classic problem of the flow behind a bluff body such as a cylinder is a good example of the destabilization of a flow because of shear stresses. The corresponding framework was developed by the fluids community [MH82, HM85, BB97] and has been applied to many different configurations, like the wake behind bluff bodies, jets, plumes and splitter plates.

The main matter of this PhD work is the numerical and analytical study of the stability of a falling viscous curtain in open flow. We have just introduced the different methods that we will use to investigate this problem. Fluid and solid mechanics are closely intertwined in the resolution of this system and we will be using methods classically associated with both fields.

We study the stability of a thin viscous layer with an axis of symmetry along the vertical direction. In previous studies, buckling of a viscous sheet that leads to surface wrinkles was associated with flows having a direction of invariance. We will be going further in this matter, as we will be considering a genuinely two-dimensional stress state.

Because viscous membrane models imply the use of comoving derivatives, we will need to take into account its advective part comprising a spatial derivative. Combining this operator with the fourth order equations associated with the bending of thin structures will lead to a stability equation that is fifth order in space. Finite elements implementation of such high order partial differential equations will prove to be a challenge.

The open nature of the flow imposes that analytical approaches to its stability take into account the advective effects. We have seen that a method to study open shear flows instabilities is available, however we will have to adapt it to the instability equations of the falling viscous curtain, driven by compressive stress.

In order to present the different steps of this analysis in an incremental manner, in the first part of this manuscript we will introduce stability methods on a simple solid mechanics problem. We will obtain equations in weak form for Euler's Elastica and use a finite elements solver in order to obtain its buckled configurations. We will proceed in two steps, first obtaining the base solution for a beam under compression, then studying its stability with respect to lateral buckling.

In the second part, we will study both the modelling of the falling curtain as a viscous membrane and its numerical resolution. We will follow the simple road map exposed for the Elastica, even though adapting it to the falling curtain will require substantial efforts due to the more complex geometry and to the underlying viscous constitutive law. The base flow that develops in the falling curtain is driven by gravity and will display

extensional and compressive regions. From this base state, we follow the second step of the numerical analysis and study its stability with respect to out-of-plane displacements.

In the third part, we will use a stability analysis to improve our analytical understanding of the buckling phenomenon observed numerically. Analytical studies also have to incorporate the presence of comoving derivatives, and we will transpose a framework for studying the instabilities of open shear flows to our falling viscous sheet.



**Euler's Elastica, the archetypal  
problem in nonlinear elasticity**





# Euler's Elastica

HUMANITY'S INTEREST in the behaviour of structures is certainly as old as our earliest buildings. Ancient civilizations from around the world have been celebrated for their skill in construction, an ability that is necessarily accompanied by a deep understanding of the mechanics of solids and of chosen materials. Knowing that the impressive skill of our ancient predecessors sometimes still surpass our modern understanding is also quite unsettling.

The way the Egyptians could manage to build the pyramids of Giza is still a topic of debate. How Romans could achieve the construction of the Pantheon in Roma has for very long been a mystery. The engineering skills of the Roman civilization was lost after the fall of the Roman empire, and during the complete duration of the Middle Ages, no one would have been able to reproduce such a feat as the dome of the Pantheon in Roma. For more information on this subject see [MH86].



Figure 1: The dome of the Pantheon in Roma, with a span of  $43.6m$  remains the largest circular dome made of unreinforced concrete. Painting by artist Giovanni Paolo Panini around 1734.

An outstanding phenomenon in the behaviour of structure is buckling. Thin structures, with at least one narrow dimension (e.g. a beam, a sheet), are particularly sensitive

to this effect. Buckling designates the fact that structures under compressive stresses can display large displacements in the direction orthogonal to the applied force. This is quite out of the ordinary, as one expects objects to contract under compressive stresses. In thin structures, contraction is observed until the threshold for buckling is crossed and a displacement in an orthogonal direction occurs, spontaneously breaking symmetry. Buckled systems are very sensitive to additional compression, and display large displacements when subjected to small increments of force.

The simplest example of such a phenomenon can be observed when compressing a beam, this problem was investigated first by Leonhard Euler in the 18th century. It is nowadays known as Euler's Elastica theory, and describes the critical strains leading to buckling for different boundary conditions on a beam.

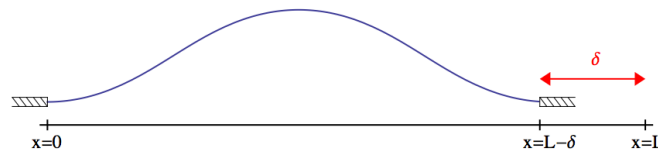


Figure 2: A clamped-clamped beam buckling when its ends are brought closer to each other.

Beams being fundamental parts of many structures, having a quantitative understanding of their behaviour is of course of great interest. In particular, buckling leads to very large displacements, that can often be associated with structural failure. Hence knowing the load that can be applied on a column without it buckling is of tremendous importance in order to avoid a potentially catastrophic collapse of the larger structure built upon it.

From a numerical perspective, and to understand the finite elements method, this problem is also particularly suited, due to its simplicity. Having an analytical prediction for the expected thresholds sets a clear point of comparison for the numerical scheme. Obtaining buckling thresholds and buckled configurations of the Elastica using a finite elements solver is a very simple and efficient way to make sure the numerical set up is accurate and working. After we've made sure that the numerical scheme is correctly set up, we can move on to more complicated problems, for example adding more complicated boundary conditions or additional non linearities.

Euler's Elastica theory predicts different thresholds for buckling depending on boundary conditions. This is an important aspect of the problem, as very often in physics and in mechanics boundary conditions play an important role. Blocking or reinforcing small but well chosen parts of a structure can greatly strengthen its overall resistance or make it fitter for specific applications.

We study the Elastica numerically by implementing the problem in a finite elements library. We will obtain base solutions and both buckling thresholds and buckling modes depending on boundary conditions.

## Contents

---

<b>1.1 Kinematics</b>	<b>9</b>
1.1.1 Assumptions for the linear elastic response	9
1.1.2 Nonlinear strain	10
<b>1.2 Constitutive laws</b>	<b>11</b>
1.2.1 Linear elastic material	11
1.2.2 Hyper-elastic materials	12
<b>1.3 Weak formulation</b>	<b>13</b>
<b>1.4 Boundary conditions</b>	<b>15</b>
1.4.1 Natural and kinematic boundary conditions	15
1.4.2 Examples of boundary conditions	16
<b>1.5 Equilibrium of the Elastica</b>	<b>16</b>
1.5.1 Moment balance	16
1.5.2 Weak formulation of the Elastica with nonlinear strains	17

---

# Description of the Elastica

IN THIS chapter we describe the problem of the Elastica and of its buckling instability by defining the geometry and the energies associated with its deformations. We will establish the kinematics for a slender beam taking into account geometrical nonlinearities. We consider the material composing the beam to be elastic, with linear constitutive relations. The equations governing the deformation and the equilibrium of the Elastica are obtained in weak form by using the principle of virtual work, and we will detail how boundary conditions appear and must be accounted for.

## 1.1 Kinematics

### 1.1.1 Assumptions for the linear elastic response

The study of the Elastica is very fundamental to the mechanics of structures and simplified by the fact that a beam is a one dimensional object. If we use a model that averages strains across the width of the beam, we obtain a one dimensional line with a length along the coordinate  $x$ , and thickness  $h$ . The thickness of the beam is very small, as it is an elongated object we will consider the central line only, and strain gradients in the short vertical directions will give rise to bending terms applied on this line.

The beam is then a linear structure in a two dimensional environment, with possible displacements in only two directions: along the length of the beam or in the transverse

direction. This means that there is always a plane containing the whole length of the deformed beam and that we will not consider 3D torsional modes. The two components of the displacement will be denoted by  $u(x)$  and  $w(x)$ , displacements along and orthogonal to, the length of the beam.  $x$  denotes the horizontal direction, along the length of the beam in its resting configuration, and varies from 0 to 1. An undeformed configuration corresponds to  $u(x) = w(x) = 0$ .

A linear elastic model with linear geometric strains for the beam is not able to capture the buckling phenomenon. In this model, a beam under compression, for example setting  $u(0) = 0$  and  $u(1) = -\delta$  will lead to a homogeneously compressed beam.

$$\begin{aligned}\epsilon_{xx} &= u' \\ \epsilon'_{xx} &= 0 \\ u(0) &= 0 \\ u(1) &= -\delta\end{aligned}$$

With  $\epsilon$  denoting a stretching strain. Solution to this problem is:

$$u(x) = -\delta x$$

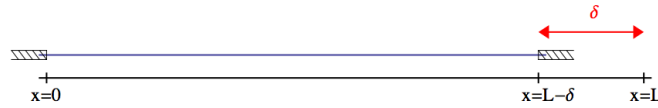


Figure 1.1: A simply compressed beam. The linear model is not sufficient in order to capture the buckling phenomenon.

In order to see a non zero deflection of the beam, one must take into account two important aspects. First, the capacity for the beam to bend must be heeded and we must consider bending energies associated with the displacement  $w(x)$ . Second, the strains must be able to couple horizontal and vertical displacements. Hence the interaction between stretching and bending must appear through a non linear geometric strain definition.

### 1.1.2 Nonlinear strain

In order to write a nonlinear strain definition we have to understand why a displacement orthogonal to the length of the beam is coupled to stretching. Try imagining a beam laying flat on a table, with both ends glued to the table. It is resting at its natural length  $L_0$ . If you pull this beam upwards from its middle point so that it forms an arc, both ends still glued to the table, the length of the beam has necessarily increased, as the length of the arc is longer than the flat length  $L_0$ . Hence the beam is extended by the vertical displacements along its arc length.

At first order, the new length of the beam can be obtained using Pythagoras' theorem and expanding to second order an element of the arc length  $s$ .

$$ds = dx \sqrt{1 + w'^2} \approx dx \left(1 + \frac{1}{2} w'^2\right)$$

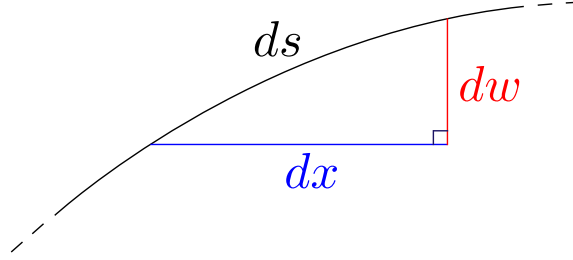


Figure 1.2: Second order approximation leads to a simple expression for the curvilinear coordinate of the beam.

Hence the strain including a non linear geometric coupling between horizontal and vertical displacements is  $\epsilon_{xx} = u' + \frac{1}{2} w'^2$ .

The nonlinearity that was restored is the fundamental ingredient of Föppl-von Kármán equations that describe thin flat plates [AP10], although it is here its one dimensional version. This kind of nonlinear terms correspond to moderate thin structures, e.g. a beam of width  $a$ . The widely recognized success of Föppl-von Kármán's model although it only integrates the lowest order nonlinear term is proof that the geometric coupling between horizontal and vertical displacements is a key element in the description of thin structures.

Additionally to this coupling between displacements through the stretching strain, the bending of the beam must also be taken into account. We define a linear bending strain equal to the curvature of the beam with  $\kappa_{xx} = w''$ .

## 1.2 Constitutive laws

### 1.2.1 Linear elastic material

The buckling of an Elastica is often thought about as involving large displacements, and sometimes failure. This is because the incremental stiffness of the beam goes down a lot after the onset of buckling. This means that in a force-controlled experiment, after crossing the threshold for buckling, the additional force required to move the beam's ends closer together is rather small and will be associated with very large displacements in the buckling direction. Hence an increment of force considered small before buckling can result in important deformations of the beam in the post-buckled domain, possibly leading to failure of the specimen. On the other hand, in a displacement controlled experiment, after reaching the threshold for buckling the required additional force to move beam's ends closer drops sharply.

This means that buckling can be associated with small displacements. Right after the onset of buckling, buckled configurations become stable solutions with small deflections,

and can be reached by using small displacements, or well chosen small force increments. For this reason we can confidently use a linear elastic material description to capture buckling (as long as we stay close to the buckling threshold).

Stretching stress is proportional to stretching strain through a factor that depends on the properties of the material. Two independent material parameters suffice to describe an isotropic linear elastic material and we will use the Young's modulus  $E$  and Poisson's ratio  $\nu$ . Concerning bending stress, in the linear elastic description it is also proportional to the bending strain, with a coefficient involving the same material parameters.

However, the proportionality constants for stretching and bending stresses have very different scalings in the geometrical parameters. In particular elastic energies corresponding to the stretching and bending of thin structures, e.g. a beam of width  $a$ , scale differently with the thickness  $h$ .

$$\mathcal{E}_{Elastic} = \mathcal{E}_{Stretching} + \mathcal{E}_{Bending}$$

$$\begin{aligned} \text{With: } \mathcal{E}_{Stretching} &\propto a h \\ \mathcal{E}_{Bending} &\propto a h^3 \end{aligned}$$

This is the underlying reason why thin structures can display unusually large displacements behaviours like buckling. As the thickness of the structure is reduced, the magnitude of stretching stresses can become much larger than that of bending stresses. When comparing the thickness  $h$  of a beam to its dimensionless length  $L = 1$ , if  $h$  is small ( $h \ll 1$ ) then the scaling  $h^3 \ll h$  makes thin structures adopt bent configurations rather than adapt to constraints through stretching or compression.

Here is the fundamental reason of beam buckling, it is much costlier energetically to deform in compression than to adopt an unstretched, but bent configuration. Structures that do not possess any small dimension compared to others do not have a direction where bending is much easier and will not tend to buckle under small strains.

An interesting practical note can be made here, when building a shelf, if you fear that it won't support the weight you're designing it for, choose a material twice as thick and your shelf will be eight times stiffer!

Here we can stress upon the fact that buckling is a rather universal phenomenon, related only to the geometry of the problem and rather independent of the material.

However, buckling tends to lead to large displacements, and thus to deformed states where material properties have a strong importance. Taking into account nonlinear material properties then becomes of major importance and some possible nonlinear material descriptions are exposed in the following paragraph.

### 1.2.2 Hyper-elastic materials

The study of the post-buckling behaviour and of large deformations requires a finer description for the material properties, for example to know when a brittle material would break.

A wider family of constitutive relations is composed of hyper-elastic materials. These materials derive their constitutive relations from a strain energy density function, which

is a scalar function representing the stored energy of a specific deformed configuration. This family of relations restores an important property of real materials, the fact that large strains lead to a nonlinear response in stress. These nonlinear stress strain relations are able to model the hardening of rubber as it is stretched. Several models have been proposed, based on experimental evidence, or motivated by an analytical prediction of expected properties.

It is important to note that variational models based on the energy cannot describe materials that can plasticize and deform in an irreversible way, or even break. To obtain irreversible and plastic behaviours, a more complicated model must be adopted that records the states of the material along the path of deformation.

In the problems studied in the following we will always consider linear elastic constitutive relations.

### 1.3 Weak formulation

Instead of writing the equations of equilibrium by balancing applied forces and internal stresses, we present here a way of formulating the problem in terms of energy minimization. We write a functional integral that represents the energy of the system, and its minimization in terms of displacements gives the equilibrium configuration.

#### Principle of virtual work

For conservative systems, variational formulations are based on the principle of minimum energy. In a physical system, equilibrium configurations correspond to minima of the energy. The global minimum is always a stable equilibrium.

Applying the principle of minimum energy to a conservative mechanics problem would naturally lead to the principle of virtual work. However, the principle has a wider scope, since the work of a nonconservative action can also be evaluated. In a mechanical system, we can evaluate the work of a force acting on a particle as it moves along a trajectory. If the path is changed, the integrated work won't be the same. By applying all possible virtual displacements, we can evaluate virtual works, and the displacements that minimizes the energy will correspond to the equilibrium configuration.

Fundamentally this description through virtual displacements and virtual work is equivalent to saying the system is at equilibrium. The displacement field obtained corresponds to a stationary virtual work, which means that getting the system in another configuration would require more efforts than it cost to get to the current one. This description is equivalent to the equations of equilibrium.

This formulation for continuum mechanics based on the principle of virtual work is convenient as it defines a weak form that is well adapted for a numerical study. It leads directly to configurations that minimize the energy.

#### Virtual internal work of the Elastica and applied forces

Deformations of an elastic body lead to two kind of energy contributions, one from the stretching of the body and the other from its bending. The virtual work of the system is composed of the virtual internal work ( $\hat{W}_{int}$ ), which is the opposite of the variation of elastic energy, and of the virtual external work ( $\hat{W}_{ext}$ ) linked to external forces acting on the system. Virtual work is evaluated along virtual displacements that represent the



possible movements in the system. These virtual displacements are not any possible movement, but must be kinematically admissible, which means they are in accord with the displacement boundary conditions and the geometry, and are regular functions that can be differentiated to calculate strains. Here a virtual displacement is composed of two components, a virtual horizontal displacement  $\hat{u}$  and a virtual vertical displacement  $\hat{w}$ . In the conservative case, external forces are derived from a potential energy, and we can write the equilibrium:

$$\hat{W}_{int} + \hat{W}_{ext} = -\hat{\mathcal{E}}_{El} - \hat{\mathcal{E}}_{Pot} = 0 \quad (1.1)$$

Where the variation of elastic energy can be expressed as:

$$\hat{\mathcal{E}}_{El} = \int_{\mathcal{L}} (N \hat{\epsilon} + M \hat{\kappa}) ds \quad (1.2)$$

This definition for the variation of elastic energy is very general,  $\hat{\epsilon}$  and  $\hat{\kappa}$  represent the virtual strains and are expressed using the virtual displacements  $\hat{u}$  and  $\hat{w}$ . To obtain their expression we perturb strains with a virtual displacement  $u \rightarrow u + \hat{u}$  and  $w \rightarrow w + \hat{w}$  and keep terms of order 1 in  $(\hat{u}, \hat{w})$ . Recalling the expression for  $\epsilon = u' + \frac{1}{2}w'^2$  and  $\kappa = w''$  we find after perturbation to order 1 that  $\hat{\epsilon} = \hat{u}' + w' \hat{w}'$  and  $\hat{\kappa} = \hat{w}''$ .

Quantities  $N$  and  $M$  represent stresses associated with the virtual stretching and bending strains respectively. In the case of a linear constitutive relation, these are the actual stretching and bending stress tensors, the elastic energy is quadratic  $\mathcal{E}_{El} = \frac{1}{2} E a \epsilon^2 + \frac{1}{2} E I \kappa^2 = \frac{1}{2} N \epsilon + \frac{1}{2} M \kappa$ , with  $N = E a \epsilon$  and  $M = E I \kappa$ . When taking the variation of this quantity, we see that the quantities  $N$  and  $M$  are recovered in the variational form.

Without assuming any specific constitutive relation, let's derive equations in strong form with the nonlinear strains chosen earlier. In order to get those equations, one must integrate by parts the weak form so that virtual displacements in the integral part do not carry derivative orders anymore.

$$\begin{aligned} \hat{\mathcal{E}}_{El} &= \int_{\mathcal{L}} (N \hat{\epsilon} + M \hat{\kappa}) ds \\ &= \int_0^1 (N (\hat{u}' + w' \hat{w}') + M \hat{w}'') ds \end{aligned}$$

Through integration by parts along the length  $\mathcal{L}$  by following the curvilinear abscissa  $s \in [0; 1]$ :

$$\begin{aligned} \hat{\mathcal{E}}_{El} &= [N \hat{u}]_0^1 + [(N w' - M') \hat{w} + M \hat{w}']_0^1 \\ &\quad - \int_0^1 (N' \hat{u} + (N w' - M')' \hat{w}) ds \end{aligned}$$

Integrated terms were written with the convention  $[f \hat{x}]_0^1 = f(1) \hat{x}(1) - f(0) \hat{x}(0)$ . We can identify horizontal and vertical force resultants  $R_x = N$  and  $R_y = N w' - M'$  from the coefficients of  $(\hat{u}, \hat{w})$  in the integrated terms.

The variation of elastic energy becomes:

$$\hat{\mathcal{E}}_{El} = [R_x \hat{u} + R_y \hat{w} + M \hat{w}']_0^1 - \int_0^1 (R'_x \hat{u} + R'_y \hat{w}) ds \quad (1.3)$$

Before writing a system of equations in strong form we want to consider the case of external body forces, we take a general expression for a force per unit length  $\underline{f} = f_u \underline{u} + f_w \underline{w}$ . By definition of the virtual work of an external force,  $\hat{W}_{ext} = \int_{\mathcal{L}} \underline{f} \cdot \underline{\hat{r}} ds = \int_{\mathcal{L}} (f_u \hat{u} + f_w \hat{w}) ds$ . This expression is valid in the case of a body force, constant in the whole volume of the system. With this very general formulation we can write the principle of virtual work:

$$\hat{W}_{int} + \hat{W}_{ext} = - \int_{\mathcal{L}} (N \hat{\epsilon} + M \hat{\kappa} - f_u \hat{u} - f_w \hat{w}) ds = 0 \quad (1.4)$$

Integration by parts leads to a system of equations, called the strong form of the equations. These equations depend on the boundary conditions applied on the system, we will see in the next paragraph that different types of boundary conditions can be applied.

## 1.4 Boundary conditions

When describing a system in terms of energy minimization, boundary conditions do not appear in the weak form. However, they appear when deriving the strong form. We will see that boundary conditions can be of two very different kinds, one of which is implicitly assumed in the weak formulation.

### 1.4.1 Natural and kinematic boundary conditions

We have just seen that the weak form can be used to obtain equilibrium equations, called the strong form of the equations.

During the process of integration by parts, some integrated terms (in brackets) have appeared in equation (1.3) that should not be overlooked, they constitute additional equations, and are part of the strong form description. Those integrated terms involve the boundaries of the domain and actually correspond to the boundary conditions imposed on the system.

When applying the principle of virtual work, those integrated boundary terms are set to zero by the displacement field obtained, and for this reason these boundary terms are called natural boundary conditions. They are explicit equations when studying the strong form of the problem, but are implicitly (naturally) satisfied when applying the principle of least action on the weak form. These boundary terms can very often be identified with Neumann boundary conditions, at least in simple problems.

The natural boundary conditions in the equations obtained earlier at boundaries  $s = 0$  and  $s = L$  impose that  $R_x$ ,  $R_y$  and  $M$  are zero. These boundary conditions describe the fact that no force nor moment are exerted on the extremities of the beam. When choosing only natural boundary conditions, no constraints can hold the beam in position, and the system is only submitted to body forces.

To impose different boundary conditions, one must give specific values to the virtual displacements on the boundaries, which means giving a chosen value to some kinematic quantity. Those boundary conditions are called kinematic boundary conditions, and are additional equations in both the strong and the weak forms of the problem. In simple problems these boundary terms are very often Dirichlet boundary conditions.

### 1.4.2 Examples of boundary conditions

As an example of a kinematic boundary condition let us look at the first integrated term in equation (1.3),  $[R_x \hat{u}]$ . The natural boundary condition on  $R_x$  expresses the absence of any horizontal force on the end of the beam. If we choose a kinematic boundary condition, horizontal displacements on the sides are imposed, which sets the virtual displacement  $\hat{u}$  to zero. For example  $u(0) = 0$ , the beam cannot slide horizontally at its left end, and  $u(1) = \delta$ , the displacement of the beam is prescribed at its right extremity.

In that situation, the absence of boundary conditions on  $w$  will be satisfied with the trivial solution  $w = 0$ , although the boundary condition on  $u$  will impose a non zero horizontal displacement. Hence a simpler form for the weak form describing a compressed beam that cannot buckle could be  $\hat{W}_{int} = \int_{\mathcal{L}} N \hat{u}' ds = \int_{\mathcal{L}} E a u' \hat{u}' ds$ .

Through integration by parts we can identify two equations.  $E a u'' = 0$  is the strong form of the equation and is obtained by cancelling all terms that appear as factors of  $\hat{u}$ . The integrated quantity  $[E a u' \hat{u}]_0^1$  represents a boundary term. If we apply natural boundary conditions, this term is naturally zero for the solution  $u(s) = 0$ . By applying kinematic boundary conditions, e.g.  $u(1) = \delta$  and  $u(0) = 0$ , we find a non zero solution  $u(s) = \delta s$  that satisfies the boundary conditions.

We can also decide to apply a mixed boundary condition by setting kinematically  $u(1) = \delta$  but keeping a natural boundary condition for  $s = 0$ . In that case the boundary equation becomes  $u'(0) \hat{u}(0) = 0$ . The solution  $u(s) = \delta$  satisfies this boundary condition and the strong form of the equation, hence we obtain a rigid body displacement of the whole beam, which is of little physical interest.

We have seen the strong difference between natural and kinematic boundary conditions, and how a problem left completely free at its boundaries is always at equilibrium, in the absence of external loading. It is important to stress out the importance of boundary conditions in a physical problem, as their choice constrains very strongly the solution that will be obtained.

## 1.5 Equilibrium of the Elastica

The complete set of equations in strong form for the Elastica expresses equilibrium equations both in the bulk and at the extremities.

### 1.5.1 Moment balance

The components  $R_x$  and  $R_y$  of the resultant force vector have been naturally defined as the coefficients in integrated terms of  $\hat{u}$  and  $\hat{w}$ .  $R_x = N$  means that the horizontal force that develops is only due to the stretching stress, and bending has no influence on the horizontal balance. The definition of  $R_y$  couples effects of stretching and bending stress, with  $R_y = N w' - M'$ . This equation can be rewritten:

$$\begin{aligned} R_x &= N \\ R_y &= N w' - M' \\ M' + R_y - R_x w' &= 0 \end{aligned}$$

This last equation can be interpreted as a moment balance. If we consider the vector  $\underline{t}(s) = \underline{e}_x + w'(s) \underline{e}_y$  called the local tangent vector, we can write  $R_y - R_x w' = \underline{t} \times \underline{R}$  with  $\times$

the two dimensional vector cross-product. The moment balance becomes  $M' + \underline{t} \times \underline{R} = 0$ . This can be interpreted as the change in bending stress along the beam being equal to the local moment of the resultant force.

### 1.5.2 Weak formulation of the Elastica with nonlinear strains

In the description of the kinematics of the Elastica, we have chosen a nonlinear stretching strain along with linear elastic constitutive relations. With this choice the weak form of the Elastica becomes:

$$\begin{aligned}\hat{W}_{int} &= - \int_{\mathcal{L}} (N \hat{\epsilon} + M \hat{\kappa}) ds \\ &= - \int_{\mathcal{L}} (E a \epsilon \hat{\epsilon} + E I \kappa \hat{\kappa}) ds \\ &= - \int_{\mathcal{L}} \left( E a \left( u' + \frac{1}{2} w'^2 \right) (\hat{u}' + w' \hat{w}') + E I w'' \hat{w}'' \right) ds\end{aligned}$$

The dimensionless version of the virtual internal work can then be expressed as

$$\int_{\mathcal{L}} \left( \left( u' + \frac{w'^2}{2} \right) (\hat{u}' + w' \hat{w}') + h^2 w'' \hat{w}'' \right) ds \quad (1.5)$$

with  $\frac{I}{a} = h^2$  the thickness parameter squared, acting as the bending coefficient. The ratio of the bending and stretching terms is proportional to the thickness squared.

We have obtained this weak form by assuming geometric nonlinearities coupling the horizontal and vertical displacements and a linear elastic constitutive relation for the material. This weak form will be numerically implemented in the next chapter, where we will introduce the finite elements method.



## Contents

---

<b>2.1</b>	<b>Short introduction to the finite element method</b>	<b>19</b>
2.1.1	Discretization . . . . .	20
2.1.2	Scheme order . . . . .	20
2.1.3	The <code>libmesh</code> finite elements library . . . . .	21
<b>2.2</b>	<b>First variation . . . . .</b>	<b>22</b>
2.2.1	Base solution . . . . .	22
<b>2.3</b>	<b>Stability analysis by calculation of eigenmodes .</b>	<b>23</b>
2.3.1	Second variation with base solution . . . . .	23
2.3.2	Eigenvalue problem . . . . .	25

---

# Numerical implementation of the Elastica

WE WILL review in this chapter the different steps required to solve numerically for the equations of the Elastica previously established. After an introduction about the finite elements method, we present the software library chosen for implementation. We will be looking into the details of the resolution in two steps. The first one is to derive the base solution corresponding to a beam under compression because of applied boundary conditions. The second step will lead to the buckling instability of such compressed configurations, and will consist in solving an eigenvalue problem.

## 2.1 Short introduction to the finite element method

The finite elements method is a computational method used to solve partial differential equations that can be applied to complex domains. It is widely used in many fields, as the general method can be applied to any differential equation underlying a physical problem of interest. This is especially true if these equations possess an equivalent variational formulation. The most famous field of application of the method is probably its application to structural analysis, as it is used to predict the behaviour and strength of structures in civil engineering. Dynamical equations can also be simulated, and other famous fields of application are aerodynamics and vehicles crash testing. Many other

fields exploit the power of finite element methods, it is in particular great to solve problems in thermal applications or electromagnetism.

### 2.1.1 Discretization

In finite element methods, the main idea is to discretize problems so that they can be approximated on several small regions, called elements. This idea has a lot of very interesting consequences. First of all, differential equations are local, which means that they can be evaluated on each element only considering a limited number of neighbours. This process of evaluating the values of each term of the equations and assembling those results in a matrix actually transforms a differential equation into a linear algebra problem which usually involves sparse matrices and vectors. This is the origin of a very valuable asset of the method, it is a fast algorithm since computers can solve quickly even very large sparse algebraic systems.

The method has other valuable perks, for example the fact that all elements do not need to be of the same size. This enables for a detailed mesh in geometrically complex or quickly varying regions, but preserves the possibility of using a rather coarse mesh in regular regions, reducing computational cost.

In order to approximate the equations as a combination of local functions, they first have to be expressed in their weak form. It can sometimes be obtained directly through a static equilibrium condition involving the virtual internal and external work, like was presented for the Elastica in §1.3. Starting from the strong form, multiplying by virtual displacements and integrating by parts leads to the weak form. While integrating by parts, the highest derivation order on the unknowns is reduced and partly transferred to the virtual displacements. This means local functions used in the finite element methods have weaker differentiability requirements. In the finite element method solutions can be sought in a space of function having mild regularity requirements and that span only a limited number of neighbours for each element.

Time dependent problems can also be solved, and their discretization leads to systems of ordinary differential equations, that can be solved one time-step at a time. For each time-step the finite elements matrix assembly takes place, and the transient problem can be tackled by using an implicit or an explicit scheme. The whole process is rather fast since the obtained matrix only involves neighbouring elements, and it leads to a large sparse matrix. Only a few terms will be non zero on each line since each element interacts only with a few other. Numerical tools for manipulating large and sparse matrices are very advanced and powerful, and finite element schemes tend to make the most out of them.

In this study, we will not solve any dynamical problem, but will rather be interested in equilibrium configurations. Time dependency will be treated through modal analysis and eigenvalue problems, but we will not run any direct numerical simulation.

### 2.1.2 Scheme order

Choosing a basis of functions for the finite elements analysis is driven by the requirements of the problem. Specifically the geometry of the elements and the continuity requirements of the problem must be taken into account. Standard basis of elements contain  $C^0$  functions having a discontinuous gradient. This means the highest order that functions can carry in the weak form is one.

A weak form involving first order derivatives leads, through the integration by parts process, to a strong form with second derivatives. The strong form of the problem is the best indicator for the continuity requirements of the problem. If the highest derivation order is two, then  $C^0$  elements can be used, as the weak form will contain at most first order derivatives.

When the equations in strong form contain higher order derivatives, elements of higher order must be used. We will see in the following that elasticity can involve fourth order derivatives. In that case, the weak form involves second order derivatives, and one has to use  $C^1$  elements. These elements have continuous first derivatives, while their second order one is only defined inside elements, with possible discontinuities across edges.

In the case of the flat beam that cannot buckle, the weak form used in §1.4.2 only presents first order derivatives. In order to obtain flat solutions with horizontal compression in the beam we can use  $C^0$  elements. However, the complete weak form taking into account bending strains presents second order derivatives on the vertical displacement  $w$ . These correspond to fourth order derivatives in the strong form. In order to obtain buckled solutions for the beam we will use  $C^1$  elements.

### 2.1.3 The libmesh finite elements library

In order to implement numerically the previously obtained equations, we need to make a choice for the finite elements library we are going to use. Several libraries are available but we choose to use the C++ finite elements library libMesh [KPSC06]. This library offers several very useful numerical tools. A major goal of the library is to provide support for adaptive mesh refinement computations that run in parallel. It is built upon powerful and modern tools, using PETSc [BAA+14a, BAA+14b, BGMS97] and SLEPc [HRV05] to handle scientific calculations and more intricate algebra. As open source software, we have control at all levels of the computation, and can adapt the code easily to our specific needs.

libmesh is a very fast library made to handle very complex problems, especially on complicated and large meshes. During my PhD, numerical calculations were done on standard desktop or portable computers, and ran locally. No numerical result shown throughout this manuscript has required the usage of a cluster or paralleling on an external device. This is the advantage of using a finite elements method, as it is a very fast algorithm.

The process of discretization and of defining approximating functions on the elements is handled by the library after the domain's shape and a family of functions have been chosen. In the case of the beam we chose a one dimensional domain that is split equally in the chosen number of elements.

On a 1D grid, the main element types we can choose from are Lagrange and Hermite polynomials. Since we will require the use of  $C^1$  functions when solving for the buckled configuration, we choose a basis of Hermite polynomials. In the case of the flat compressed solution, this choice has no influence on the configurations obtained.

In the following we will describe the different steps required to obtain numerically the solutions of the flat Elastica problem under compression and of the eigenvalue problem associated with its buckled configurations. We will see how each step is implemented in the actual code.



## 2.2 First variation

### 2.2.1 Base solution

In order to obtain a base solution for the compressed beam, i.e. a flat configuration that is not buckled, we set  $w = 0$  in the weak form (1.5). We obtain the simplified weak form  $\int_{\mathcal{L}} E a u' \hat{u}' ds = 0$ .

This weak form when integrated leads to the equation in strong form  $(E a u')' = 0$ , which is of second order. As mentioned earlier, this means we can use  $C^0$  elements to solve this problem. We can choose either Lagrange or Hermite base functions in this case.

The numerical implementation requires to fill in both the force vector  $F$  that contains the internal work and applied body forces (none in this case), and the stiffness matrix  $K$  that contains the gradient of  $F$ .

As we have seen earlier, we have to apply specific boundary conditions to obtain a compressed solution. There are no body forces in this specific example and deformation of the beam is only due to kinematic boundary conditions on its sides.

An element of the stiffness matrix corresponding to the coupling between degrees of freedom  $i$  and  $j$  is denoted  $K_{ij}$ . Degrees of freedom are defined on the nodes of the elements. We use  $C^0$  element having one degree of freedom per node (a  $C^1$  element would require at least two). Hence two degrees of freedom are typically not coupled, unless they belong to the same or to adjacent elements. This is the reason why the stiffness matrix  $\underline{K}$  is sparse.

The value of a basis function at a given node is obtained by using a quadrature rule that defines Gaussian points on each element. The number of Gaussian points per element depends on the degree of the interpolating polynomial, hence a basis of  $C^1$  functions requires a higher number of Gaussian points.

In order to evaluate the quantity  $K_{ij}$ , we need to sum on the Gaussian points  $x_\gamma$  belonging to the elements that contribute to the degrees of freedom  $i$  and  $j$ . Let us call this set of Gaussian points  $\Omega_{(i,j)}$ .

$$K_{ij} = \sum_{x_\gamma \in \Omega_{(i,j)}} E a \Phi_u^1[j][x_\gamma] \Phi_u^1[i][x_\gamma]$$

where  $\Phi_u$  denotes the basis of test and trial functions chosen for the variable  $u$ .  $\Phi_u[i]$  is the function acting at degree of freedom  $i$  and  $\Phi_u[i][gp]$  its value at Gaussian point  $gp$ .

The superscript 1 refers to the derivation order of the function. In the case of a  $C^0$  function basis, this superscript can only take the values 0 and 1, while a  $C^1$  function also has a second order derivative and superscript 2 can be used.

### Boundary conditions

We impose kinematic boundary conditions on both ends of the beam by fixing the left end,  $u(0) = 0$ , so that the beam cannot rigidly move when compressed. We also impose a displacement on the right end  $u(1) = \delta$  that will force the beam to compress.

In the numerical implementation, such a constraint cannot be directly set. However the contribution to  $\underline{K}$  and  $\underline{F}$  of elements located on the extremities is taken care of in a different place of the program, as it is very important to be able to set personalized boundary conditions easily.

A simple way to enforce constraints on some side elements' degrees of freedom is to penalize the difference between their current value and a target value. To that end we will use a large penalization coefficient  $\zeta$ . To impose a zero value to the variable  $u$  on the left boundary, we add the term  $\zeta(u - 0)\hat{u}$  to the vector  $F$  at degrees of freedom laying on the left extremity of the domain  $x = 0$ .

This penalization method sets the value of a variable and corresponds to a kinematic boundary condition. The choice of parameter  $\zeta$  sets the accuracy of the kinematic constraint, a typical value would be  $10^4$ . Changing the value of  $\zeta$  should have no effect on the shape of the obtained solution, otherwise it means the numerical scheme hasn't converged. Extremely large values for  $\zeta$  must also be avoided because it may impact preconditioning and the linear assembly process.

The solution obtained is a linearly compressed beam with  $u(s) = \delta s$ . Note that this solution is valid for both stretched and compressed configurations, depending on the sign of  $\delta$ . Though in the case of compressed solutions, it is unstable in buckling, and a stability analysis can lead to buckled solutions. In the case of stretching, our linear elastic model wouldn't be valid for large displacements either, as material nonlinearity should be taken into account.

## 2.3 Stability analysis by calculation of eigenmodes

Now that we have obtained the base compressed solution we need to find the threshold for buckling. To study the buckling instability we have to restore terms corresponding to out-of-plane displacements  $w$ . This means we have to take into account the non linear displacements, as well as the bending energy.

We will study the stability of the compressed beam with respect to out of plane displacements. We expect the beam to buckle when the stretching energy becomes of the order of the bending energy stored in a buckled configuration. This means the critical compression  $\delta_c$  at which the beam will buckle only depends on its bending stiffness  $h^2$ .

In addition to the bending terms, we will add inertial terms in order to be able to study the linear stability analysis. Terms of the form  $\rho(u_{,tt} + w_{,tt})$  are added to the weak form as we want to predict a growth rate for the buckling mode, and thus formulate a dynamic problem.

The complete weak form is the same as equation (1.5) with additional inertial terms.

$$\int_{\mathcal{L}} \left( u' + \frac{w'^2}{2} \right) (\hat{u}' + w' \hat{w}') + h^2 w'' \hat{w}'' + \rho u_{,tt} \hat{u} + \rho w_{,tt} \hat{w} \quad (2.1)$$

We now seek solutions with non zero values for  $w$ , and have two independent variables. We will see that using the flat compressed beam as a base solution will lead to two uncoupled problems on the virtual displacements  $\hat{u}$  and  $\hat{w}$ .

### 2.3.1 Second variation with base solution

We now consider the flat compressed beam with displacements only in the horizontal direction as a base solution. This base solution will be denoted by  $u^{(0)} = \delta s$  and  $w^{(0)} = 0$ . We perturb this base solution with displacements  $u^{(1)}$  and  $w^{(1)}$  and insert them in the weak form of the equations.

$$\int (u'^{(0)} + u'^{(1)} + \frac{1}{2}(w'^{(0)} + w'^{(1)})^2) (\hat{u}' + (w'^{(0)} + w'^{(1)}) \hat{w}') + h^2 (w''^{(0)} + w''^{(1)}) \hat{w}'' \quad (2.2)$$

Since  $u^{(0)}$  and  $w^{(0)}$  are independent of time  $t$ ,  $\ddot{u}^{(0)} = 0$ . After restoring inertial terms in the previous equation and developing to first order in  $u^{(1)}$  and  $w^{(1)}$  we obtain:

$$\int \rho \ddot{u}^{(1)} \hat{u} + u'^{(1)} \hat{u}' + \rho \ddot{w}^{(1)} \hat{w} + u'^{(0)} w'^{(1)} \hat{w}' + h^2 w''^{(1)} \hat{w}'' \quad (2.3)$$

From the weak form, we can identify two independent problems, each associated with one virtual displacement  $\hat{u}$  or  $\hat{w}$ .

The first problem on virtual displacement  $\hat{u}$  contains the terms  $\int \rho \ddot{u}^{(1)} \hat{u} + u'^{(1)} \hat{u}'$ . Boundary conditions for the variable  $u$  are unchanged.  $u(0) = u^{(0)}(0) + u^{(1)}(0) = 0$  and  $u(1) = u^{(0)}(1) + u^{(1)}(1) = \delta$ . Since  $u^{(0)}$  is the base solution and it already verifies those kinematic boundary conditions, they become  $u^{(1)}(0) = u^{(1)}(1) = 0$ . With those boundary conditions at each extremity of the beam, the weak form that implies the virtual displacement  $u$  only admits the obvious null solution. This means that the buckled configurations share the same horizontal displacements  $u$  as the base solution. Buckling is only associated with an out of plane motion with material elements staying on the same vertical axis.

The second problem is on the out of plane virtual displacement  $\hat{w}$ . It involves the terms  $\int \rho \ddot{w}^{(1)} \hat{w} + u'^{(0)} w'^{(1)} \hat{w}' + h^2 w''^{(1)} \hat{w}''$ . Here we can see that the weak form depends on the base solution, that appears through the term  $u'^{(0)} w'^{(1)} \hat{w}'$ . We obtained the solution  $u(s) = \delta s$ , hence this term becomes  $\delta w'^{(1)} \hat{w}'$ , where  $\delta$  is the pre-stress with  $Ea = 1$ . This problem accepts nonzero solutions depending on the choice of boundary conditions. The different possibilities can be summarized in the following table:




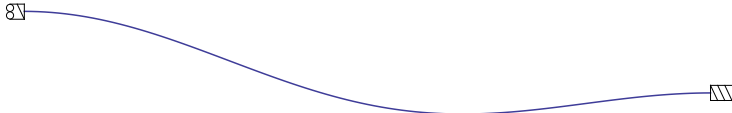
Boundary type	s=0	s=1	Expected shape
Pinned	$w=0$	$w=0$	
Clamped	$w=0$ $w'=0$	$w=0$ $w'=0$	
Mixed example	$w=0$	$w=0$ $w'=0$	
Uneven example	$w'=0$	$w=0$ $w'=0$	

Table 2.1: Different kinematic boundary conditions lead to different buckling configurations for the Elastica. Expected shape are solutions computed with  $\delta = -0.04$ .

Solutions displayed here are obtained by solving an eigenvalue problem and are an anticipation of the following paragraph.

### 2.3.2 Eigenvalue problem

We use a linear stability analysis by inserting time growing modes of the form  $A \Phi(x) e^{-i\omega t}$ , where  $\Phi(x)$  is the shape of the adopted eigenmode,  $i$  the unit imaginary number and  $i\omega$  the eigenvalue. If the growth rate  $\text{Im}(\omega) > 0$  the real part of the exponential's argument is positive and we have identified an unstable, time growing mode.

#### Strong form and analytical solution

By integrating by parts  $\int \rho \ddot{w}^{(1)} \hat{w} + \delta w'^{(1)} \hat{w}' + h^2 w''^{(1)} \hat{w}''$  in order to remove derivation orders on the virtual displacement  $\hat{w}$  and exhibit the strong form, we obtain the equation  $\rho \ddot{w}^{(1)} - \delta w''^{(1)} + h^2 w''''^{(1)} = 0$

We choose pinned boundary conditions for the vertical displacement, that allow  $w'$  to take nonzero values at the extremities. We inject a solution with the shape  $w(x) = A e^{i(kx - \omega t)}$  as we are searching for time growing periodic solutions, and the equation becomes:

$$\begin{aligned} -\rho \omega^2 + \delta k^2 + h^2 k^4 &= 0 \\ \omega^2 &= \frac{k^2}{\rho} (\delta + h^2 k^2) \end{aligned}$$

We are looking for a time growing mode, hence we require that  $\omega$  has a positive imaginary part.  $\omega$  is imaginary if  $\omega^2 < 0$ , we thus require  $k^2 (\delta + h^2 k^2) \leq 0$ . For real values of  $k$  this is equivalent to  $h^2 k^2 \leq -\delta$ . Since  $\delta$  is a compression, it is a negative number and the inequality has solutions. However boundary conditions have to be taken into account and we choose  $w(0) = w(L) = 0$ , the beam at equilibrium is resting on a horizontal support. Hence  $A e^{i k 0} e^{-i \frac{\pi}{2}} = A e^{i k L} e^{-i \frac{\pi}{2}} = 0$ . We have added a phase to the solution so that the first boundary condition is always verified and we don't consider null solutions, the right boundary condition leads to  $A \cos(kL - \frac{\pi}{2}) = A \sin(kL) = 0$ . Once again, ignoring null solutions we obtain the condition  $\sin(kL) = 0 \Leftrightarrow kL = 0 \bmod \pi \Leftrightarrow k = \frac{n\pi}{L}$ ,  $n \in \mathbb{N}$ .

The smallest possible value for  $k$  is obtained for  $n = 1$  and the previous inequality becomes  $-\delta \geq \frac{h^2 n^2 \pi^2}{L^2}$ . This is the buckling threshold of the beam, when compression  $\delta$  is large enough, a compressed and flat solution becomes unstable, and the beam adopts a buckled configuration. We can plot the eigenvalue  $\omega^2$  for each possible value of the wavenumber  $k$  as a function of  $\delta$  and spot the instability threshold when it becomes negative.

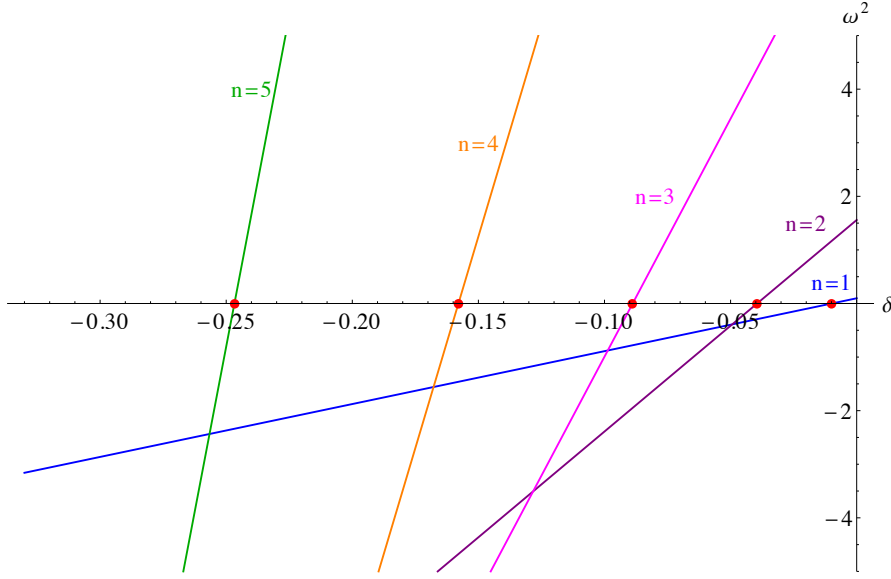


Figure 2.1: Eigenvalue squared  $\omega^2$  as a function of compression  $\delta$ ,  $\omega^2 = \frac{n^2 \pi^2}{\rho L^2} (\delta + \frac{h^2 n^2 \pi^2}{L^2})$ . The beam is pinned at both extremities, with imposed horizontal displacements  $u(0) = 0$  and  $u(L) = \delta$ . This graph was plotted with  $h^2 = 10^{-3}$ ,  $L = 1$ ,  $\rho = 1$ . For small absolute values of the compression  $\delta$  the compressed flat solution is stable. As soon as  $\delta$  becomes large enough,  $\omega^2$  becomes negative, the growth rate  $Im(\omega)$  of the mode corresponding to  $n = 1$  becomes positive and the beam adopts a buckled configuration. Red dots on the horizontal axis are placed at the value obtained earlier for the stability threshold of modes  $n \in \llbracket 1, 5 \rrbracket$ ,  $\delta_n = \frac{h^2 n^2 \pi^2}{L^2}$

### Weak form and numerical implementation

To solve numerically the eigenvalue problem on the vertical displacement  $w$ , we will write the equivalent generalized eigenvalue problem, by choosing a more generic form  $w^{(1)}(s) = W(s) e^{-i\omega t}$ . The spatial dependence is a general function, that will be determined by the eigensolver algorithm. With this choice the weak form becomes  $\int -\rho \omega^2 W \hat{W} + u^{(0)} W' \hat{W}' + h^2 W'' \hat{W}'' = 0$ .

With the eigenvector  $W(s)$  acting as the new unknown function. The finite element discretization process decomposes the unknown on a basis of function, with contributions at each degree of freedom of  $W$ . If we denote by  $X$  the eigenvector in its discretized version the previous weak form can be written in the compact form  $A X = \lambda B X$ . This equation denotes a generalized eigenvalue problem. In our case, the eigenvalue  $\lambda$  is equal to  $\rho \omega^2$ , and the matrix  $B$  contains the contributions of all the inertial terms. This matrix is not empty because we previously added time dependence and an inertial term, with the objective of having  $\lambda \propto \omega^2$  appear in the weak form. The matrix  $A$  contains all other contributions, i.e. it is an operator corresponding to the terms  $\int u^{(0)} W' \hat{W}' + h^2 W'' \hat{W}''$ .

We use the finite elements library in order to assemble the matrices  $A$  and  $B$ , that can then directly be fed into a eigenvalue solver, in our case SLEPc. The solver requires several parameters to be set, as well as the type of eigenvalue problem. Numerical methods for eigenvalue problems are classified based on the structure of matrices  $A$  and  $B$ . If matrices  $A$  and  $B$  are both symmetric, the problem is called Hermitian. If the

matrix  $B$  isn't the identity, then the eigenvalue problem is called generalized. In that case, one possibility is to invert this matrix in order to write  $B^{-1} A X = \lambda X$ , which is an usual (non-generalized) eigenvalue problem for matrix  $B^{-1} A$ . However numerical methods try to avoid inverting this matrix as it is a costly operation, and can use other methods like preconditioners.

Assembling matrices  $A$  and  $B$  is very similar to the process involved in assembling matrix  $\underline{K}$  described in §2.2.1.  $A$  is called the stiffness matrix, while  $B$  is called the mass matrix. Since terms of the equation couple the same derivative order for  $W$  and  $\hat{W}$ , these two matrices only involve symmetric terms, and the problem under study is Hermitian.

Additionally,  $B$  contains the contribution of the term  $\int W \hat{W}$  and is not the identity. This is a generalized eigenvalue problem. It is worth noting that this inertial term has no influence on the values for the stability threshold we will obtain, since we choose  $\rho = 1$ . However we will not replace  $B$  with the identity in order to implement a generalized eigenvalue problem and use its associated numerical methods.

Kinematic boundary conditions are handled in a slightly different way compared to the base solution's finite element assembly. Here we proceed by setting directly degrees of freedom to a specific value. If we call  $x_i$  a degree of freedom we want to set to 0, we have to make sure the equation  $x_i = 0$  appears in  $A X = \lambda B X$ . Hence we find that setting  $A_{ij} = A_{ji} = 0 \forall j$  and  $B_{ij} = B_{ji} = \delta_{ij} \forall j$  leads to line  $i$  of the equation fixing a kinematic boundary condition. This step is taken after assembly of the matrices  $A$  and  $B$ , we thus replace directly all lines and columns associated with a degree of freedom under kinematic constraint.

Once matrices are assembled, and kinematic boundary conditions have been taken care of, the generalized eigenvalue solver returns eigenvalues and eigenvectors associated with the problem.

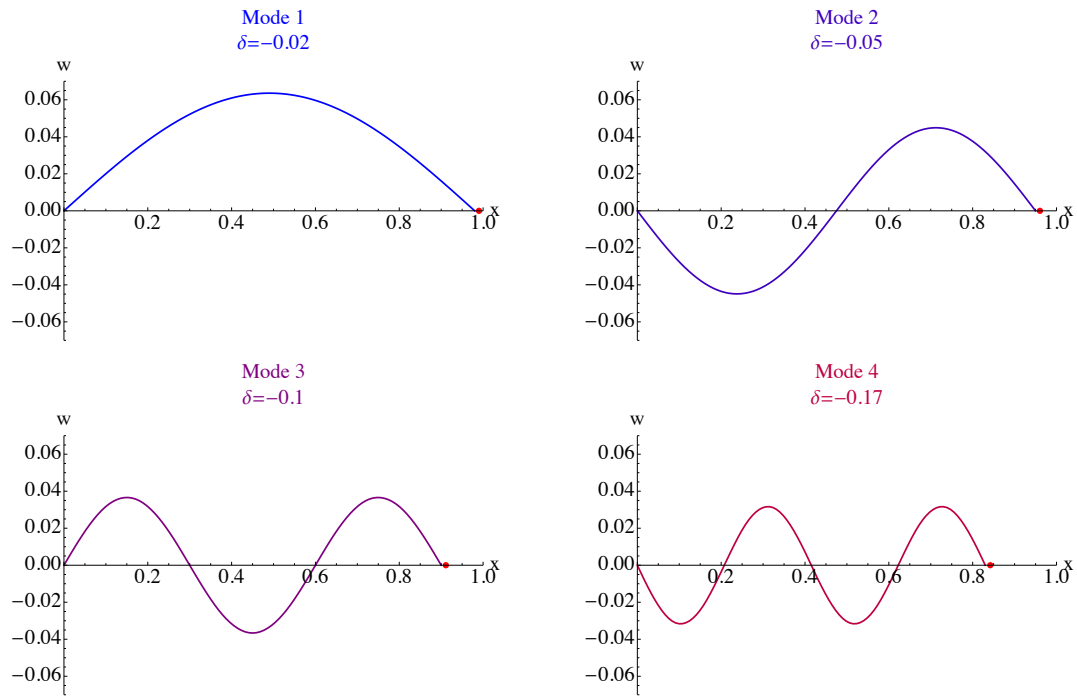


Figure 2.2: First buckling modes of the Elastica with the corresponding chosen values for the compression  $\delta$ . These buckled solutions were obtained by calculating the eigenmodes of a compressed base solution, as described in this chapter. Red dots indicate the static instability threshold of the corresponding mode.

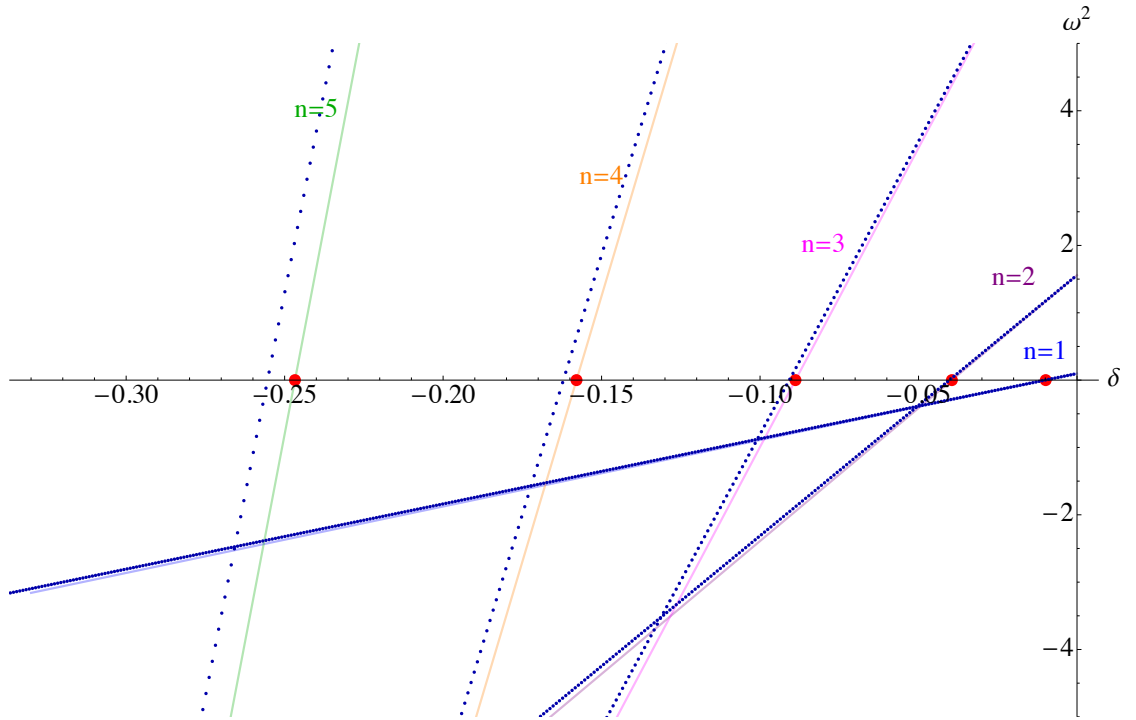


Figure 2.3: Numerical results for the eigenvalue problem corresponding to an Elastica with pinned-pinned boundary conditions (see table 2.1). Blue dots are the eigenvalues obtained numerically as a function of  $\delta$ , the displacement boundary condition imposed on the flat beam base solution. Numerical results (dots) are superimposed on the analytical results (solid lines) already presented in figure 2.1. The discrepancy observed between the numerical and analytical study for higher order modes can be attributed to the small number of elements used for discretization of the eigenvalue problem  $N = 10$ .







# **Stability of a falling viscous curtain**



# Viscous flows and the elastic analogy

THE FALLING viscous sheet we will study is a thin structure made up of a viscous fluid. Buckling is usually associated with thin elastic structures in solid mechanics, however a viscous fluid is able to build up stresses that can lead to a mechanical instability. This has been studied in the past and we are going to review the history of this domain.

In an experiment led by Taylor [Tay58], a circular spinning plate is completely immersed in a thin layer of a viscous fluid that floats on a less viscous and denser fluid. The spinning plate drags the surrounding fluid in its rotation, with small friction at interfaces, since both air and the supporting liquid have small viscosities. When the plate is spinning fast enough, he notices the formation of waves of small amplitude at the surface of the viscous layer, close to the edges of the spinning disk. Next to the spinning plate, liquid is dragged at a certain velocity, while far from the disk (near the enclosing cylindrical container) liquid is at rest. Hence shear stress develops next to the spinning plate. Since shear can be decomposed as stretching and compression in two orthogonal directions, the stress along the compressive directions can lead to buckling when it becomes large enough, i.e. when the plate is spinning fast enough. A theoretical investigation of buckling in visco-elastic layers was first carried out by [Ram63] [Bio64], as a possible model for the deformation of earth's crust. The next important addition to the study of the viscous buckling of thin layers is due to [SM81]. The authors study a viscous liquid layer floating on a denser liquid, similarly to Taylor's experiment previously described, but this time in a "Couette" configuration. The liquids are constrained between a stationary central cylinder and a larger rotating cylinder. When rotating the outer cylinder, the difference of velocity between the inner and outer boundaries develops a shear flow of orthoradial symmetry. The surface of the viscous fluid remains flat for lower values of angular velocities, a region where shear stress is proportional to the shear velocity. They find that in their setup, stability is lost when the dimensionless shear stress reaches a certain value, at which point the surface of the fluid starts displaying waves due to a buckling phenomenon.

A theoretical and experimental investigation by [BM88] in the same geometry was published in 2006. In this work they confirm the empiric law obtained by [SM81] with a theoretical argument. Their model is an adaptation of the theory of thin elastic plates perturbed from a planar state, without any membrane approximation. It successfully predicts that ripples should appear on the surface at an angle of  $45^\circ$  from the central cylinder, which is the principal direction of compression. Experiments involving viscous fluids with no significant non Newtonian behaviour were found to display good agreement with the theory.

These cylindrical geometries all feature an orthoradial symmetry. Other systems with very different geometries have also been studied. When a long strip of paper is allowed to fall vertically on a tabletop, it will fold on itself [LSK78] [MK99] in a regular pattern. This is explained by the buckling of the lower part of the strip that touches the table. A similar problem involving viscous sheets or threads can also be

studied. The first experimental evidence was brought to the attention of the scientific community by [Bar58]. Although it is a very common experiment, that some people may be running every morning when pouring honey on their bread, it also has a lot of industrial applications, and attracted the attention of investigators in a large measure. The first theoretical work on the subject is due to [TYR93], and further experimental studies were led by [GT88], with a geophysical motivation.

Later on [SM07] defined more clearly the analytical problem and led some initial numerical and experimental studies. In 2002, [Rib02] establishes a more sophisticated model for the deformation of thin viscous sheets, by taking into account their finite thickness and bending moments. In a paper published in 2012 and its accompanying commentary [Rib12], authors study the problem of an infinitely long plate under shear constraints. Authors find several different modes for the shape of the buckled pattern, with waves aligning with the most compressive direction.

In all these problems, strong symmetries let authors define a homogeneous base state with a direction of invariance (orthoradial or along a straight axis). In our study, we will consider a pre-buckled state with strong spatial dependence in two dimensions, displaying both extensional and compressive regions.

Here we will present a review of the phenomenon known as wrinkling. Closely related to buckling, it occurs if an additional mechanism is limiting the stretching of the medium, like in the case of an Elastica on an elastic foundation, and leads to shorter wavelength buckling modes, whence the formation of wrinkles. We will later observe that the falling viscous curtain we study buckles in modes of shorter wavelength than the fundamental buckling mode that could be *a priori* expected.

Wrinkled elastic membranes are very interesting for engineering applications, and as such have been studied extensively. Originally the analysis of membranes was carried out using tension field theory, e.g. gravity induced wrinkles in variously shaped membranes in [Man81]. Tension field theory assumes a two dimensional continuum with negligible bending stiffness, featuring no compression, and focuses its study on tension lines between elements.

The fact that compressive stresses can lead to buckling is very well known, but an original way of inducing those stresses was experimentally displayed in [CRCM02], and previously studied by [FRF00]. By stretching a rectangular elastic sheet clamped on its short edges, wrinkles appear along the width of the sheet. The clamps prevent transverse contraction due to Poisson's effect and compressive stress appears in the transverse direction. These stresses are relaxed through buckling that leads to wrinkles. By assuming a homogeneously compressed state and an ansatz constraint equation that relates the buckled sheet shape's and its compressive state, they are able to predict scaling laws for the wavelength and the amplitude of the wrinkles. The wavelength is set by the competition between the bending and elastic stiffness. The amplitude is obtained through a competition of the compressive strain and the width of the elastic sheet.

Additionally to those that appeared in [FRF00], significant numerical results were obtained for wrinkled membranes a few years later, notably by [KPF12] [Zhe09] [NRCH11]. In [PDF11], authors define a weaker constraint as their ansatz, which leads to a better analytical understanding of the wrinkling of stretched thin sheets, in the context of a small slope approximation. One of their notable result in the context of our study is the evidence that longer sheets display a smaller number of wrinkles.

In a shortly following article from [KPF12], the authors are able to relax the small slope approximation in their numerical experiments. They find that sheets always display

an even number of wrinkles, which is also the case of our symmetric buckled solutions. The authors provide an interesting discussion about the role of a constraint ansatz. By establishing a relationship between the length of the buckled mode and the amount of compression, this constraint forces the system to explore wrinkled configurations. Without this constraint, the assumed homogeneous base solution would be stable. Assuming this link between the wavelength of the wrinkles and the amount of compression is necessary, and originally made by [CRCM02] because of the lack for an analytical solution describing the pre-buckled state. The authors of [KPF12] also reference [FRFW00] as taking into account an inhomogeneous pre-buckled state in their discussion of the so-called "towel buckling". The authors of [FRFW00] express the wrinkles as a cosine with a strong decaying amplitude towards free edges. It can be noted that their numerical solution has a very short wavelength and displays nine wrinkles. This can be explained by the fact that their system of interest is a slight variation on the previously described problem. Experimental investigation carried out by [Zhe09] as well as the numerical results obtained, and numerical results from [NRCH11] all display strong resemblance to the results obtained in the case of our study.

Going back to the falling viscous curtain problem, we are interested in the buckling of a viscous fluid. Buckling is usually rather associated with solid mechanics, we will see in the following that it is possible to draw an analogy between the equations of linear elasticity and the equations associated with viscous flows.

When studying a very viscous flow, a situation corresponding to small Reynolds numbers, some terms of the Navier-Stokes equations can be dropped. Ignoring inertial and advective terms, Stokes equation is used to model viscous flows.

In the context of viscous flows, one can use the Stokes-Rayleigh analogy, which relates Stokes equation with the equations of linear elasticity. The relation between strain rate and the velocities in the fluid is analogous to the linear elastic definition of strains as a function of displacements in a solid. In a similar fashion, the viscous modulus relates strain rate with stress in a proportional manner. This is analogous to the relation between elastic stress and elastic strains in the case of a linear constitutive relation.

A simple demonstration of this analogy can be performed on the Stokes equation, which is obtained by linearizing the steady state Navier-Stokes equation:

$$\nabla \cdot \underline{\underline{\mathbf{C}}} + \underline{\underline{f}} = 0 \quad (2.4)$$

where  $\underline{\underline{\mathbf{C}}}$  is the Cauchy stress tensor and  $\underline{\underline{f}}$  denotes body forces.

The constitutive relation for a viscous fluid is  $\underline{\underline{\mathbf{C}}} = \frac{\mu}{2}(\nabla \underline{\underline{u}} + \nabla \underline{\underline{u}}^T) + \mu \text{Tr}(\nabla \underline{\underline{u}})$  for the 2D case, and the applied body force is  $\underline{\underline{f}} = \rho \underline{\underline{g}}$ .

Hence Stokes equation is equivalent to a linear elastic model applied to the velocities in the flow. Elastic moduli must be replaced by the viscous ones, and kinematic boundary conditions must be retained and applied to velocities. When solving these equations for a steady laminar viscous flow, one must remember that the analogy draws a similarity between displacements (a length) in the case of elastic solids and velocities (a length per unit time) in the case of viscous liquids. This additional time dimension has no effect when solving the linear equations, but one must remain very careful when using those results for further study, as time derivatives and advective effects become of importance.

The study presented in the following is based on preliminary work by G. Pfingstag, A. Boudaoud and B. Audoly, preceding the beginning of this PhD work. We promptly had to alter the model in use by taking into account advective effects, which led us to new

kinematics and a new set of stability equations. The linear study could not be solved efficiently at the time, and by making a fresh start and using tools like finite elements solving we also improved on that matter.

## Contents

---

<b>3.1 Glass sheet forming apparatus . . . . .</b>	<b>37</b>
3.1.1 Industrial application and motivation . . . . .	37
3.1.2 Geometry of the curtain . . . . .	38
<b>3.2 Problem definition . . . . .</b>	<b>39</b>
3.2.1 Kinematics . . . . .	40
3.2.2 Constitutive laws . . . . .	43
3.2.3 Kinematic boundary conditions . . . . .	43
3.2.4 Applied volume forces . . . . .	45
3.2.5 Dimensionless quantities . . . . .	46
<b>3.3 Weak formulation . . . . .</b>	<b>47</b>
3.3.1 Strong form of the equations . . . . .	48
3.3.2 Summary of the equations . . . . .	49
3.3.3 Weak form for the base solution . . . . .	50
3.3.4 Linearized weak form for the stability analysis . . . . .	51

---

# Falling viscous curtain

IN THIS section we will describe the geometry of the problem under study. The inspiration for this problem originates from a process of the glass industry as will be described in §3.1. We will define the geometry and the kinematics of the problem, and will solve it using the same method as described in the first part of this manuscript about the Elastica. We will show that various differences arise making the study more difficult in several aspects and will propose solutions to tackle those problems.

## 3.1 Glass sheet forming apparatus

### 3.1.1 Industrial application and motivation

We study a thin sheet of viscous fluid in a vertical geometry. The fluid is injected by a slit situated at the top of the domain, which forms a liquid curtain that flows down. The viscous fluid is further accelerated by the effect of gravity as it falls down vertically.

This geometry is motivated by an industrial process from the glass making industry. Following a first patent deposited in 1964, Corning Inc. still uses an apparatus to form glass sheets in a vertical free fall configuration. Molten glass is injected in a triangular gutter that overflows with the viscous liquid. The overflowing fluid sticks to the outer part of the gutter and joins at its bottom. The stationary injection process thus creates a constant thickness curtain of viscous fluid that falls down forming a rather wide, but thin sheet of glass. This process is still used to date, especially to make various electronics



appliances screens, as the finished surface is very smooth since the glass doesn't contact any mechanical part while setting.

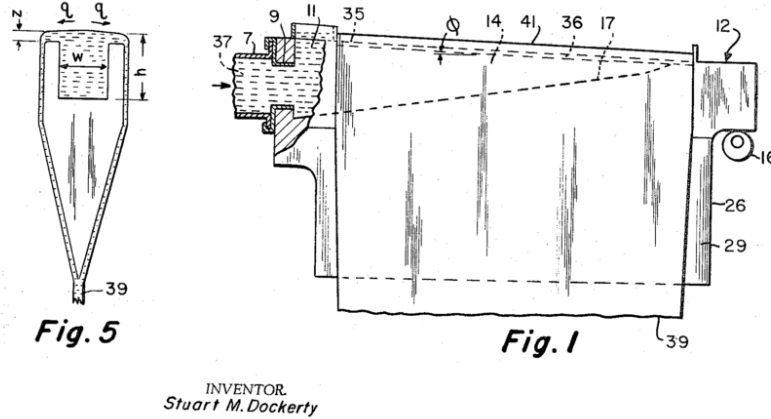


Figure 3.1: Fig. 5 extracted from the 1964 patent represents a cross section of the injection apparatus, with overflowing molten glass flowing on the sides of the triangular gutter and reuniting at the bottom into a thin sheet. Fig. 1 also extracted from the patent shows a front view of the gutter. The dashed line at the bottom corresponds to what we will consider as the top of our domain of study.

When the curtain falls down, a flow in the lateral direction appears, and some compressive strains are created. Since we study a thin structure, the presence of these compressive strains can lead to a buckling instability if the strains are large enough. As the bending stiffness of the sheet goes down, similarly to the case of the Elastica, the curtain may become unstable.

Because of its application to the formation of liquid curtains, studying this problem is of importance in terms of fluid mechanics. However, more fundamental aspects of the study are also very interesting. First, Stokes-Rayleigh analogy finds in this study a fitting application, but is limited to the study of the stationary flow. Going further requires studying a fully two dimensional flow using a numerical global stability analysis, while taking into account advection effects.

### 3.1.2 Geometry of the curtain

In order to create a curtain of viscous fluid, a horizontal hanging slit is used to inject a viscous liquid at a prescribed injection velocity  $U$ . It is injected vertically and is further accelerated by the effect of gravity. The flow is vertical and forms a thin and planar curtain of viscous fluid.

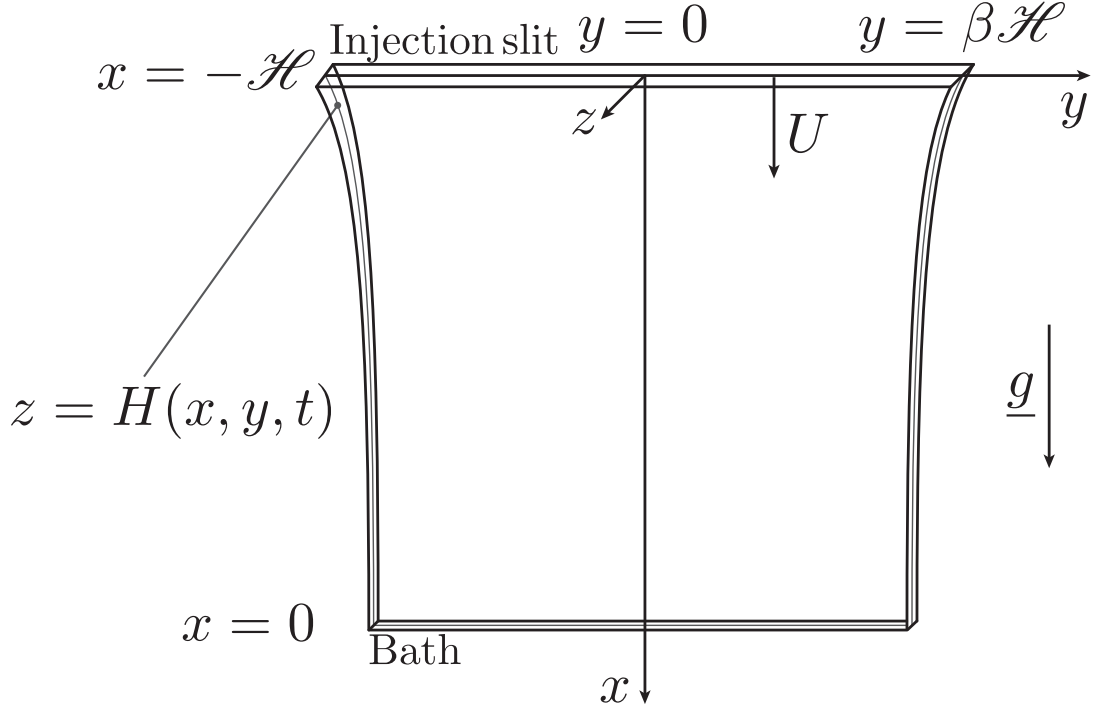


Figure 3.2: Geometry of the falling viscous curtain.

As the thin sheet of viscous liquid accelerates downwards gravity stretches the film in the vertical (axial) direction. Lower particles move faster and move away from particles behind them. Because of volume conservation particles will also move closer to each other in the two other (transverse) directions. This phenomenon can lead to the appearance of compressive stress in the horizontal direction. Since the liquid sheet has a small thickness, we expect that it may be unstable with respect to a buckling instability. Thin structures in mechanics are generally sensitive to compressive stresses, as they can trigger bending modes through buckling that sometimes result in very large displacements that can be catastrophic. In the case of the glass curtain, buckling of the surface would lead to non planar and unusable glass panes.

In the problems presented in the introduction of this chapter, viscous flows were submitted to shear and developed compressive stress large enough to display a buckling instability. Whether it is orthoradial or along a straight axis, these problems display a strong symmetry that lets authors work with a homogeneous pre-buckled solution as their starting point. In our study, the planar unbuckled configuration is spatially inhomogeneous and will display both extensional and compressive regions.

## 3.2 Problem definition

In order to describe the curtain and its corresponding equations we adopt several notations. We use Cartesian coordinates  $(x, y, z)$ : the three dimensions of the model are one transverse to the sheet ( $z$  axis), one across the width of the sheet ( $y$  axis) and one

aligned with the direction of gravity ( $x$  axis) as represented in figure 3.2.

The top of the sheet, where the fluid is injected, corresponds to  $x = -\mathcal{H}$  and the bottom, where the fluid contacts with a bath to  $x = 0$ . In the  $y$  direction, the position of the centre of the sheet is  $y = 0$  and the position of the edges are  $y = \pm\beta\mathcal{H}$ . Here  $\beta$  is the dimensionless parameter that represents the aspect ratio of the curtain. When symmetries are applicable, we will restrict the domain to one half of the curtain, i.e.  $x \in [-\mathcal{H}; 0]$  and  $y \in [0; \beta\mathcal{H}]$ .

Greek letters will be used to denote generic indexes in the plane of the sheet (directions  $x$  and  $y$ ), we will also assume summation over repeated indexes. Commas in subscripts indicate partial derivatives, e.g.  $\phi_{,x}$  denotes the partial derivative of the generic function  $\phi$  with respect to the variable  $x$ .

At any time  $t$ , let  $z = H(x, y, t)$  be the position of the sheet's centre surface, and  $h$  its thickness. The velocity field in the mid-plane of the sheet is two dimensional and is denoted by  $\underline{u}(x, y, t)$ . In these functions, coordinates  $x$  and  $y$  are Eulerian variables and refer to the actual configuration.

### 3.2.1 Kinematics

In order to describe the buckling of a fluid sheet, we have to model the movement of fluid particles in the plane of the curtain, and the out of plane displacements caused by buckling. We will thus use in-plane **velocities** along the tangent plane ( $x, y$ ), and the out-of-plane **displacement**. This mixed formulation, which makes use of both velocity and position as unknowns, will turn out to be very convenient, although it is nonstandard.

When searching for a steady planar base flow that establishes in the curtain, the two unknowns are the in-plane Eulerian velocities. When studying buckling modes we use the Eulerian out-of-plane deflection of the sheet's centre surface,  $H(x, y, t)$  as the unknown. For the sake of conciseness, we may omit the time argument of some functions in the following.

We have to consider material derivatives in time as fluid movement is responsible for a convective effect that we express in an Eulerian framework. Both the in plane velocities  $u_x$ ,  $u_y$  and the out of plane displacement  $H$  are functions of the Eulerian variables ( $x, y$ ). In this framework, time derivatives become comoving derivatives that involve the gradient of the surrounding flow. The comoving derivative of a generic function  $f(x, y, t)$  of Eulerian variables is:

$$\frac{Df}{Dt} = f_{,t} + u_\alpha f_{,\alpha} \quad (3.1)$$

We recall notations, greek letters  $\alpha$  and  $\beta$  are used to denote generic indexes in the plane of the sheet (directions  $x$  and  $y$ ). The commas in subscripts indicate partial derivatives, e.g.  $\phi_{,\alpha}$  denotes the partial derivative of  $\phi$  with respect to  $x$  or  $y$ , as we also assume summation over repeated indices.

We will first consider the advection of a small material segment  $d\mathbf{l} = (dx, dy, dz) = (dx_\alpha, dx_\beta, dz)$  attached to the centre surface of the sheet. This line represent an elementary fluid segment that moves with the surrounding flow. As it is advected, it also sustains deformations due to the differences in velocities along its length. By evaluating its extension as a function of the surrounding field we can obtain the strain rate tensor, that quantifies the strain that develops in the fluid.

When the small material segment is advected, it deforms with the local gradient of velocities of the in-plane directions as follows:

$$dx(t + dt) = dx(t) + dt(u_x(x + dx, y + dy) - u_x(x, y)) = dx(t) + dt(u_{x,x} dx + u_{x,y} dy)$$

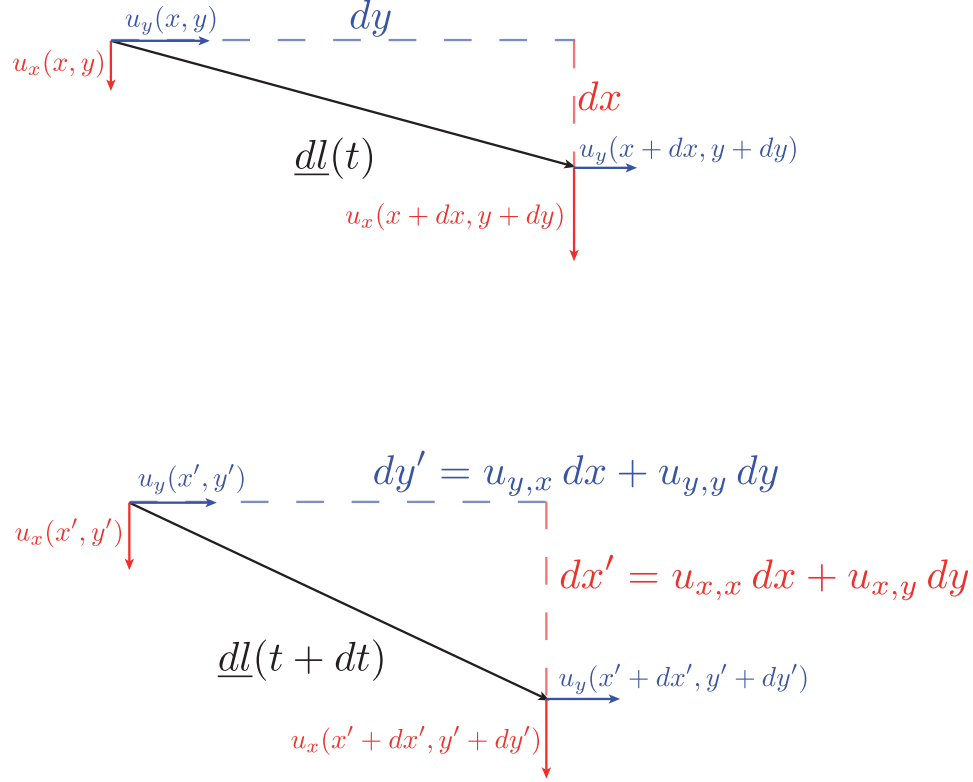


Figure 3.3: The material line  $\underline{dl}$  at two successive times. Its in plane components are advected by the surrounding flow and deform with the gradient of velocities. This process defines the comoving derivative.

The previous equation is used to express the difference quotient, and dividing by the time increment we obtain the comoving derivative of  $dx$  as:

$$\frac{Ddx}{Dt} = u_{x,\beta} dx_\beta$$

The  $y$ -component is treated similarly and we find the comoving derivative of both in-plane components of  $\underline{dl}$ :

$$\frac{Ddx_\alpha}{Dt} = u_{\alpha,\beta} dx_\beta \quad (3.2)$$

For the  $z$ -component of the material element  $\underline{dl}$ , the calculation is a little bit different, since it depends on the deflection profile  $H(x, y, t)$ . The length of the material element  $dz$  can be linearly approximated as  $dz \approx H_{,\alpha} dx_\alpha$ . The deformation of the third component of the small material segment is thus:

$$\frac{Ddz}{Dt} = (H_{,\alpha t} + u_\beta H_{,\beta\alpha}) dx_\alpha + H_{,\beta} u_{\beta,\alpha} dx_\alpha \quad (3.3)$$

This equation is simply obtained by taking the total derivative of the product  $H_{,\alpha} dx_\alpha$  and using formula (3.2) for the in-plane total derivative.

We now want to identify the strain rate tensor  $\underline{\underline{d}}$  that is applied on the curtain as it flows down. This tensor measures the rate of deformation of material elements. We can identify  $\underline{\underline{d}}$  by using the equality

$$\underline{\underline{dl}} \cdot \underline{\underline{d}} \cdot \underline{\underline{dl}} = \frac{1}{2} \frac{D\underline{\underline{dl}}^2}{Dt} = dx_\alpha \frac{Ddx_\alpha}{Dt} + dz \frac{Ddz}{Dt}$$

Expressing  $\underline{\underline{dl}} \cdot \underline{\underline{d}} \cdot \underline{\underline{dl}}$  in components

$$\underline{\underline{dl}} \cdot \underline{\underline{d}} \cdot \underline{\underline{dl}} = \underline{\underline{dl}} \cdot (d_{\alpha\beta} e_\alpha \otimes e_\beta) \cdot \underline{\underline{dl}} = d_{\alpha\beta} dx_\alpha dx_\beta \quad (3.4)$$

Developing expression  $dx_\alpha \frac{Ddx_\alpha}{Dt} + dz \frac{Ddz}{Dt}$  using equations (3.2) and (3.3), we obtain through identification:

$$d_{\alpha\beta} = u_{(\alpha,\beta)} + H_{,(\alpha} H_{,\beta)t} + u_\gamma H_{,(\alpha} H_{,\beta)\gamma} + u_{\gamma,(\alpha} H_{,\beta)} H_{,\gamma} \quad (3.5)$$

The subscript  $\gamma$  is a greek index and plays the same role as  $\alpha$  or  $\beta$ , it appears here as a dummy index and denotes directions  $x$  or  $y$ . Here the tensor is written in its symmetric form with the help of the parenthesis notation. Indices contained in the parentheses are symmetric according to the rule  $A_{(\alpha\beta)} = \frac{1}{2}A_{\alpha\beta} + \frac{1}{2}A_{\beta\alpha}$ .

It is useful to provide an interpretation to the two parts making up the tensor  $d_{\alpha\beta}$  (3.5). The first part is the classical strain rate for a planar fluid mechanics problem, it only comprises the derivatives in space of the velocities in the curtain. This expression is exactly the same as in linear 2D elasticity, the Stokes Rayleigh analogy lets us predict this term, with displacements changed to velocities, and therefore linear strains becoming strain rates. Other terms in the formulation of  $d_{\alpha\beta}$  all involve the out of plane displacement  $H$  and will have no influence on the planar problem. In these terms however, velocities in the plane of the curtain are coupled to the out of plane displacement, and will be at the core of the buckling phenomenon under study.

In the elastic formulation of viscous plates, the other important tensor is the bending strain rate tensor  $\dot{\underline{\underline{K}}}$ . It is equivalent to the bending strain tensor of an elastic plate, but through the Stokes-Rayleigh analogy implies an additional dimension of time and becomes a strain rate tensor. When considering small deflections, the bending strains of a nearly flat sheet are equal to the curvatures. Local curvature is obtained with the second derivative of the out of plane displacement and  $K_{\alpha\beta} = H_{,\alpha\beta}$ . In order to obtain the tensor capturing the rate of bending strain, we just have to take the total derivative in time of the previous expression.

$$\dot{K}_{\alpha\beta} = \frac{D(H_{,\alpha\beta})}{Dt} = H_{,\alpha\beta t} + u_\gamma H_{,\alpha\beta\gamma} \quad (3.6)$$

We have now identified both the stretching and bending strain rate tensors in terms of our kinematic variables in equations (3.5) and (3.6). The next step is to define constitutive relations for the viscous material we use.

### 3.2.2 Constitutive laws

As the viscous fluid forming the curtain is considered to be a Newtonian fluid, constitutive relations for the material are immediate analogues of a linear elastic constitutive law in solid mechanics. Once again, the Stokes Rayleigh analogy can be used to replace elastic moduli by the viscous ones and write down constitutive relations. Obtaining these relations for membranes can be done by reducing the three-dimensional Stokes equations of viscous flows [Rib02, PAB11]. In the process of averaging over the thickness of the sheet, velocities along the  $z$ -direction can be rescaled by following two different scalings for time. The resulting equations describe different limits for the kinematics of a viscous sheet. The time scale for velocities in the direction of the thickness is

$$t = \varepsilon^{2m} \frac{H}{U} t' \quad (3.7)$$

with the choice for  $m$  leading to the two different models, see [How96]. The Trouton scaling ( $m = 0$ ) corresponds to a deformation of the sheet dominated by stretching, while the BNT (Buckmaster, Nachman and Ting [BNT75, BN78]) scaling ( $m = 1$ ) accounts for both stretching and bending. The most important difference between these two scalings is that the Trouton scaling leads to kinematics where the thickness of the sheet evolves, while in the BNT scaling, the thickness of the sheet remains constant but bending effects are important. In the Trouton scaling, we can expect the sheet to accommodate strains through changes of its thickness, while in the BNT scaling, we expect the sheet to deform out of plane by bending. The equations presented in the following are obtained by using the BNT scaling, which leads to constitutive relations for both stretching and bending stresses.

$$N_{\alpha\beta} = 2\mu h (d_{\alpha\beta} + \delta_{\alpha\beta} d_{\gamma\gamma}) \quad (3.8)$$

$$M_{\alpha\beta} = \frac{\mu h^3}{6} (\dot{K}_{\alpha\beta} + \delta_{\alpha\beta} \dot{K}_{\gamma\gamma}) \quad (3.9)$$

Here  $\delta_{\alpha\beta}$  denotes the Kronecker delta  $\begin{cases} 0 & \text{if } \alpha \neq \beta \\ 1 & \text{if } \alpha = \beta \end{cases}$  so that the second term in the parentheses are the traces of the tensors  $\underline{d}$  and  $\underline{\dot{K}}$ .

In these equations, the tensor  $\underline{N}$  represents the membrane stress. It measures the stress in a membrane due to stretching of its surface. Similarly, the tensor  $\underline{M}$  represents the bending stresses, that are due to bending of the surface.

Before obtaining the equations governing our problem, we need to specify the boundary conditions.

### 3.2.3 Kinematic boundary conditions

Kinematic boundary conditions derive from our choice for the geometry of the problem. The fact that the viscous curtain is being injected at the top, that it is falling freely and what happens at the bottom will have an influence of the resulting boundary conditions.

The viscous curtain is falling in an open medium, of negligible friction, hence it is considered stress free on its lateral edges. This means stresses will go to zero, including bending moments. Stress free boundary conditions aren't associated with any kinematic constraint and the sides of the domain are only subjected to natural boundary conditions.

As mentioned in §1.4.1 natural boundary conditions are automatically enforced when solving the weak form numerically.

We suppose that the bottom of the curtain is falling in a bath of the same liquid. In the stationary regime, we expect it to reach the surface with a velocity comprising only a vertical component. Hence at  $x = 0$ ,  $u_y = 0$ . The liquid bath will permit movements at the bottom of the curtain, we impose no kinematic boundary conditions and keep natural ones for the out of plane deflection  $H$ . This means that  $H$  and its first derivative  $H_{,x}$  will be set respectively through a force and a moment balance.

The problem has an axis of symmetry for the in-plane velocities at  $y = 0$ , in the context of eigenvalue analysis out-of-plane displacements can be thought as either symmetric or antisymmetric with respect to the  $x$  axis.

The presence of an injector at the top prescribes a purely vertical speed,  $u_x = U$  and  $u_y = 0$  on the  $x = -1$  border. This injector also prescribes specific boundary conditions for the out of plane displacement, which we derive now.

Injecting some liquid at speed  $U$  at the top of the curtain constrains the out of plane displacement. Exiting the injector, the sheet stays flat and we have  $H = 0$  and  $H_{,x} = 0$ . By pushing the liquid at speed  $U$  out of the injector, we know that both the position and the tangent to the curtain are continuous while passing the slit.

The presence of an advective term changes a lot the structure of the equations, and setting  $U \neq 0$  implies that we take into account comoving derivatives. Since  $H$  and  $H_{,x}$  are identically zero, even in the situation where  $U = 0$ , one can write  $\frac{dH}{dt} = 0$  and  $\frac{dH_{,x}}{dt} = 0$ . We want to write these conditions using comoving derivatives to take into account the injection velocity  $U$ .

As the fluid is injected through the slit, it is considered to come from a constrained flat environment. In that injection mould, out-of-plane displacement  $H$  and rotation  $H_{,x}$  are constrained to take zero values. Upon exiting the mould, the out-of-plane velocity  $u_z = \frac{DH}{Dt}$  has to be continuous since its acceleration is finite and we can use the fundamental principle of dynamics to derive it. Hence at the top, the boundary condition  $\frac{DH}{Dt} = H_{,t} + U H_{,x} = 0$  is enforced, which means that as soon as  $U \neq 0$ ,  $H_{,x} = 0$ . This condition was already known since we assumed a flat injector forcing no out-of-plane movement. We can use the same reasoning by invoking the theorem of angular moments and stating that the angular velocity  $\omega = \frac{DH_{,x}}{Dt}$  must be continuous upon exiting the injector. When the advection speed becomes  $U \neq 0$ , we can write these two equations using comoving derivatives:

$$\begin{aligned}\frac{DH}{Dt} &= H_{,t} + U H_{,x} = 0 \\ \frac{DH_{,x}}{Dt} &= H_{,xt} + U H_{,xx} = 0\end{aligned}$$

Here we can see that when the injection speed is non zero, our equations gain one order in space derivatives and we need to introduce an additional boundary condition. This boundary condition necessarily appears at the injector, and derives from previously imposed conditions. Maintaining the two boundary conditions  $H = 0$  and  $H_{,x} = 0$ , the second equation leads to  $H_{,xx} = 0$ , which is our additional boundary condition at  $x = 0$  when  $U \neq 0$ .

This completes the set of kinematic boundary conditions on the displacement  $H$  and appears in table (3.1).

kinematic BCs	in plane velocities ( $u_x, u_y$ )	out of plane deflection $H$
free lateral edges	none	none
top (injection)	$u_x = U$ $u_y = 0$	$H = 0$ $H_{,x} = 0$ $H_{,xx} = 0$
bottom	$u_y = 0$	none
centreline (axis of symmetry)	$u_y = 0$	* $\begin{cases} H_{,y} = 0 \text{ (symmetric)} \\ H = 0 \text{ (antisymmetric)} \end{cases}$

Table 3.1: Kinematic boundary conditions for half of the curtain. The base solution being symmetric with respect to the  $x$  axis, numerics solve for half of the curtain. Additional boundary conditions due to the centreline are given in the last row. The stability analysis is also solved for a half curtain, with centreline kinematic boundary conditions on the displacement  $H$  (indicated by a \*) corresponding to the symmetric and anti-symmetric modes respectively.

### 3.2.4 Applied volume forces

We have modelled the falling viscous curtain as a viscous shell and derived the elastic stresses due to its deformations. We have also defined boundary conditions that are imposed by the geometry we have chosen, in particular the fact that the liquid is injected at a velocity  $U$  on the top boundary. Regarding the base solution, this injection speed appears as a boundary condition. For the out of plane equations, it is part of the advective terms, and also has a peculiar effect on the top boundary condition as explained earlier.

We will now add two last ingredients to this problem. First we consider the volume force due to gravity, that will be responsible for an instability. Second, we take into account internal stresses due to capillary strains.

During the fall of the curtain, the main driving force is of course gravity's pull on the viscous sheet. Denoting by  $\rho$  the volume density of the liquid making up the curtain and by  $g$  the acceleration of gravity, volume forces due to gravity are of the order  $\rho g$ . If we want to compare this body force to viscous effects, we need to evaluate the order of magnitude of the viscous volume force.

Using  $\mu$  as the dynamic viscosity of the fluid, and since  $U$  is the order of magnitude of the velocities that develop in the curtain, we are interested in an evaluation of the order of the typical viscous stress. In Stokes equation, the viscous term is  $\mu \Delta \underline{u}$ . For velocities developing during the fall of the curtain, i.e. over its height and width of typical dimension  $\mathcal{H}$ , the order of the viscous volume force is thus  $\frac{\mu U}{\mathcal{H}^2}$ .

Comparing gravity's action and viscous effects, the ratio of the corresponding volume forces defines the dimensionless quantity  $Je$ , called Jeffreys number [Jef25]. TODO O Keefe...

$$Je = \frac{\rho g \mathcal{H}^2}{\mu U} \quad (3.10)$$

For large values of this number, the effect of gravity is strong and vertical acceleration is significant. It means that although the injection speed is fixed to  $U$ , after travelling along the height of the curtain while submitted to gravity's pull, the velocity of fluid particles will be significantly larger than  $U$ . In that limit, the viscous curtain deforms



a lot because of the effect of gravity, and a model giving the shape of the curtain can be found in a private communication by N. M. Ribe [Rib08]. We will be studying the problem in the other limit, where the injection speed  $U$  is large and acceleration due to gravity is weak and only causes small variations in velocity. Hence we are in the situation where  $Je \ll 1$ . This means that the velocities that will develop in the curtain, driven by the effect of  $Je$ , will be small compared to  $U$ . Hence the viscous strains associated with these small velocities  $\frac{\mu \Delta u}{\mathcal{H}^2}$  will be of the same order of magnitude as the driving force  $\rho g$ . Hence  $\frac{\rho g \mathcal{H}^2}{\mu \Delta u} \approx 1$  and we obtain  $\Delta u \approx Je U$ .

The surface tension  $\gamma$  between the liquid and ambient air is assumed to be constant. We suppose that out of plane displacements are small and of the order of the thickness of the curtain  $h$ . If we call  $H^*$  a typical transverse displacement, we can write the order of magnitude of the capillary forces per unit volume as  $\frac{\gamma H^*}{\mathcal{H}^2 h}$ . We are looking for a dimensionless number comparing the strength of capillary effects and viscous stresses, we use the ratio of capillary and viscous volume forces,  $\frac{\gamma H^* \mathcal{H}^2}{\mu U \mathcal{H}^2 h} = \frac{\gamma H^*}{\mu U h}$ . We already have  $h \ll \mathcal{H}$ , and we assume small out of plane displacements  $H^* \ll \mathcal{H}$ . We choose these two quantities to be of the same order,  $h \approx H^*$ , which is a common scaling underlying models for plates undergoing moderate deflections (as in the Föppl-von Kármán plate model). The ratio of the two volume forces becomes  $\frac{\gamma}{\mu U}$  which defines the inverse capillary number

$$\frac{1}{Ca} = \frac{\gamma}{\mu U} \quad (3.11)$$

Those dimensionless numbers will be used to measure the amplitude of the different forces acting on the curtain and will appear naturally in the dimensionless version of the equations.

### 3.2.5 Dimensionless quantities

To obtain dimensionless equations we need to define the typical dimension of our different variables. We have a natural length  $\mathcal{H}$ , the height of the curtain. Another length must be taken into account as the curtain is very thin, we use  $h$  to represent its thickness. We know that  $h \ll \mathcal{H}$  and thus define a small parameter  $\varepsilon = \frac{h}{\mathcal{H}}$ .

As the effect of gravity is considered small ( $Je \ll 1$ ), we assume that the velocities in the curtain will not be much different from  $U$ , the injection speed at the top of the sheet. We thus use  $U$  as a natural scale for velocities.

This lets us define a time scale  $\frac{\mathcal{H}}{U}$ , and we now have enough independent dimensions to define the dimensionless variables. Dimensionless versions of the variables are indicated with a prime:

$$\begin{aligned} h &= \varepsilon \mathcal{H} & H &= \varepsilon \mathcal{H} H' & t &= \frac{\mathcal{H}}{U} t' \\ x &= \mathcal{H} x' & y &= \mathcal{H} y' & z &= \varepsilon \mathcal{H} z' \\ u_x &= U u'_x & u_y &= U u'_y & \\ d_{\alpha\beta} &= \frac{U}{\mathcal{H}} d'_{\alpha\beta} & \dot{K}_{\alpha\beta} &= \frac{\varepsilon U}{\mathcal{H}^2} \dot{K}'_{\alpha\beta} & \hat{\epsilon}_{\alpha\beta} &= \frac{1}{\mathcal{H}} \hat{\epsilon}'_{\alpha\beta} \\ N_{\alpha\beta} &= 2 \mu U \varepsilon N'_{\alpha\beta} & M_{\alpha\beta} &= 1/6 \mu U \varepsilon^4 \mathcal{H} M'_{\alpha\beta} \end{aligned}$$

We will drop the prime notation and consider only dimensionless quantities from now on. With these proposed scales, the curtain is now of unit height with  $x \in [-1, 0]$ , its width is twice the aspect ratio  $\beta$ ,  $y \in [-\beta, \beta]$  and its thickness is  $\varepsilon$ .

The first dimensionless parameter of the problem is the aspect ratio of the sheet  $\beta$ , that defines the two dimensional shape of the curtain. Using  $\varepsilon$  for the thickness of the sheet (this dimensionless ratio measures the slenderness of the curtain) is enough to define the geometry of the viscous curtain. Injection velocity  $U$  is rescaled and we use Jeffreys number  $Je$  to compare the effect of gravity, which acts as the other main driving force for the flow, with viscous effects. The last dimensionless number to be considered is the inverse capillary number  $Ca^{-1}$ , comparing capillary effects with viscous dissipation.

### 3.3 Weak formulation

We can now apply the principle of virtual work in order to obtain equations governing the viscous curtain. We obtain a linear form that has to cancel for the flow to be at equilibrium. Internal forces (membrane and bending stresses as well as capillarity) and external forces (gravity's effect) contribute to the global energy of the curtain.

Internal efforts are not conservative and are obtained using a two dimensional model for viscous membranes [Rib02, PAB11]. Contributions from both membrane and bending stresses are taken into account through the stretching and bending tensors  $N_{\alpha\beta}$  and  $M_{\alpha\beta}$  respectively. These are calculated using the real configuration of the curtain. Writing equations in weak form, these two tensors are multiplied by corresponding virtual strains (measuring elongation and curvature).

$$\hat{W}_{int} = \iint (-N_{\alpha\beta} \hat{\epsilon}_{\alpha\beta} - \varepsilon^2 M_{\alpha\beta} \hat{w}_{,\alpha\beta}) dS \quad (3.12)$$

Inspired by a plate mechanics model, we introduce a geometrical non linearity through the tensor  $\hat{\epsilon}_{\alpha\beta} = \hat{u}_{(\alpha,\beta)} + H_{,(\alpha} \hat{w}_{,\beta)}$ .  $\hat{u}_\alpha$  and  $\hat{w}$  are virtual displacements for the in plane and out of plane directions that will be used as unknowns in the numerical simulations. This tensor involves the out-of-plane deflection  $H$ , introducing a coupling between stretching due to in-plane velocities,  $N_{\alpha\beta}$ , and out-of-plane movements. This is the same non linearity that is taken into account to derive the Föppl-von Kármán equations in plate mechanics. Internal work is thus obtained as the sum of two terms corresponding to stretching and bending. The stretching term is the product of the stretching stress  $N_{\alpha\beta}$  and of the plate mechanics inspired virtual displacement tensor  $\hat{\epsilon}_{\alpha\beta}$ , introducing a geometrical non linearity. The bending term is the product of the bending stress  $M_{\alpha\beta}$  and of a virtual displacement corresponding to a curvature. Virtual displacement being dimensionless quantities, the name virtual velocity could also be used for  $\hat{u}_\alpha$ .

External efforts are due to the two acting forces, gravity and capillary effects. External work is by definition the product of the force with a motion that has this force doing work  $\hat{W}_{ext,f} = \int -f \hat{x}$ . In the case of gravity, a change in height will have the weight working, while a horizontal movement can be done with no work on the part of gravity.

Virtual works are dimensionless, which means a virtual displacement in the vertical direction is associated with all virtual changes of kinematic variables occurring in the vertical direction, hence we use the same notation  $\hat{u}_x$  and write the external work associated with gravity  $\hat{W}_{ext,\rho g} = \int Je \hat{u}_x$  in dimensionless variables. The additional minus sign comes from the definition of the  $x$  axis pointing to the bottom.

In the case of capillarity, work is done by capillary forces when a change in area is observed. By choosing a virtual displacement tensor inspired by plate mechanics  $\hat{\epsilon}_{\alpha\beta}$ , we assume that changes in area can be due to in-plane velocities, but also to out-of-plane deflection through the first order geometrical non linearity we take into account. Changes in area are then measured using the trace of the tensor  $\hat{\underline{\epsilon}}$ ,  $\text{Tr } \hat{\underline{\epsilon}} = \hat{\epsilon}_{\alpha\alpha}$ . We can then immediately write the external work done by capillary forces as  $\hat{W}_{ext,\gamma} = \int -\frac{1}{\text{Ca}\varepsilon} \hat{\epsilon}_{\alpha\alpha} = \int -\frac{1}{\text{Ca}\varepsilon} (\hat{u}_{\alpha,\alpha} + H_\alpha \hat{w}_{,\alpha})$ .

By summing the external work done by of these two forces we can write the total external work:

$$\hat{W}_{ext} = \hat{W}_{ext,\rho g} + \hat{W}_{ext,\gamma} = \int \text{Je } \hat{u}_x - \frac{1}{\text{Ca}\varepsilon} \hat{\epsilon}_{\alpha\alpha} \quad (3.13)$$

Summing internal and external work, we obtain the weak form with unknowns  $(u_x, u_y, H)$  and virtual displacements  $(\hat{u}_x, \hat{u}_y, \hat{w})$ :

$$\int -N_{\alpha\beta} \hat{\epsilon}_{\alpha\beta} - \varepsilon^2 M_{\alpha\beta} \hat{w}_{,\alpha\beta} + \text{Je } \hat{u}_x - \frac{1}{\text{Ca}\varepsilon} \hat{\epsilon}_{\alpha\alpha} = 0 \quad (3.14)$$

This weak form cancels when the curtain is at static equilibrium and can be used in a numerical scheme to find equilibrium configurations. To do so, we have to take into account kinematic boundary conditions that the virtual fields  $(\hat{u}_x, \hat{u}_y, \hat{w})$  have to verify. Virtual functions cannot be chosen completely freely but must be kinematically admissible. A kinematically admissible motion is any differentiable motion that is geometrically compatible with kinematic constraints. These constraints appear in table (3.1) and must be set in the numerical scheme.

The weak form can also be used to obtain equilibrium equations, also called the strong form of the equations. In the next paragraph, we will follow a similar process as in §1.3 to obtain the equilibrium equations along with dynamic boundary conditions.

### 3.3.1 Strong form of the equations

Using integration by parts we recover the equations that derive from the equilibrium balance of forces. We obtain three equations, the first one corresponds to a vertical balance, that involves the effect of gravity on the extension of the sheet, equation (3.15a). The horizontal balance is a simple equilibrium condition (3.15b). The third equation we obtain (3.15c) is an out of plane equilibrium that involves stresses in the sheet, leading to buckling that must fight capillary forces.

$$N_{x\beta,\beta} + \text{Je} = 0 \quad (3.15a)$$

$$N_{y\beta,\beta} = 0 \quad (3.15b)$$

$$(N_{\alpha\beta} H_{,\alpha})_{,\beta} - \varepsilon^2 M_{\alpha\beta,\alpha\beta} + \frac{1}{\text{Ca}\varepsilon} H_{,\alpha\alpha} = 0 \quad (3.15c)$$

Obtaining these equations requires integrating by parts the weak form (3.14) assuming kinematic boundary conditions. During the process of integration by parts, boundary terms that appear are either cancelled by the kinematic boundary conditions, or must be retained as additional equations to be solved simultaneously, these are called the natural boundary conditions (see table 3.2). These equations correspond to the force balance in the different directions. The first two equations are usually obtained by calculating the divergence of strains in the two tangent directions. Equation (3.15c) corresponds to

the force balance in the transverse direction, and its first two terms are analogous to Föppl-von Kármán's equation with different constitutive relations. The first one couples the planar stresses with the vertical displacement, a nonlinear effect essential to describe for example an inflating balloon. The second term is the transverse resultant due to bending. The third term of this equation is due to capillarity effects, that tend to prevent elongation, and thus out-of-plane movement.

### 3.3.2 Summary of the equations

The problem of the falling viscous curtain is now completely defined. Strains in the sheet can be due to stretching and bending, and we have obtained the strain rate tensors for both of these, equation (3.5) and (3.6) respectively. We chose linear constitutive relations involving the viscous moduli presented in equations (3.9). We also consider the effect of two applied forces, the weight and capillarity. Their influence is measured by two dimensionless parameters, Jeffreys number  $Je$  (3.10) and the inverse capillary number  $Ca^{-1}$  (3.11). By evaluating both the internal and external work and using the principle of virtual work we obtained the weak form of the equations (3.14). In order to obtain a numerical solution to these equations, kinematic boundary conditions must be imposed, and these are regrouped in table 3.1. However, solving the strong form of the equations (3.15) requires to take into account the complete set of kinematic and natural boundary conditions. These are exposed in the following table:

	base solution		stability analysis	
	kinematic	natural	kinematic	natural
free lateral edges		$N_{xy} = 0$ $N_{yy} + \frac{1}{Ca\varepsilon} = 0$		$N_{xy} H_{,x} + N_{yy} H_{,y}$ $-\varepsilon^2 M_{yx,x} - \varepsilon^2 M_{yy,y}$ $+ \frac{1}{Ca\varepsilon} H_{,y} = 0$ $M_{yy} = 0$
top (injection)	$u_x = U$ $u_y = 0$		$H = 0$ $H_{,x} = 0$ $H_{,xx} = 0$	
bottom	$u_y = 0$	$N_{xx} + \frac{1}{Ca\varepsilon} = 0$		$N_{xx} H_{,x} + N_{yx} H_{,y}$ $-\varepsilon^2 M_{xx,x} - \varepsilon^2 M_{xy,y}$ $+ \frac{1}{Ca\varepsilon} H_{,x} = 0$ $-\varepsilon M_{xx} = 0$
centreline (axis of symmetry)	$u_y = 0$	$N_{xy} = 0$	$\begin{cases} H_{,y} = 0 & \text{(s)} \\ H = 0 & \text{(as)} \end{cases}$	$\begin{cases} N_{xy} H_{,x} + N_{yy} H_{,y} \\ -\varepsilon^2 M_{yx,x} - \varepsilon^2 M_{yy,y} \\ + \frac{1}{Ca\varepsilon} H_{,y} = 0 & \text{(s)} \\ M_{yy} = 0 & \text{(as)} \end{cases}$

Table 3.2: Boundary conditions for half of the curtain. The base solution being symmetric with respect to the  $x$  axis, numerics solve for half of the curtain. Additional boundary conditions due to the centreline are given in the last row. The stability analysis is also solved for a half curtain, with centreline kinematic boundary conditions on the displacement  $H$  (choice indicated by braces) corresponding to the symmetric and anti-symmetric modes respectively.

### 3.3.3 Weak form for the base solution

In the first step of the study, we want to derive the velocity field that develops in the curtain as it falls vertically. Similarly to the case of the *Elastica*, we will obtain a solution for the flow field in the sheet and compute its stability in a second step. The first step is to ignore the possibility of an out of plane displacement, and solve only for a flat curtain.

We call  $(u_x^{(0)}, u_y^{(0)}, H^{(0)})$  the field making up the base solution, with the hypothesis of a stationary solution and a flat configuration. This means we assume that  $u_x^{(0)}$  and  $u_y^{(0)}$  are independent of time, and that  $H^{(0)} = 0$ . Out of plane movements will be obtained in the second step, as a perturbation to the base planar flow (see §3.3.4).

#### Linearization with respect to $Je$

As mentioned earlier, we will assume the effect of gravity to remain weak, this means that Jeffreys number  $Je$  (which compares the strength of gravity with viscous forces) is considered small. Since the curtain is injected at speed  $U = 1$  (dimensionless equations use  $U$  as the scale for velocities) from the top of the domain, in the absence of any other forces, one would expect the curtain to fall in a rigid movement of velocity  $u_x = 1, u_y = 0$  everywhere in the domain. Considering the effect of gravity, quantified by  $Je$ , it will have a tendency to accelerate downwards as it is being pulled down, while horizontal velocities may develop.

We study the linear response to the small effects of gravity's pull, thus modifications to the rigid-body translation with velocity  $U$  will be of order  $Je \ll 1$ . We introduce a notation for the quantities implied in the base solution:

$$\begin{aligned} u_\alpha^{(0)} &= \delta_{\alpha x} + Je \bar{u}_\alpha^{(0)} \\ N_{\alpha\beta}^{(0)} &= Je \bar{N}_{\alpha\beta}^{(0)} \end{aligned}$$

This weak gravity, or strong advection, assumption and the fact that horizontal velocities are small means that the curtain will not be strongly deformed as it falls down, and that the domain of study stays close to a rectangle. Since we study linear perturbations in  $Je$ , we consider the unknowns  $\bar{u}_\alpha$  to be defined on a rectangle, corrections due to its small deformation would lead to order 2 terms that we don't take into account. In the limit  $Je \ll 1$  which we consider, the calculation of the base flow, which is a nonlinear problem involving a free boundary in general, has been transformed into a linear problem on a fixed, rectangular domain. We will verify in §4.1.1 that this assumption is correct by computing the shape of the open edges.

The inverse capillary number is also assumed to be small and capillary effects will be neglected. We will set  $\frac{1}{Ca} = 0$  for most of the following results. We will restore the effect of capillarity in §4.4.

#### Weak form for the base solution

In order to obtain the weak form corresponding to a flat curtain, and find the stationary solution for  $u_x^{(0)}$  and  $u_y^{(0)}$  we simply set the out of plane displacement  $H$  and its associated virtual displacement  $\hat{w}$  to zero in equation (3.14).

We obtain the equation  $\int -N_{\alpha\beta}^{(0)} \hat{u}_{(\alpha,\beta)} + Je \hat{u}_x = 0$  that can be written after dividing by  $Je$ :

$$\int -\bar{N}_{\alpha\beta}^{(0)} \hat{u}_{(\alpha,\beta)} + \hat{u}_x = 0 \quad (3.16)$$

with  $\bar{N}_{\alpha\beta}^{(0)} = 2(\bar{u}_{(\alpha,\beta)}^{(0)} + \delta_{\alpha\beta} \bar{u}_{\gamma,\gamma}^{(0)})$  and boundary conditions from the first column of table 3.1.

It is worth noting that this weak form is analogous to the one depicting an elastic rectangle in 2D, under applied load in the direction  $x$ . In this solid mechanics problem, boundary conditions chosen here would translate as boundary conditions on displacements. The imposed value of  $U$  at the top boundary is a rigid-body translation of the sheet with no influence on the final strain state.

### 3.3.4 Linearized weak form for the stability analysis

When studying the stability of the base solution, we have to restore the possibility for the curtain to move in the out of plane direction. We assume here that the base solution  $(u_x^{(0)}, u_y^{(0)})$  has already been obtained, the actual derivation will be done numerically in §4.1.

Like in the case of the Elastica of section §2.3.1 we want to perturb equations of equilibrium around the previously obtained base state. For all kinematic variables we write  $u_\alpha = u_\alpha^{(0)} + u_\alpha^{(1)} = \delta_{\alpha x} + \text{Je} \bar{u}_\alpha^{(0)} + u_\alpha^{(1)}$  and  $H = H^{(0)} + H^{(1)} = H^{(1)}$ , where  $^{(0)}$  denotes the base solution, and  $^{(1)}$  first order perturbations. We want to linearize equations, retaining only terms of order one. The virtual work in equation (3.14) is linearized as follows:

$$\begin{aligned} & \int -N_{\alpha\beta} \hat{\epsilon}_{\alpha\beta} - \varepsilon^2 M_{\alpha\beta} \hat{w}_{,\alpha\beta} + \text{Je} \hat{u}_x = 0 \\ & \int -(N_{\alpha\beta}^{(0)} + N_{\alpha\beta}^{(1)}) (\hat{u}_{(\alpha,\beta)} + H_{,\alpha}^{(1)} \hat{w}_{,\beta)}) - \varepsilon^2 M_{\alpha\beta}^{(1)} \hat{w}_{,\alpha\beta} + \text{Je} \hat{u}_x = 0 \\ & \int (-N_{\alpha\beta}^{(0)} \hat{u}_{(\alpha,\beta)} + \text{Je} \hat{u}_x) - \int (N_{\alpha\beta}^{(1)} \hat{u}_{(\alpha,\beta)} + N_{\alpha\beta}^{(0)} H_{,\alpha}^{(1)} \hat{w}_{,\beta} + \varepsilon^2 M_{\alpha\beta}^{(1)} \hat{w}_{,\alpha\beta}) = 0 \quad (3.17) \end{aligned}$$

We immediately recognize that the zero-th order terms (grouped in the left integral) correspond to the weak form verified by the base solution, and was already obtained in §3.3.3.

The velocities  $(u_x^{(0)}, u_y^{(0)})$  obtained in the base solution are perturbations of order  $\text{Je}$  around the simple translational state  $(U, 0)$ . We take these small perturbations into account in the calculation of strain rates in order to obtain nonzero stresses. However, when considering advective terms, it is not necessary to take these perturbations into account as they would lead to higher order terms. We obtain buckling modes in the limit  $\text{Je} \rightarrow 0$ .

In these equations  $N_{\alpha\beta}^{(1)}$  depends only on the tensor  $d_{\alpha\beta}$  linearized to first order which reduces to  $d_{\alpha\beta}^{(1)} = u_{(\alpha,\beta)}^{(1)}$ , other terms of order 1 being products of  $H^{(0)} = 0$  and  $H^{(1)}$ . Similarly,  $M_{\alpha\beta}^{(1)}$  depends on the tensor  $\dot{K}_{\alpha\beta}^{(1)} = H_{,\alpha\beta t}^{(1)} + u_\gamma^{(0)} H_{,\alpha\beta\gamma}^{(1)}$ . Since the velocities  $(u_x^{(0)}, u_y^{(0)})$  we compute are perturbations of order one around the simple translational state  $(U = 1, 0)$ , the advection velocity is limited to  $u_\gamma^{(0)} = \delta_{\gamma x}$  as products  $\text{Je} \bar{u}_\gamma^{(0)} H_{,\alpha\beta\gamma}^{(1)}$  are of order 2 ( $\text{Je}$  and  $H^{(1)}$  are both small quantities). Hence  $\dot{K}_{\alpha\beta}^{(1)} = H_{,\alpha\beta t}^{(1)} + H_{,\alpha\beta x}^{(1)}$  when we retain only first order terms.

We can further develop the second integral of expression (3.17) into:

$$\begin{aligned} & \int 2(u_{(\alpha,\beta)}^{(1)} + \delta_{\alpha\beta} u_{(\gamma,\gamma)}^{(1)}) \hat{u}_{\alpha,\beta} \\ & + \int N_{\alpha\beta}^{(0)} H_{,\alpha}^{(1)} \hat{w}_{,\beta} + \frac{\varepsilon^2}{6} \left( H_{,\alpha\beta t}^{(1)} + H_{,\alpha\beta x}^{(1)} + \delta_{\alpha\beta} (H_{,\gamma\gamma t}^{(1)} + H_{,\gamma\gamma x}^{(1)}) \right) \hat{w}_{,\alpha\beta} = 0 \end{aligned} \quad (3.18)$$

This weak form defines two uncoupled problems on the independent virtual displacements  $\hat{u}_\alpha$  and  $\hat{w}$ . We recall that problems were similarly decoupled in the case of the Elastica. The first line of equation (3.18) regroups all terms involving perturbations in the velocities  $u_\alpha^{(1)}$ . It corresponds to a purely planar perturbation of the system, which would correspond to an axial destabilization of the curtain. We assume that the stationary solution obtained is stable in this regard, and are interested in an instability involving out of plane displacements.

The second line of equation (3.18) defines a non trivial problem on the out of plane displacement  $H^{(1)}$ . This problem has physical solutions for specific values of the parameters  $(\beta, \text{Je}, \varepsilon)$  that can be obtained by studying this equation as an eigenvalue problem, similarly to the method described in the case of the Elastica in §2.3.2. We will search for the thickness, i.e. its corresponding parameter  $\varepsilon$ , at which the curtain loses stability with respect to an out-of-plane perturbation. Using a finite elements solver we will obtain corresponding global modes and their growth rate. We describe eigenmodes as a global out of plane displacement mode of the curtain times a time dependent complex exponential  $H^{(1)} = \tilde{H}(x, y) e^{-i\omega t}$ . This simple exponential time dependence is possible because we perturb linearly a stationary base flow. We will separate time dependent terms in order to write down a generalized eigenvalue problem.

$$\int \bar{N}_{\alpha\beta}^{(0)} \tilde{H}_{,\alpha} \hat{w}_{,\beta} + \frac{\varepsilon^2}{6 \text{Je}} \left( \tilde{H}_{,\alpha\beta x} + \delta_{\alpha\beta} \tilde{H}_{,\gamma\gamma x} \right) \hat{w}_{,\alpha\beta} = \int \frac{\varepsilon^2 i \omega}{6 \text{Je}} \left( \tilde{H}_{,\alpha\beta} + \delta_{\alpha\beta} \tilde{H}_{,\gamma\gamma} \right) \hat{w}_{,\alpha\beta} \quad (3.19)$$

To expose the way numerical implementation will be done, this equation can be formally written:

$$A(\beta, \frac{\varepsilon^2}{\text{Je}})(\tilde{H}, \hat{w}) = i\omega B(\frac{\varepsilon^2}{\text{Je}})(\tilde{H}, \hat{w}) \quad (3.20)$$

Writing the equation in this manner is a good way to exhibit the fact that this problem is a generalized eigenvalue problem for the eigenvalue  $\lambda = i\omega$ . It also reveals that the out-of-plane stability problem only depends on two parameters,  $\beta$  and  $\frac{\varepsilon^2}{\text{Je}}$ . At the moment,  $A(\beta, \frac{\varepsilon^2}{\text{Je}})$  and  $B(\frac{\varepsilon^2}{\text{Je}})$  represent differential operators that need to be discretized in the finite element implementation.  $A(\beta, \frac{\varepsilon^2}{\text{Je}})$  depends on parameter  $\beta$  through terms involving the base solution. As Jeffreys number has been rescaled by looking for a linearized solution in  $\text{Je}$ , the base solution depends only on the aspect ratio  $\beta$ . Calculation of the operator  $A(\beta, \frac{\varepsilon^2}{\text{Je}})$  requires to first choose a value for  $\beta$ , and then solve for the base solution.

$\tilde{H}(x, y)$  is the eigenvector and represents the deformed shape of the curtain as it loses stability. It is obtained numerically, along with its associated eigenvalue  $i\omega$ , and takes complex values on the domain of the curtain.

All time dependent terms are collected in the operator  $B(\frac{\varepsilon^2}{\text{Je}})$  that will become the mass matrix in the numerical scheme, while  $A(\beta, \frac{\varepsilon^2}{\text{Je}})$  captures all other terms, including those involving the base solution as mentioned earlier, and is called the stiffness matrix in the numerical eigenvalue problem.

We will cover in the next chapter the numerical implementation of the equations we have obtained and the calculation of the phase diagram in the  $(\beta, \frac{\varepsilon^2}{J_e})$  plane. As discussed in part I of this manuscript, the order of the equations is of great importance when numerical solutions are sought. We encounter the highest derivative orders in the final equations we have written for the stability analysis. When discussing boundary conditions in §3.2.3 we mentioned the fact that advective effects increase the order of the equations by one because of the comoving derivative. The highest order term of equation (3.19) is  $\frac{\varepsilon^2}{6J_e} \delta_{\alpha\beta} \tilde{H}_{,\gamma\gamma x} \hat{w}_{,\alpha\beta}$ , with order 3 on  $\tilde{H}$  and 2 on  $\hat{w}$ . This means the equivalent strong form of the equations has derivatives in space of order 5. We will see in the next chapter how this problem is implemented in a high order finite element scheme.





## Contents

<b>4.1 Base planar solution</b>	<b>55</b>
4.1.1 Reconstruction of particle trajectories	56
4.1.2 Extensional and compressive flow	59
<b>4.2 Wrinkled curtain</b>	<b>60</b>
4.2.1 Linear stability analysis	60
4.2.2 Simplified discontinuous Galerkin method	61
4.2.3 Numerical buckling modes	61
<b>4.3 Phase diagram</b>	<b>64</b>
<b>4.4 Effect of capillarity</b>	<b>66</b>
4.4.1 Influence of capillarity on the base solution	67
4.4.2 Phase diagram	68

# Numerical implementation

WORKING WITH equations obtained in the previous chapter, we will want to implement a finite element scheme in order to solve them. We will discuss other possible methods of resolution and motivate our choice of using finite elements. Equations we study are of relatively high order and we will also point out one of the limitations of the method and how to overcome it.

## 4.1 Base planar solution

We recall here the weak form of the equations for the velocities  $u_x^{(0)}$  and  $u_y^{(0)}$ :

$$\int -\bar{N}_{\alpha\beta}^{(0)} \hat{u}_{(\alpha,\beta)} + \hat{u}_x = 0 \quad (4.1)$$

with  $\bar{N}_{\alpha\beta}^{(0)} = 2(\bar{u}_{(\alpha,\beta)}^{(0)} + \delta_{\alpha\beta} \bar{u}_{\gamma,\gamma}^{(0)})$  and boundary conditions from the first column of table 3.1.

As mentioned earlier, this set of equation is analogous to the equations depicting an elastic plate under applied load in the direction  $x$ . Since the domain is rectangular, this problem can be solved analytically using series expansions [Rib08]. Such expansions must take into account boundary conditions and can become impractical if those are hard to satisfy. In our case of the curtain, boundary conditions on the top corners are

numerically difficult, as they match an injection velocity with a stress free edge. This means that a very large number of terms in the series is required in order to converge in the corners. By preferring a finite elements method, we can use adaptive mesh refinement to get the required precision near corners, while keeping a coarser mesh in the rest of the domain. The velocity field that develops in the curtain is close to a vertical flow of velocity  $U$  but does present a vertical acceleration, along with a lateral velocity directed towards the centre of the sheet. A visualization of the velocity field is presented in figure 4.1.

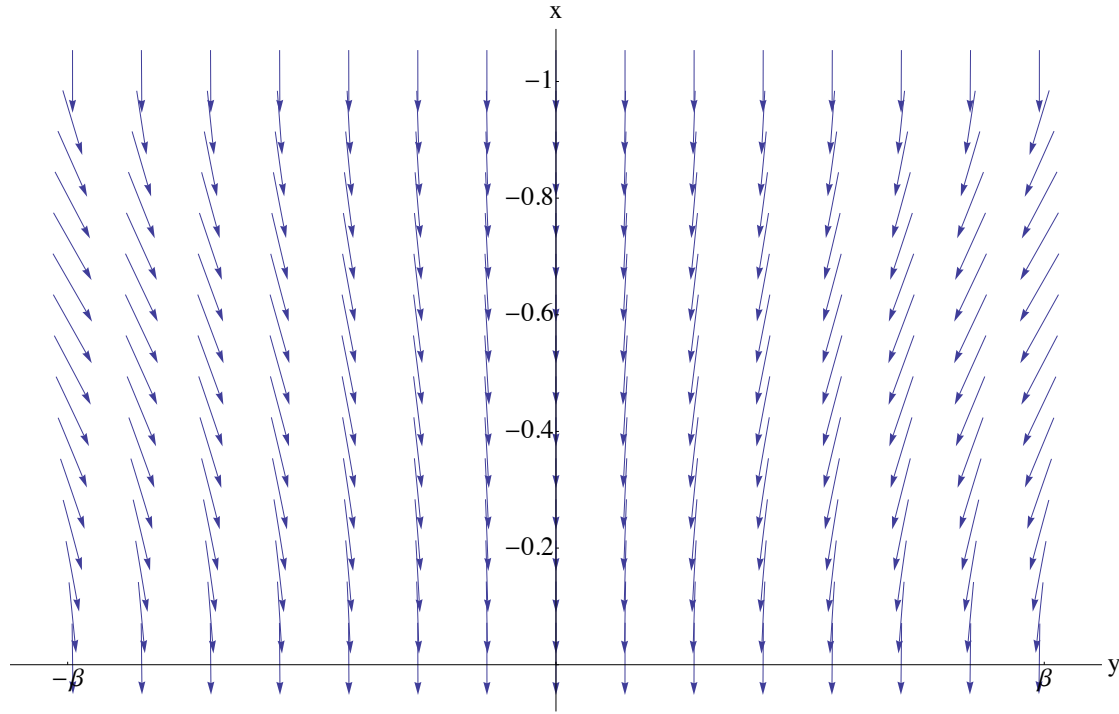


Figure 4.1: Vector field representing the stationary flow that develops in the falling curtain  $(u_x^{(0)}, 12 u_y^{(0)})$ . The transverse component of the velocity  $u_y^{(0)}$  has been magnified to aid visualization. The injection speed  $U$  is equal to 1 after rescaling,  $Je$  was set to 1 for this representation,  $\beta = 0.8$ .

The numerical scheme used to obtain the above figure is based on a mesh of rectangular elements (QUAD4) homogeneously generated by the finite elements library we use, see §4.2.2 for details on the type and family of elements. After multiple refinements of the mesh, the total number of degrees of freedom is of the order of  $10^4$ .

#### 4.1.1 Reconstruction of particle trajectories

In the previous derivation we have assumed the thickness of the curtain to remain constant over the length of the fall. This is consistent, as the relative changes in thickness are small in the limit  $Je \ll 1$ . Now that we have found horizontal velocities flowing inwards, we will quantify the small change in width of the sheet. This phenomenon is driven by conservation of volume. Particles are accelerated downwards, which stretches volume elements, through volume preservation, we expect fluid elements to become thinner in

the two orthogonal directions.

In order to confirm that the approximation of constant thickness and rectangular domain of study are right, we want to evaluate the amount of deformation that is induced. In a steady flow, flow lines on the sides of the domain follow its edges. Hence a differential equation for the shape of the edges can be obtained by evaluating  $\frac{dy}{dx} = \frac{u_y(x, \pm\beta)}{u_x(x, \pm\beta)}$  and integrating it along the vertical axis  $x$ .

$$\begin{aligned}
 \frac{dy}{dx} &= \frac{u_y(x, \beta)}{u_x(x, \beta)} \\
 \frac{dy}{dx} &= \frac{\text{Je } \bar{u}_y^{(0)}(x, \beta)}{U + \text{Je } \bar{u}_x^{(0)}(x, \beta)} \\
 \frac{dy}{dx} &= \frac{\text{Je } \bar{u}_y^{(0)}(x, \beta)}{U} \left(1 - \frac{\text{Je } \bar{u}_x^{(0)}(x, \beta)}{U}\right) \\
 \frac{dy}{dx} &\approx \frac{\text{Je } \bar{u}_y^{(0)}(x, \beta)}{U}
 \end{aligned} \tag{4.2}$$

This differential equation can be integrated along the height of the sheet following coordinate  $x$  at positions  $y = \pm\beta$  to find the shape of the edges. We show the shape of the deformed curtain exaggerating its reduction in width in figure 4.2.

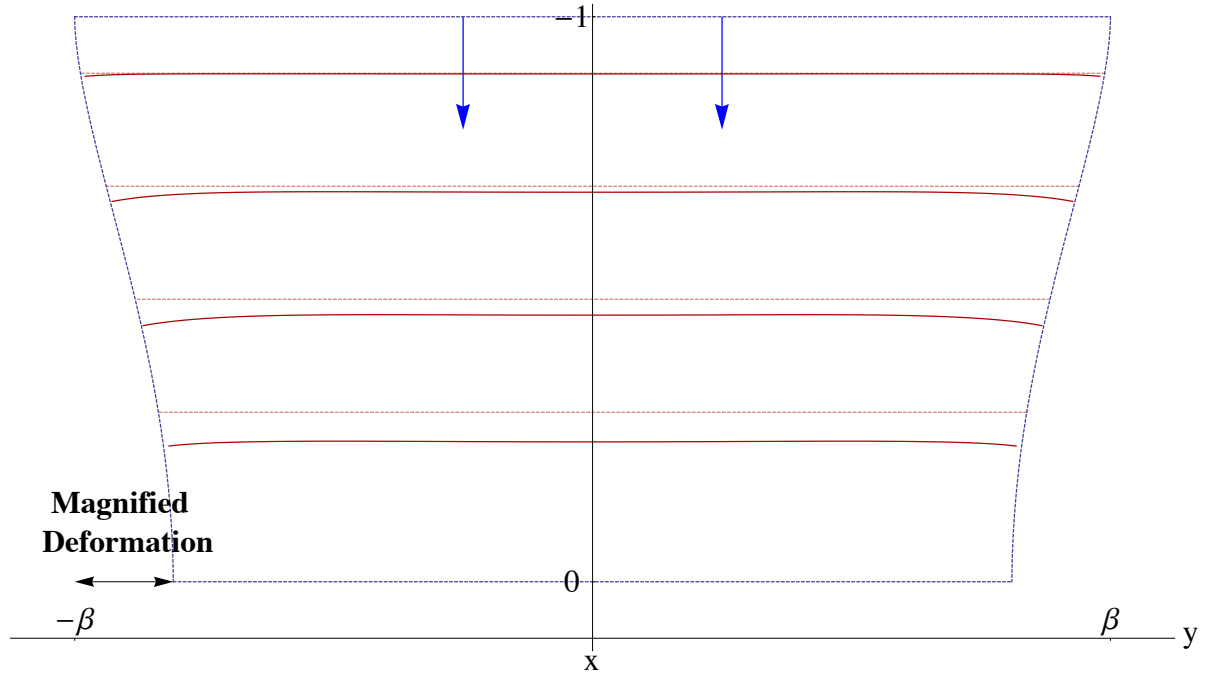


Figure 4.2: Shrinking of the curtain due to incompressibility. As velocities that develop in the horizontal direction are small, the overall deformation of the sheet is small. This is also stands for the thickness. Lateral deformations are magnified five times by using  $Je = 5$ , the velocity field used to plot this image corresponds to  $u_\alpha^{(0)} = \delta_{\alpha x} + 5 \bar{u}_\alpha^{(0)}$ . Red curves in the flow represent material lines of particles that were injected at the same time instant, red dashed lines indicate the height in the flow where these curves are calculated.

The shrinking effect has been amplified to aid visualization but is actually small due to the fact that the ratio  $\frac{Je}{U}$  that appears in equation (4.2) is a small number. Hence the change in width is small. Correcting the geometry of the curtain to take into account those deformations would lead to higher order terms that we would drop after linearization. As explained earlier this approximation allows one to reformulate the initial stability problem, which involves free boundaries, into a problem on a fixed, rectangular domain.

It is worth noting that this shrinking in the orthogonal directions can be explained by analogy with a solid mechanics phenomenon called Poisson's effect. An elastic object stretched in one direction will shrink in the two other orthogonal directions in order to keep a constant volume. The amount of shrinking is quantified by Poisson's number  $\nu$  and it takes the value  $1/2$  for an incompressible material. This number is material dependent, some materials have a Poisson's ratio of 0, which means they can stretched (or compressed) with no effect on their boundaries. Think of a sponge as an illustration of such material, when it is compressed, it mostly retains its rectangular shape. Another interesting property of solid materials is that they can have a negative Poisson's ratio, i.e. a solid that shrinks in all directions when compressed, or that expands as it is being pulled on. This kind of behaviour is very unnatural for a fluid and is never observed.

Stokes-Rayleigh analogy only draws a relation between the form of the equations. Viscous moduli are related to the elastic moduli, and if we want to carry the analogy to define Poisson's ratio, we have to look at the viscous strain rate tensor. Note that this will only lead to the definition of a two-dimensional Poisson's ratio. We obtain the relation  $d_{xx} = N_{xx} - \frac{1}{2}N_{yy}$  and conclude that the analogous two-dimensional Poisson's ratio is one half. Because it is a two-dimensional definition, this value does not lead to conservation of area.

#### 4.1.2 Extensional and compressive flow

The steady planar flow that develops in the falling curtain is a vertically accelerated flow, which induces stretching in the vertical direction, along with a horizontal inward flow, creating compressive stresses.

In order to visualize where the curtain is under compressive stresses, we plot the smallest eigenvalue of the local stress tensor on a colour map. The velocities obtained by solving for the planar flow can be used to calculate the values of this tensor everywhere in the domain. We denote the ordered principal stresses of tensor  $N_{\alpha\beta}$  by  $N_I$  and  $N_{II}$  with  $N_I < N_{II}$ , such that  $\det(\underline{N} - \lambda \underline{Id}) = (\lambda - N_I)(\lambda - N_{II})$ . Red zones of figure 4.3 represent regions having at least one direction of compressive stress where  $N_I < 0$ , while blue colour indicates a zone where the stress is tensile in all directions ( $N_I > 0$ ). In the red zone, the viscous sheet is stretched vertically, but compressed in the horizontal direction. In the blue zone, it is stretched in both directions.

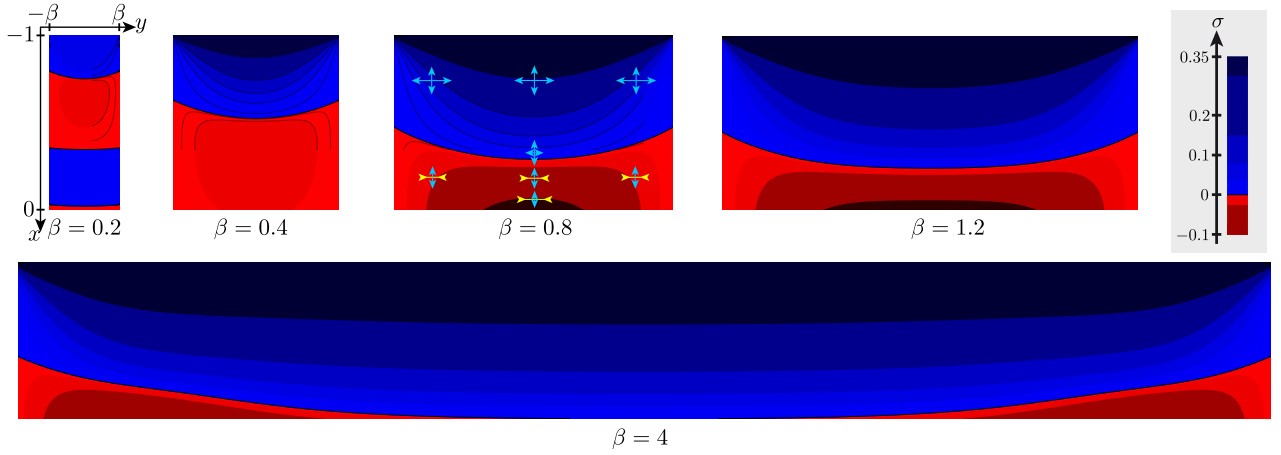


Figure 4.3: Visualization of the most negative eigenvalue (denoted by  $N_I$  in §4.1.2) of the local stress tensor  $N_{\alpha\beta}$ , for the planar base solutions of different aspect ratios  $\beta$ . Red zones are under compression, while blue zones are stretched. Consistent with our approximation  $Je \ll 1$ , all stress fields are shown in a rectangular domain  $-\beta < y < \beta$  and  $0 < x < 1$ : the small lateral contraction of the curtain is not represented. Arrows overlaid to aspect ratio  $\beta = 0.8$  represent the directions of the two eigenvectors of the local stress tensor, with a length proportional to their corresponding eigenvalue. Light-blue and yellow arrows respectively indicate positive and negative eigenvalues. Note that compressive directions are very close to the horizontal.

As displayed in figure 4.3, stresses in the vertical  $x$  direction are always tensile, while

compressive stresses appear in the horizontal  $y$  direction. The shape of the compressed zone is very dependent on the aspect ratio of the curtain. We can see that for lower values of  $\beta$ , the most compressed zone is along the centreline. This zone seems to be moving down as  $\beta$  increases, and before reaching the bottom of the curtain, this zone separates in two symmetric patches that move towards the exterior of the curtain. For large aspect ratios  $\beta$ , compressive zones localize at the bottom corners of the curtain.

In the next section we will restore effects of bending in the sheet, in order to study the possibility of buckling instabilities driven by compressive stress. The base solution was obtained as linearized in Jeffreys number  $Je$ , hence the planar base flow only depends on one parameter, the aspect ratio  $\beta$ .

## 4.2 Wrinkled curtain

We have obtained the base flow that develops in the curtain as it falls down as a function of aspect ratio  $\beta$  and the study of local stresses reveals that some regions of the curtain are prone to buckling. The compressive stresses can drive a buckling instability, and we expect the liquid sheet to become unstable provided it is thin enough. We will find the threshold for this instability in following sections.

### 4.2.1 Linear stability analysis

In part I, at this step of the analysis we needed to include inertial terms in order to add an explicit time dependence for the eigenmodes. In the case of the curtain, the viscous constitutive law applied to the bending strain rate tensor gives rise to time dependent terms. These contribute to the stiffness matrix  $B$  of the generalized eigenvalue problem described in §3.3.4. As a result, there is no need to introduce inertia for the stability analysis.

If we want to derive the strong form of the equations, we will integrate by parts equation (3.19). In this equation, the term responsible for the contribution of highest derivation order is the product  $\tilde{H}_{,\alpha\beta x} \hat{w}_{,\alpha\beta}$ . After integration by parts, this term leads to a fifth order derivative in space. The origin of this term is of course the comoving derivative, and more specifically its advective part that raises the order of the equations by one with the operator  $\underline{u}^{(0)} \cdot \frac{d}{dx}()$ .

When solving partial differential equations of order two or less, the finite elements method relies on continuous ( $C^0$ ) functions for its bases of test and trial functions. These equations have a weak form that involve only first order derivatives and those can be accessed locally with  $C^0$  functions. In the case of higher order equations, one way of dealing with derivatives is to implement higher order bases of test and trial functions. Hence some finite element libraries, including the one we use, `libmesh`, provide  $C^1$  function bases. These bases of functions give access to local second order derivatives on the finite elements. This means that corresponding strong forms that can be solved are now up to order four differential equations.

However, as mentioned previously at the end of §3.3, our problem is of fifth order in space derivatives. Hence using  $C^1$  functions is still not enough to handle the fifth order differential equation we want to solve. Although it only seems natural to try to implement bases of even higher order class for the test and trial functions, this is not a simple process and isn't available in the finite elements library we use.

### 4.2.2 Simplified discontinuous Galerkin method

We will use ideas coming from the discontinuous Galerkin method with interior penalties in order to solve our fifth order finite elements problem. We will use an adaptation of the method in order to keep the advantage of using  $C^1$  elements.

In the discontinuous Galerkin method, no continuity is required across element boundaries, but weak formulations become a bit more complex. The main idea we will use of is to assign each order of derivation to a different variable [XS08]. Instead of working only with the kinematic variable  $H$ , which would limit us to its second order derivatives, we introduce a new variable, let us call it  $\Theta$ , such that  $\Theta = H_{,x}$ . By using finite elements with  $C^1$  shape functions for  $\Theta$ , we have access to its second order derivatives, which are equal to some of the third order derivatives of  $H$ .

$$\Theta_{,\alpha\beta} = H_{,x\alpha\beta} \quad (4.3)$$

Note that we cannot access all third order derivatives as  $H_{,yyy}$  isn't available. However, this is not an issue as this term does not appear in equation (3.19). We can now use  $\Theta_{,xx}$  instead of  $H_{,xxx}$ . For lower order derivatives, using  $\Theta$  or  $H_{,x}$  makes no difference. In fact, we monitor the value of the residues  $\Theta - H_{,x}$  and  $\Theta_{,x} - H_{,xx}$  and check that they cancel.

In order to impose the equality of two a priori independent kinematic variables, we introduce a constraint equation along with a penalty parameter  $\Lambda$  of the form

$$\Lambda \int (\Theta - H_{,x}) \hat{\Theta} \quad (4.4)$$

The penalty parameter  $\Lambda$  has to be large enough to warrant accuracy but generally needs to be increased from the value  $\Lambda = 1$  only if a discrepancy is observed. Implementing this additional equation in the finite elements scheme, we need to choose a basis for the test and trial functions.

As mentioned earlier, we work on a rectangular domains and require the use of  $C^1$  elements. We choose third order Hermite polynomials on rectangular elements for both  $H$  and  $\Theta$ . These elements are known as the Bogner-Fox-Schmidt rectangle elements and are a good choice for thin plate analysis [Rus08]. Each rectangular element shares 4 nodes with its neighbours. Each node contains 4 degrees of freedom, for a total of 16 degrees of freedom per rectangle, shared with its neighbours. At each node the list of degrees of freedom is  $\text{DOFs}_w = w, w_{,x}, w_{,y}, w_{,xy}$ , a value, the two first order derivatives along the in plane directions and the crossed second order derivative.

### 4.2.3 Numerical buckling modes

We have already obtained the planar base flow for each aspect ratio  $\beta$ , and we have now restored bending effects in the viscous sheet that involve the additional parameter  $\frac{\varepsilon^2}{\text{Je}}$ , corresponding to the thickness squared of the sheet. After solving numerically the generalized eigenvalue problem defined in §3.20 the most unstable mode is given by the largest growth rate  $\text{Im}(\omega)$ . For thicker sheets, no positive growth rate that would correspond to an unstable mode is present. But as the thickness of the curtain is reduced, the growth rate of the most unstable mode becomes positive and the corresponding eigenvector turns into an unstable and growing deformation of the sheet. We can compute the shape of the first eigenvectors that become unstable for different aspect ratios  $\beta$  which are represented in figure 4.4.



When studying numerical results from a generalized eigenvalue solver, some steps must be taken in order to identify physical modes. In general, matrices used for solving must be well conditioned. This evaluates their sensibility to very small changes in initial conditions (e.g. the number of nodes used in calculation), however pre conditioners are readily implemented by eigensolvers, and ill-conditioned problems are easy to identify. The number of eigenvalues that can theoretically be obtained by the solver is equal to the rank of the matrix  $B^{-1}A$ , but this is a very large matrix. Hence we have to specify the domain of the complex plane where we will be looking for eigenvalues.

It is possible to follow the value of the growth rate as the thickness is reduced and crosses the instability threshold. Growth rate starts with negative values, and becomes positive as thickness is reduced, corresponding to unstable configurations. Evolution of the growth rate along a path will be shown in the next section §4.4.2. Densely packed around the zero eigenvalue lie many so called grid modes with no physical meaning. These modes look very jagged (with a wavelength of the order of the mesh size) and are easy to filter out from modes having physical significance. As we are studying the onset of the instability, we want the imaginary part of  $\omega$  to change sign and we will concentrate the research around  $\text{Im}(\omega) \gtrsim 0$ .

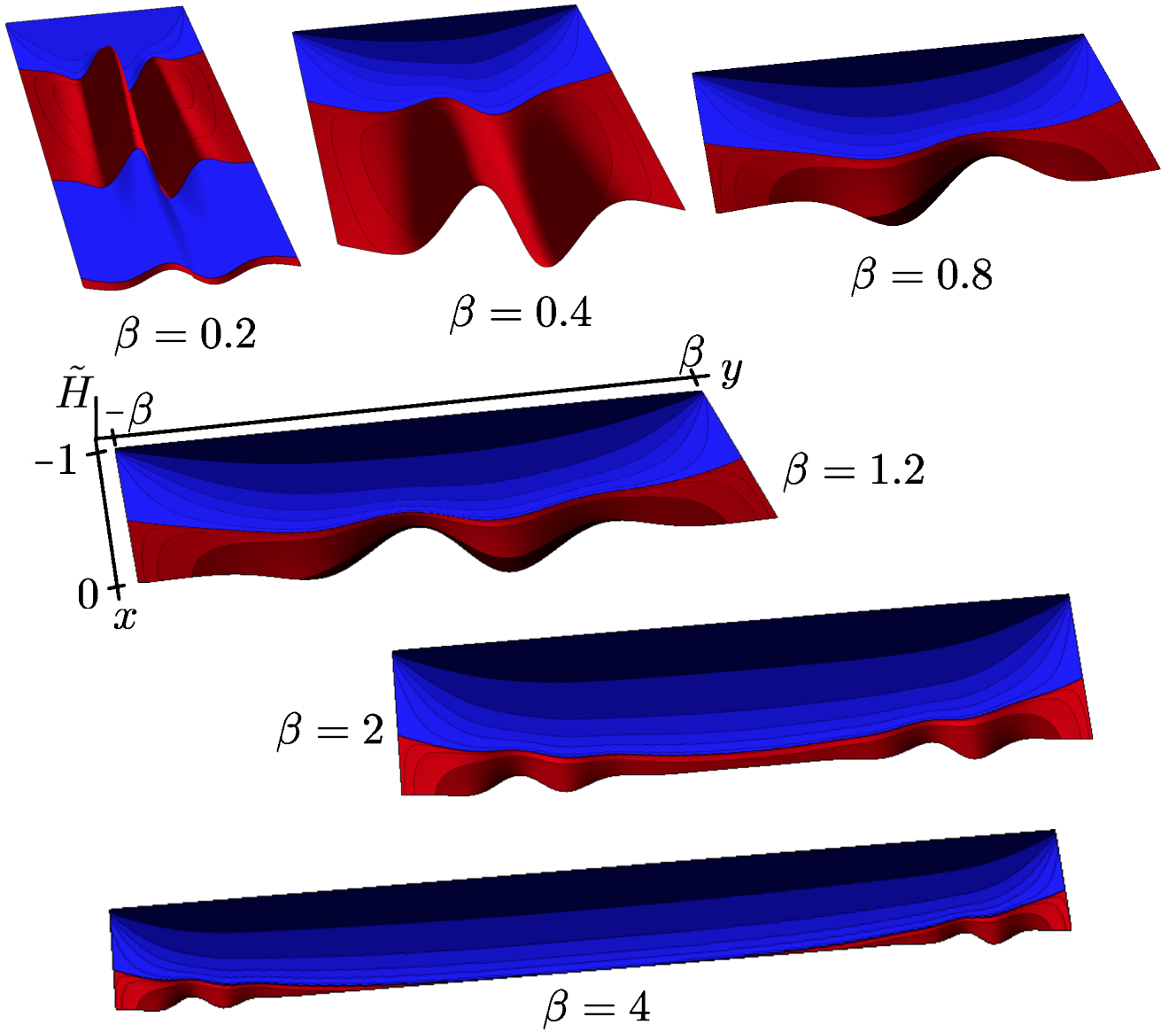


Figure 4.4: Shape of the most unstable buckling mode for different aspect ratios displayed with an arbitrary amplitude. The growth rate  $\text{Im}(\omega)$  is chosen very small and corresponds to the onset of the instability, values of the parameter  $\frac{\varepsilon^2}{\text{Je}}$  corresponding to these images are as follows:  $\beta = 0.2$ ,  $\frac{\varepsilon^2}{\text{Je}} = 10^{-6.9}$ ;  $\beta = 0.4$ ,  $\frac{\varepsilon^2}{\text{Je}} = 10^{-5.8}$ ;  $\beta = 0.8$ ,  $\frac{\varepsilon^2}{\text{Je}} = 10^{-4.5}$ ;  $\beta = 1.2$ ,  $\frac{\varepsilon^2}{\text{Je}} = 10^{-4.5}$ ;  $\beta = 2$ ,  $\frac{\varepsilon^2}{\text{Je}} = 10^{-4.9}$ ;  $\beta = 4$ ,  $\frac{\varepsilon^2}{\text{Je}} = 10^{-5.0}$ . For values of  $\beta$  smaller than 1.2 in this image, the growth rate is purely imaginary, while  $\text{Re}(\omega)$  is non zero for larger aspect ratios (oscillatory modes). See figure 4.5 to visualize these values on the phase diagram  $\frac{\varepsilon^2}{\text{Je}}(\beta)$ .

We retained colours of the local stability analysis in this picture and it can be seen that deformation of the curtain is initiated in the locally compressive regions. This indicates good qualitative agreement between the stress map visualization and the global numerical stability scheme, however local stresses can only serve as an indicator for unstable regions. As expected from the stress map, for larger aspect ratios deformation localizes near the bottom corners of the curtain, the deformation of largest amplitude is no longer close to the centreline.

In the simplest analogy with a buckling phenomenon, one expects a compressed system to buckle with the largest wavelength possible in the domain. In the case of the Elastica, the longest available wavelength is set by the length of the beam, and if no other constraints are applied it is the one that appears first. In the case of a constrained Elastica, between parallel plates for example, modes of higher order and shorter wavelengths can be preferred. In the case of the viscous curtain, higher order modes are selected, potentially because compressive zones aren't homogeneous and only cover limited regions of the flow: the length scale of the buckling mode reveals the typical lengths present in the map of pre-stress.

In the analogous elastic version of the problem where a sheet of elastic material is clamped on both sides and stretched, wrinkles of rather small wavelength appear. Numerous numerical studies of this problem lead to predictions for the number of wrinkles and their amplitude. It is worth noting that results obtained here are qualitatively similar to those obtained in numerical studies of the elastic case. The differences, mainly due to the effects of advection are particularly visible for larger aspect ratios.

### 4.3 Phase diagram

As described earlier, we obtain the growth rate of the most unstable eigenmode for each pair  $(\beta, \frac{\epsilon}{\text{Je}})$ . We are interested in the value of the thickness at which the curtain loses stability. We can plot a phase diagram with two distinct zones. For small thickness, the curtain is unstable, while in the upper part of the diagram the curtain is stable.

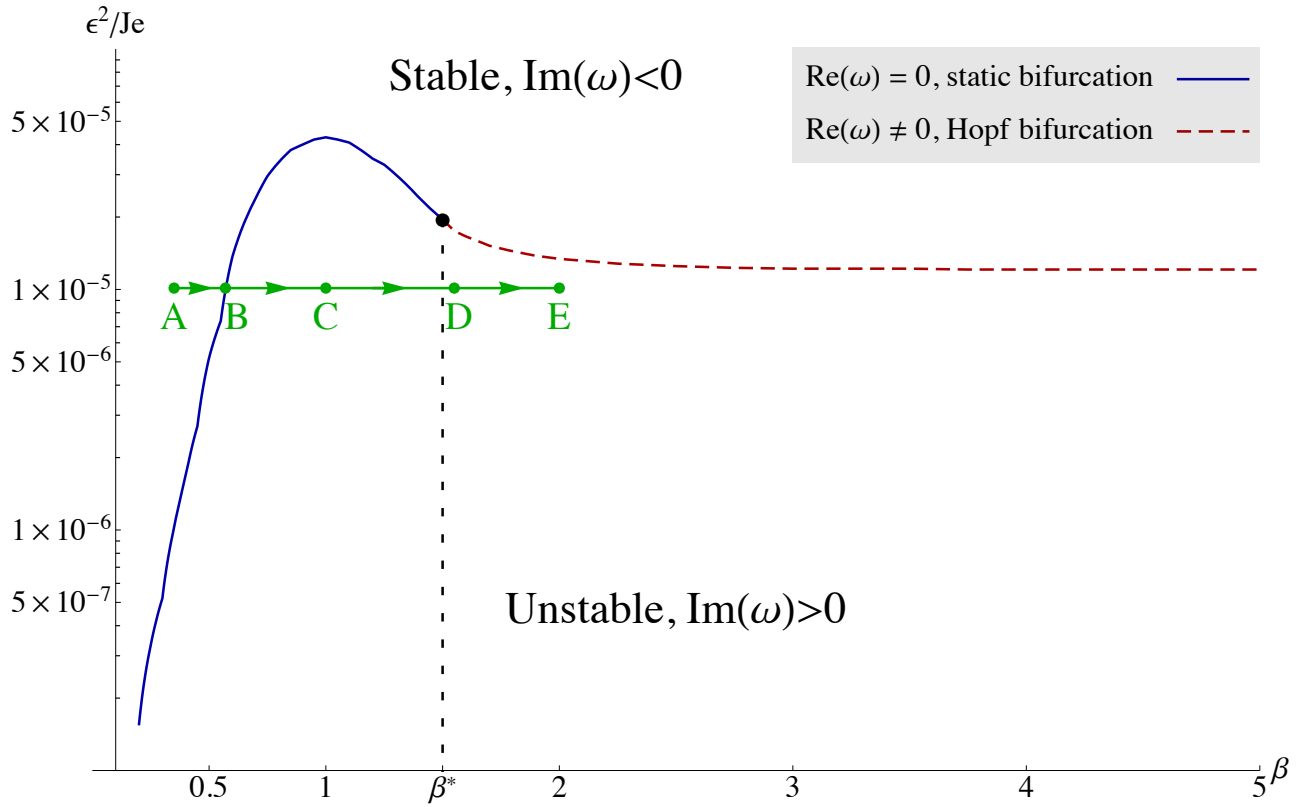


Figure 4.5: Phase diagram in the plane  $(\beta, \frac{\epsilon^2}{J_e})$  depicting the stability of the viscous curtain. The horizontal axis is the aspect ratio of the curtain, wider curtains are on the right of the diagram. The vertical axis is the dimensionless parameter corresponding to the thickness squared, the contour separates larger thicknesses on the top of the diagram where the curtain is stable ( $\text{Im}(\omega) < 0$ ) from the unstable zone of lower thicknesses at the bottom (where  $\text{Im}(\omega) > 0$ ).

The most unstable aspect ratio is around  $\beta = 1$ , a curtain twice as large as it is high. The eigenvalue associated with each mode  $\omega$  is complex, and we have already seen that its imaginary part is the growth rate of the mode. A non zero real part for  $\omega$  is an oscillatory term (complex exponential) that multiplies the amplitude of the eigenvector. Hence it means the deformation has a periodic amplitude, and the solution is oscillating.  $\beta^*$  marks the separation between purely imaginary eigenvalues and eigenvalues with a non zero real part, indicating oscillatory amplitude. In both cases the corresponding modes will grow or be dampened depending on the sign of  $\text{Im}(\omega)$ . The position of the aspect ratio  $\beta^*$  is independent of Jeffreys number and separates two types of bifurcations.

Referring to nonlinear dynamics, we can relate the bifurcations we observe and their properties with standard linear stability analysis. Purely imaginary eigenvalues can be related to a pitchfork bifurcation, in which the variation of a parameter is associated to a destabilization of the system, following an unstable branch (static bifurcation). Eigenvalues with a nonzero real part correspond to oscillating modes and can be related to a Hopf bifurcation, with a destabilization of the system leading to a limit cycle.

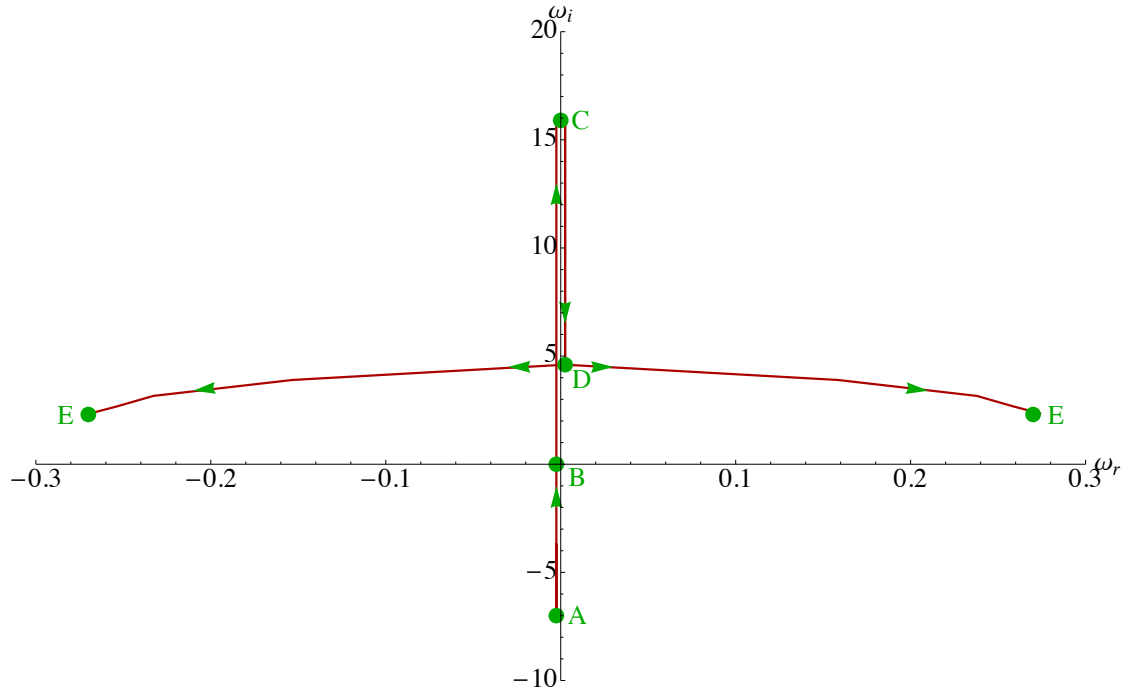


Figure 4.6: Motion of the growth rate of the most unstable eigenmode in the complex  $\omega$  plane, as we follow the path from A to E in the phase diagram of figure 4.5. B is the boundary between stable and unstable aspect ratios for the chosen thickness  $\varepsilon^2 = 10^{-5}$ . C corresponds to the most unstable aspect ratio, and D marks the boundary between the fixed and oscillatory modes.

Travelling along a path of constant thickness  $A \rightarrow E$  indicated on figure 4.5, the eigenvalue of the largest growth rate reaches positive imaginary parts as it crosses the instability threshold at point B. The eigenvalues of the most unstable mode are represented on figure 4.6 as we move along the path  $A \rightarrow E$ .

## 4.4 Effect of capillarity

Capillary action tends to minimize the surface occupied by a liquid. While its effect is small, especially in a very viscous liquid, it tends to reduce the section of the curtain and will lead to a faster reduction of its width. This effect increases the amount of lateral compression in the curtain. However, when the curtain loses width, its thickness is expected to increase. On the one hand, this effect increases the compressive stresses that would drive the instability, but on the other hand increased thickness tends to stabilize the system. The most important effect concerns the out of plane deflection, as capillary effects try to limit augmentation of the sheet's surface, it prevents out of plane movements that would add to the sheet's length.

By following these two qualitative guesses, we expect the base flow to not change much when capillary effects are restored, while we expect buckling to happen for thinner sheets, increasing the buckling threshold and stabilizing the curtain.

#### 4.4.1 Influence of capillarity on the base solution

Capillarity can be taken into account using the same numerical method, simply by restoring the term involving  $\text{Ca}$  in our equations. It has to be taken into account at both steps of the study, when deriving the base solution as well as when studying its stability. Concerning the derivation of the base flow, in §3.3 the important equation is the weak form presented in equation (3.16). When considering a non-zero capillary number this equation becomes:

$$\int -\bar{N}_{\alpha\beta}^{(0)} \hat{u}_{(\alpha,\beta)} + \hat{u}_x - \frac{1}{\text{Ca} \varepsilon \text{Je}} \hat{u}_{\alpha,\alpha} = 0 \quad (4.5)$$

As mentioned earlier, this term should modify quantitatively but not qualitatively the base flow that develops in the curtain. For a chosen aspect ratio, we can compare the local stress maps with and without capillary forces. We can observe on figure 4.7 that

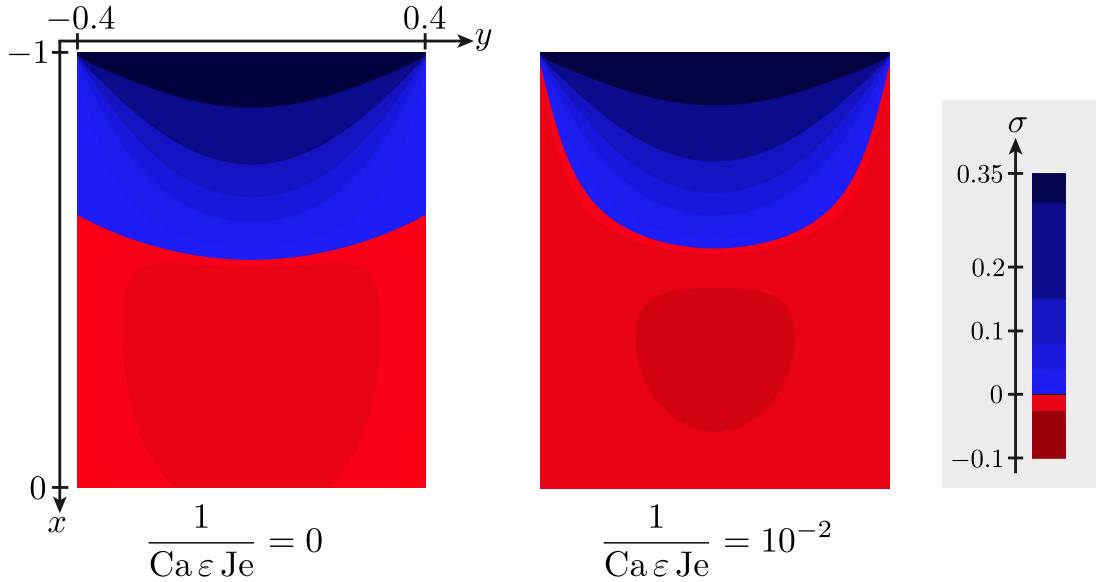


Figure 4.7: Local stress maps for aspect ratio  $\beta = 0.4$  with no capillary effect (left) and restored capillary number  $\text{Ca}$  (right).

the effect of capillary effects are mostly visible on the sides of the curtain. As capillary forces tend to reduce the width of the curtain, compressive stresses are present earlier near the edges of the curtain. Overall, the stress map remains qualitatively similar.

Capillarity does not only modify the calculation of the base solution (hence the map of pre-stress), it also introduces new terms in the eigenvalue problem. Indeed, we also have to restore a term in the weak form governing the out of plane equilibrium (3.17):

$$\begin{aligned} & \int (-N_{\alpha\beta}^{(0)} \hat{u}_{(\alpha,\beta)} + \text{Je} \hat{u}_x - \frac{1}{\text{Ca} \varepsilon \text{Je}} \hat{u}_{(\alpha,\alpha)}) \dots \\ & \dots - \int (N_{\alpha\beta}^{(1)} \hat{u}_{(\alpha,\beta)} + N_{\alpha\beta}^{(0)} H_{,\alpha}^{(1)} \hat{w}_{,\beta} + \varepsilon^2 M_{\alpha\beta}^{(1)} \hat{w}_{,\alpha\beta} + \frac{1}{\text{Ca} \varepsilon \text{Je}} H_{,\alpha}^{(1)} \hat{w}_{,\alpha}) = 0 \end{aligned} \quad (4.6)$$

Similarly to the previous situation, we have two uncoupled problems to solve. One for the virtual velocities  $\hat{u}_x$  and  $\hat{u}_y$ , the other for the virtual displacement  $\hat{w}$ . Following

the exact same argument, the first problem has a null solution, while the second one leads to solutions with non zero out of plane displacements. Boundary conditions were already exposed with their full dependence in the parameter  $Ca$  in table 3.2. Numerical implementation follows the same method as described earlier.

#### 4.4.2 Phase diagram

In order to clearly visualize the effect of restoring a non zero capillary number we compute a new phase diagram  $(\beta, \frac{\epsilon^2}{Je})$  and observe how the boundary corresponding to marginal stability is affected.

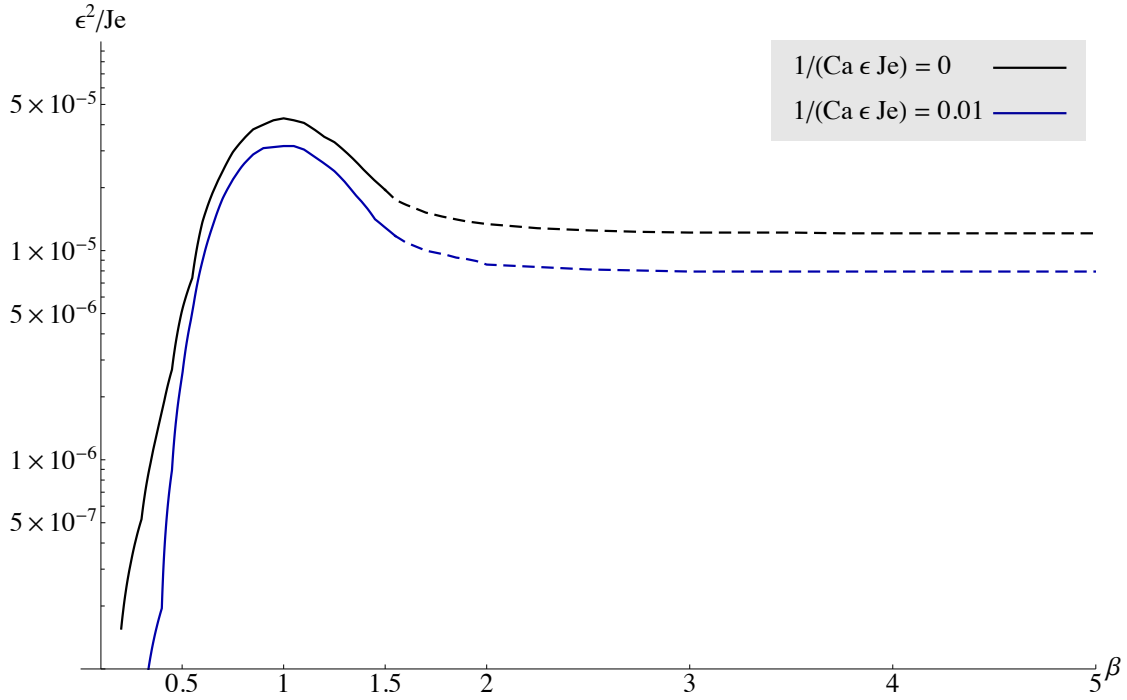


Figure 4.8: Effect of the capillary forces on the stability diagram of the falling curtain. Notations in use are the same as in the phase diagram of figure 4.5.

We observe that the separation between stable and unstable domains moves down. This could be expected, as the curtain is on average more stable with capillary effects acting, hence a smaller thickness is required to reach the instability threshold.

## Partial conclusion

In chapter 3 we described the geometry and equations governing the falling viscous curtain. We defined both the kinematics and the constitutive relations and made use of the Stokes-Rayleigh analogy in order to derive the internal work of a viscous membrane. We took into account the effect of weight and capillarity and derived their contribution to external work. We could then obtain the weak form of the equations for both the planar base state and the out-of-plane buckling problem.

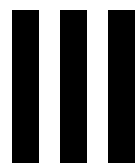
The present chapter was focused on the numerical implementation of these equations and on solving for the base state as well as for buckling modes. We first reviewed our choice of two-dimensional elements. A  $C^1$  element of the Bogner-Fox-Schmidt type, was chosen as it is well adapted for plate analysis. The base solution was obtained for different aspect ratios of the curtain, and it presents strong inhomogeneities with both extensional and compressive regions. For large aspect ratios  $\beta$ , the most compressive regions localize at the bottom edges. Compressive stresses appear as a consequence of flow lines moving closer to each other, which also deforms the curtain. We observed that this deformation is small and that the domain of study can be considered to remain a rectangle.

In the second step of the numerical analysis, because of the advective term, the partial differential equations are of order 5. This required us to use an idea found in discontinuous Galerkin methods and to introduce an additional variable with  $C^1$  elements. This additional constraint equation is added to the weak form and we can solve the generalized eigenvalue problem to obtain buckled solutions. We could find the instability threshold as a function of the aspect ratio and obtained a phase diagram for the stability of the falling viscous curtain. We finally restored capillary effects and observed qualitatively similar results.

This numerical toolbox has proven very powerful and could solve both the steady planar flow and the buckled configuration for all aspect ratios. However, this global stability analysis only lets us predict the threshold of the instability, and we don't have any information about how parameters contribute to the dynamics of the instability, neither can we predict anything about the post-buckling behaviour. We also noticed the peculiar appearance of a wavelength in the buckled solutions, that do not become unstable through the fundamental mode. We would like to get a better understanding of this effect by using an analytical study. We will not gain any insight about the nonlinear behaviour of the sheet in the post-buckling regime, however we expect to acquire a better understanding of the onset of the instability, and of the destabilization process. In part III, we will adapt a framework used in fluid mechanics to study open flows destabilizing under the effect of shear stresses to the falling viscous curtain. The latter is unstable under the effect of compressive stresses, and we will need to adapt the framework to our set of equations.







# **Open flow instabilities**



# Open flows and their stability

IN THE domain of fluid dynamics, the complete Navier Stokes equation cannot be solved in closed form in three dimensions, and in general, simpler equations retaining only essential elements and phenomena of a problem are studied. This idea of simplifying problems using only essential effects is very common in physics, but even more important in fluid dynamics. Common limits include the study of very viscous flows, where inertial terms can be neglected, or on the contrary turbulent flows.

The great variety of driving forces that can lead to fluid movement means that many different regimes can be studied that imply a pair or more of those effects. This is easily illustrated by the variety of non dimensional numbers defined in fluid dynamics, each comparing a few of the possible driving forces. The most usual physical quantities used in fluid dynamics are inertia and gravity's effects, viscosity, capillarity, along with the parameters that can have an effect on these like temperature, velocity, magnetic fields etc... This wide landscape is furthermore enriched by the existence of instabilities and transitional regimes.

The simplest examples of instabilities can be created from completely static configurations, with flows appearing as a result of the instability. Using inertia and gravity's effect, one can create an unstable stratification, with heavier fluid laying on a lighter fluid. Due to buoyancy the lighter fluid will move up through the heavier fluid leading to a phenomenon known as Rayleigh-Taylor's instability. This instability can be reproduced using a single fluid by heating the bottom of the fluid. Under the effect of temperature, the fluid will expand and its density will be reduced. This situation cannot be sustained and the fluid at the bottom will flow upwards. This phenomenon is known as the Rayleigh-Bénard instability and leads to stable recirculation cells and a stationary flow if heating is maintained. An unstable static fluid configuration can be created by using gradients of surface tension. Movement is created by the difference in surface energies and this is known as the Marangoni effect. An unstable configuration can be induced thermally. Geometry plays an important role in those instabilities. Another destabilization mode for fluids can be obtained by vibrating a still bath of fluid in the vertical direction. If the vertical acceleration is strong enough compared to gravity's acceleration  $g$ , a phenomenon known as Faraday's instability can be triggered, that leads to a periodic patterning of the surface of the bath. This phenomenon has several very interesting properties [CGM<sup>+</sup>05, CFGB05, PBC06].

Instabilities can also arise in stationary flows, with different effects depending on whether the flow has a free surface or not. A vertically falling column of liquid, e.g. water flowing out of a tap, can see its geometry modified by the so called Rayleigh Plateau instability. Capillarity tends to reduce the width of the liquid column, and can be strong enough to lead to the formation of droplets that have a lower surface energy in total. When surfaces are enclosed by walls or in a pipe, instabilities often lead to complex flow. In the case of a liquid flow impacting a bluff body like a transverse cylinder, a sphere, or any geometrical profile, at high velocities streamlines become non parallel and turbulent. The appearance of a Von Kármán vortex street can often be observed. The flow in a long pipe is stationary (laminar) at low Reynolds numbers, and experiences

a transition to turbulence when the Reynolds number becomes large. Shear-induced flows in general display instabilities, when velocity gradients cannot be sustained and lead to mixing. The Taylor-Couette flow is unstable through a centrifugal instability, that leads to the appearance of rolls in the vertical direction, while the stationary flow was originally purely orthoradial. The Kelvin-Helmholtz instability appears when two fluids moving at different velocities are in contact along a common boundary. It leads to mixing of the two fluids.

Many more instabilities exist, for example in the domain of magneto hydro dynamics where magnetic fields are coupled with the flow of molten metals, or surface instabilities like the Kapitza instability in falling films. This variety explains why the fluid mechanics community has developed tools to study flow stability. In our study of the falling viscous curtain, we are interested in the buckling instability of an open flow, which is a specific feature of liquid flows. This is why we turn to the methods developed in the domain of fluid dynamics to obtain a better analytical understanding of our problem.

Understanding underlying mechanisms and predicting the threshold of turbulence are obviously very interesting research matters, and in the case of open shear flows a framework was developed by the fluid dynamics community [MH82, HM85, BB97]. An open flow has particles entering and exiting the domain of study, material elements are advected and end up exiting the system. Shear flows display velocity gradients in their transverse direction that can lead to unstable configurations.

The study of instabilities in fluids has long been a subject of interest, but its application to open shear flows was inspired by works in the field of plasma physics [Bri64, Ber75]. The method and its application to open shear flows were exposed by Huerre and Monkewitz in 1985 [HM85]. In particular, they obtained the threshold of instability for a family of free shear layers with hyperbolic tangent velocity profiles.

Being able to study the dispersion relation that emerges from a problem's equations and to identify easily the threshold of the instability are essential steps. In an article by Kupfer et al. [KBR87] a method is exposed that simplifies the analysis of the dispersion relation associated with the problem under study. Dispersion relations  $\omega(k)$  are generally polynomial, but the inverse relation  $k(\omega)$  can be transcendental. The possibility of obtaining the values of parameters that lead to an instability without mapping from the  $\omega$  plane to the  $k$  plane is a strong advantage.

Reviews of the method covering theoretical advances [Cho05] and including numerical considerations [The11] are available. The framework for studying open shear flows is applied in many different physical situations, the most common example being the study of the flow past a bluff body. From the simply defined problem of the wake behind a cylinder to more complicated configurations with dynamic objects the prediction of instability thresholds and of the resulting oscillation frequency can be obtained with this method. Monkewitz et al. in 1987 [MN87] give a first detailed view of the method and of its application to the absolute instability in the near wake of bluff bodies. This paper is accompanied by experiments on shear flows behind variously shaped bodies. Confirmation of these experiments with further investigation of the convectively unstable regime are presented in an article by Khor et al. in 1995 [KSHW95]. The classical problem of the wake behind a cylinder has been extensively studied, with predictions for the frequency selection in the cylinder wake [Pie02]. The important interest in this problem stems in the fact that it only depends on one dimensionless number, the Reynolds number. A slightly modified version of this problem featuring an oscillating cylinder as been studied experimentally by Thiria et al. in 2007 [TW07]. In this experiment, the oscillation of

the cylinder can be tweaked in frequency and amplitude, authors observe the appearance of locked and non-locked states. In non-locked states (small amplitude/large frequency) the natural shedding frequency reappears at a further station downstream, while in a locked state (high amplitude/low frequency) the forced oscillation's frequency appears everywhere downstream in the wake. A recurring question that arises in the stability analysis is which base flow to consider. Authors including the two last cited contributions [Pie02, TW07, LTH10] have concluded that using a time-average of the flow as the base flow leads to the most accurate results for the linear stability analysis. This matter is extensively reviewed in [Bar06]. It is very interesting to notice that steady base flows do a poor job at predicting the nonlinear vortex shedding frequency when used in the stability analysis. Much better results can be obtained by using a time-average of the unsteady flow as the base state of the analysis. This all seems very reasonable, but obtaining these perturbed solutions to compute their time-average requires a nonlinear simulation which already gives the full evolution of the flow, including the vortices and their shedding frequency. This makes the method less predictive.

In a more general approach, the work by Thompson [THRS06] reviews the wake created by different types of bluff bodies. From 2D bodies like plates and modified cylinders to axisymmetric objects like a sphere or a torus, he compares in particular the obtained wake with the case of the standard circular cylinder wake. Assuming a slowly developing flow along the streamwise coordinate, Pier et al. [PH01] investigate the nonlinear self-sustained structures in prescribed synthetic wake flows. This nonlinear study is a bit more advanced and gives insight on frequency selection and the importance of non linear effects.

In all the previous examples of unstable open shear flows, the liquid flows in a medium considered wide in the transverse direction. In that case, unstable configurations lead to a complex flow. However, one can wonder what happens when the flow takes place in a deformable medium like an elastic pipe. This fluid-structure interaction due to flows in elastic media has also been studied using the open shear flow instabilities framework. Results are quite naturally more complicated, with a strong influence of the length of the medium and of its applied boundary conditions. In an article by Doaré et al. [DdL02a], authors consider a fluid conveying pipe on an elastic foundation. Equations of motion are of higher order than the usual amplitude equations of fluid mechanics which leads to the appearance of neutral zones. This result differs strongly with the usual analysis and leads to different regimes in which finite length effects must be taken into account. In a similar problem but this time considering hanging pipes, the length of the pipe is also a very important parameter. Doaré et al. [DdL02b] obtain two different regimes, and the velocity required to cause fluttering of the pipe is found to be independent of the length for longer pipes. In that case, the upper part of the pipe plays a negligible role and fluttering is located in a fixed size zone at the bottom of the hanging pipe.

A series of problems close to the case we study are fluid flows along a plane. The flow on an inclined plane is subject to different types of instabilities, of capillary or inertial origins. Although the geometry of these problems is a curtain of liquid, the contact with a plane changes a lot the type of instabilities observed. In particular Kapitza instabilities are the most interesting in this configuration.[RQ12, RQK12, DRQKGD07]

The closest problem in terms of geometry would be a fluid falling along a vertical plane. In a publication by Albert et al. [ATB14] authors find that the primary instability is convective. They apply a global stability analysis to their steady flow and end up using selected synthetic perturbations for the film and observing their evolution through direct

numerical simulations.

As mentioned earlier we are interested in the buckling instability of an open flow. The falling viscous curtain buckles under the effect of compressive stress. This mechanical instability that leads to a deformation of the free surface of the flow is unusual in fluid mechanics, however stability analysis of open flows was developed to study instabilities driven by shear stress. We will thus need to adapt the methods used in the study of open shear flows instabilities and apply them to the transverse balance governing out-of-plane movements of the curtain. In the next chapter, we will present the framework of open shear flow instability, and its application to the linear complex Ginzburg-Landau equation. This equation is chosen because it features all the physical ingredients typically encountered in a fluid mechanics problem (see §5.2). After reviewing the different steps of the method and describing how it can be used to predict the destabilization of an open shear flow, we will apply it in chapter 6 to the base solutions obtained in §4.1.2. In order to lead a completely analytical derivation of the open flow stability analysis, we will first have to study an averaged base flow. We will then restore the two-dimensional aspect of the base flow and resort to a numerical method to conduct the analysis.

## Contents

<b>5.1 Method introduction</b>	<b>77</b>
5.1.1 Geometry and definitions	77
5.1.2 Noise amplifiers and flow oscillators	78
5.1.3 Convective and absolute instabilities	78
5.1.4 Stream functions and dispersion relation	79
<b>5.2 The linear complex Ginzburg-Landau equation</b>	<b>80</b>
5.2.1 Temporal framework	81
5.2.2 Spatial framework	82
5.2.3 Space time analysis	84
5.2.4 Method summary	85
<b>5.3 Local to global step</b>	<b>88</b>
5.3.1 Complex analytical continuation	89

# Open shear flows instabilities

THIS CHAPTER intends to serve as an introduction to the framework for studying the stability of open shear flows. A reader unfamiliar with the approach will be able to follow its detailed application to the case of the linear complex Ginzburg-Landau equation. We will detail each step of the process and underline the differences, that are due to the open nature of the flow, with other methods for linear stability analysis. We are interested in this technique because we intend to transpose it to the buckling instability of the falling viscous curtain in open flow. We expect this analytical method to lead to a necessary condition and help us gather insight about the instability. The presentation of the following chapter is based on the section about open shear flows written by P. Huerre in the book Perspectives in Fluid Dynamics [Hue00], in which the interested reader can find additional details.

## 5.1 Method introduction

### 5.1.1 Geometry and definitions

In this introduction to the framework of open shear flows instabilities, we will be studying flows that all display similar geometries. At the inlet of an open flow sits the injection layer, where fluid is steadily entering the system at a prescribed velocity. This velocity will be denoted as  $U$ , the injection velocity. Along the flow is defined the coordinate  $x$ , with  $x$  oriented in the downstream direction.  $y$  is aligned with the cross-section of the



flow, and in general the typical length of the flow along this direction is much shorter than along the streamwise direction. At the end of the open flow, material elements are considered to be evacuated from the system. This outlet can be considered to sit at  $x = \infty$  or be at a finite distance.

### 5.1.2 Noise amplifiers and flow oscillators

The study of open shear flows will rely on the fundamental idea that two very different flow dynamics can be encountered. On the one hand, noise amplifiers, that display instabilities when extrinsic dynamics lead to some perturbations, which then get amplified in the system. On the other hand, flow oscillators that display an intrinsic dynamic triggered by external perturbations leading to a growing instability.

We discussed in the introduction the archetypal problem of the wake behind a bluff body. When studying the wake behind a two-dimensional cylinder in an infinite pipe, the problem only has one control parameter, the Reynolds number  $Re$ . In this problem, as the Reynolds number grows, i.e. as the injection velocity  $U$  is increased, the structure of the flow changes. It is the differences of velocities along the transverse direction  $y$  in the wake of the cylinder or in other words, the presence of shear, that is responsible for the instability. For low Reynolds numbers, the flow remains stable and laminar, with symmetric streamlines enveloping the cylinder. When the Reynolds number grows, a recirculation bubble appears behind the cylindrical obstacle, it is associated with a separation of the boundary layer at the back of the obstacle. In this intermediate regime, the flow behaves as a noise amplifier, with oscillations easily triggered by a perturbation of the inflow. In the last regime, associated with large Reynolds numbers, the Von Kármán vortex street fully develops through the intrinsic dynamics of the flow. This regime corresponds to a flow oscillator.

### 5.1.3 Convective and absolute instabilities

In accordance with the previously described observations, one can define two types of unstable regimes. These two regimes will be called convective and absolute instabilities.

In a convectively unstable zone, the flow behaves as a noise amplifier with no intrinsic wavelength or frequency completely outgrowing others. Perturbations in this type of flow are amplified but will move downstream as they are being advected away by the incoming flow.

In an absolutely unstable system, external perturbations are amplified and the intrinsic dynamics dominate, selecting a perturbation with prescribed frequency and wavelength.

A good way of understanding this phenomenon and its origin is by recalling that the flows under study are open. This means that a permanent inflow takes place, and that all material elements are being advected. Hence an instability that grows in amplitude with time is advected downstream and cannot remain in place. It will end up being evacuated from the system. The difference between a convectively and an absolutely unstable configuration is whether the instabilities are able to crawl back upstream fast enough, and thus appear to remain stationary in the laboratory frame. In this frame of reference, the condition for the appearance of an absolute instability is a zero group velocity for the unstable waves. We will see that this condition leads to a mathematical criterion for absolute instability.

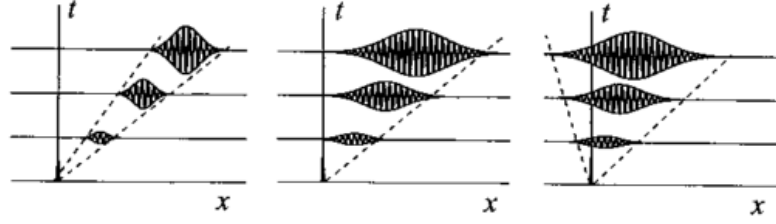


Figure 5.1: Left: Convectively unstable regime, a wave packet of the instability is advected away with time. Centre: Marginally unstable regime, the tail of the instability stays at a fixed position in space. Right: Absolutely unstable regime, the instability can fully develop in a fixed spot and propagates in the medium. Image reproduced from the figure 8 of reference [Hue00].

While studying open shear flows, an important assumption about the dynamics is made. The development of the basic flow along the streamwise direction is considered very slow. A fundamental first step in the analysis is to consider a perfectly parallel infinite flow in the streamwise direction. This is done by extracting the base flow  $U(x_0, y)$  at a given station  $x = x_0$  and extending it to infinity in both the upstream and downstream directions. This process can be reproduced at any particular coordinate  $x$  and will lead to the identification of different types of instabilities as a function of the coordinate  $x$ .

#### 5.1.4 Stream functions and dispersion relation

When studying the two dimensional flow of an incompressible viscous fluid, a stream function can be defined and used to recover the horizontal and vertical components of the velocity perturbations  $u$  and  $v$  to the base flow  $U(x_0, y)$ . The stream function contains two components, one accounting for the base flow, and the other corresponds to the perturbed solution:  $\psi(x, y, t)$ . This stream function perturbation is related to the velocity perturbations by:

$$u(x, y, t) = \frac{\partial \psi}{\partial y} \quad (5.1)$$

$$v(x, y, t) = -\frac{\partial \psi}{\partial x} \quad (5.2)$$

We recall that the dynamics of the system emerges from its response to external perturbations, and since the base flow is invariant in time and along the streamwise direction  $x$ , a natural choice for the mathematical form of the perturbation is  $\psi(x, y, t) = \Phi(y) e^{i(kx - \omega t)}$ .  $k$  is a complex wavenumber and  $\omega$  is the complex frequency. By substituting in the equation for the stream function and enforcing proper boundary conditions on the function  $\Phi(y)$ , the problem reduces to an equation relating  $k$  with  $\omega$  and depending on all the control parameters.

This equation is known as the dispersion relation and is denoted by  $D(k, \omega; R)$  where  $R$  represents the set of control parameters. In the case of the wake behind a bluff body in an infinite pipe discussed earlier, this set  $R$  is composed of only one parameter, the Reynolds number  $Re$ . Note that the values taken by the parameters forming the set  $R$  depend on the spatial position chosen  $x_0$ .

The dispersion relation can be solved by choosing a value for the complex wavenumber  $k$  and obtaining eigenvalues  $\omega$ . To each pair  $(k, \omega)$  corresponds an eigenfunction  $\Phi(y)$  that represents the shape of the perturbed stream function.

In this paragraph, we outlined this analysis to a two dimensional viscous flow without stating any equation. In the following we shall concentrate on the archetypal model for open shear flows: the linear complex Ginzburg-Landau equation.

## 5.2 The linear complex Ginzburg-Landau equation

In the previous section, without going into details of the process, we have seen that studying an infinite flow in the streamwise direction  $x$  requires to insert a particular form for perturbations. This mathematical substitution into the equations for the stream function leads to a dispersion relation.

In this section, we will detail the rest of the open shear flow analysis framework by applying it to a stream function obeying the linear complex Ginzburg-Landau equation (LCGL). We use this equation as a model for real flows because it displays all the ingredients that can be encountered in a fluid dynamics problem. In terms of the perturbed stream function  $\psi$  the LCGL is:

$$\left( \frac{\partial}{\partial t} + U \frac{\partial}{\partial x} \right) \psi - \mu \psi - (1 + i c_d) \frac{\partial^2 \psi}{\partial x^2} = 0 \quad (5.3)$$

The effects of advection appear with the comoving derivative, and  $U$  is the advection velocity along direction  $x$ .  $c_d$  is called the dispersion factor, it will have an influence on the phase velocity as a dispersive term.  $\mu$  is a parameter that drives the instability. The Ginzburg-Landau equation is usually defined as an amplitude equation, while the term  $-\mu \psi$  is the first order linearization of all possible unstable terms.

In order to obtain the dispersion relation corresponding to this equation, we insert the normal-mode decomposition  $\psi(x, t) = A e^{i k x - \omega t}$  in equation (5.3):

$$-i \omega + i k U - \mu + k^2 (1 + i c_d) = 0 \quad (5.4)$$

In this equation, the transverse dependence is completely projected out. Since no derivatives along the direction  $y$  are present, choosing an amplitude  $A$  or an arbitrary function  $\Phi(y)$  leads to the same result, as both would disappear in the derivation of this equation. Effectively, the direction  $y$  plays no role in this model.

We obtain the dispersion relation  $D(k, \omega; U, \mu, c_d)$ :

$$\omega = k U + i (\mu - k^2) + c_d k^2 \quad (5.5)$$

The dispersion relation is complex and of second order in the wavenumber  $k$ , the latter originating from the fact that the LCGL displays derivatives of order 2 at most. Dispersion relations of linear equations are always polynomial in  $k$ , and the function  $\omega(k)$  is easy to compute with a given set of parameters. However, the inverse function  $k(\omega)$  can be hard to compute in the case of high order polynomials. Here we have a second order equation to solve.

The values of the set of parameters  $R = (U, \mu, c_d)$  comes in part from the definition of the problem, and for the other part from the solution for the base flow. We study a one dimensional problem extracted from each slice of the base flow, with  $x$  taken in the

range  $[-1; 0]$ . As we change the value of  $x$ , we change the values of the set of parameters to  $R(x)$ , which can lead to different situations. Once the slice has been chosen and the set of parameters extracted, we extend the flow to infinity and obtain the corresponding dispersion relation. It is then possible to use the open shear flow instability framework. We will thus determine stable and unstable zones, along with their convective or absolute nature.

### 5.2.1 Temporal framework

The temporal framework helps understanding what is designated as initial values problems. It corresponds to the temporal evolution of an initial sinusoidal perturbation of wavenumber  $k$  of the whole system. In this study,  $k$  is a real number while the associated frequency  $w(k)$  is a complex number.

#### Growth rate

In this linear temporal stability analysis, unstable modes are associated with an unbounded amplitude at large time.  $\psi$  is proportional to  $e^{-i\omega t}$ , hence instabilities correspond to positive growth rates  $\text{Im}(\omega) = \text{Im}(\omega_r + i\omega_i)$  such that  $e^{\omega_i t}$  is a growing function of time.

For the Ginzburg-Landau equation, we can obtain the growth rate from the stability analysis  $\omega_i = \mu - k^2$ . Hence we have a positive imaginary part for  $\omega$  if and only if  $-\sqrt{\mu} < k < \sqrt{\mu}$ . This equation is only valid for positive values of  $\mu$ . Here we can confirm that  $\mu$  is the parameter governing stability, as wavenumbers  $k$  that lead to a positive growth rate can only be found if  $\mu > 0$ .

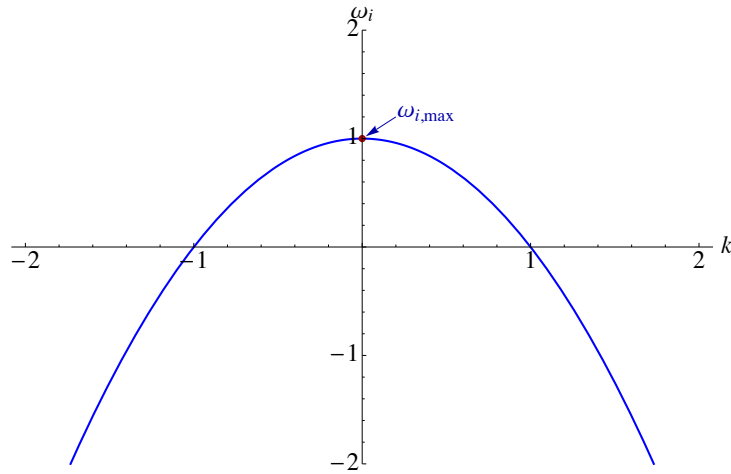


Figure 5.2: The value of the growth rate  $\omega_i$  as a function of  $k$  in the temporal analysis. Values chosen for the parameters are  $\mu = 1$ .

On figure 5.2 we can see the segment of values of  $k$  that lead to a positive growth rate, associated with an unstable mode. The flow is said to be linearly unstable for corresponding values of  $k$ . We notice that the most unstable mode is associated to the highest value of  $\omega_i$ , which corresponds to a wavenumber  $k = 0$  in this example. This indicates that the system is most unstable to very long wavelengths, and from this result

we should expect translation movements. Any characteristic length ignored in the local stability analysis could also be selected.

### Phase velocity

The phase velocity is defined as the ratio  $v_\phi = \frac{\omega_r}{k}$ . We can easily obtain the value of this velocity as a function of the parameters:

$$v_\phi = \frac{\omega_r}{k} = U + c_d k$$

The phase velocity is affine in  $k$ .

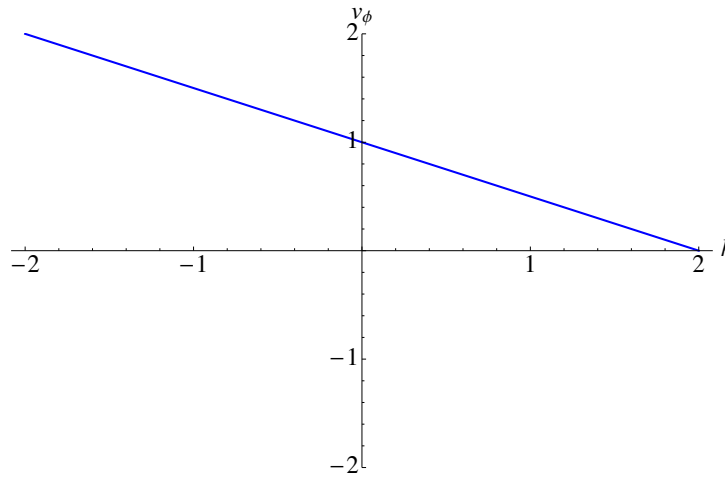


Figure 5.3: The value of the phase velocity  $v_\phi = \frac{\omega_r}{k}$  as a function of  $k$  in the temporal analysis. Values chosen for the parameters are  $U = 1$ ,  $c_d = -0.5$ .

Considering the case of a negative dispersion coefficient leads to smaller velocities for larger wavenumbers. According to the temporal stability of the previous paragraph, the most unstable wavenumber is  $k = 0$ , with a phase velocity  $v_\phi = U$ . This indicates that in the frame of the laboratory, phase moves along with the surrounding fluid.

We can conclude from this temporal study, that when an initial sinusoidal perturbation is applied to the system, translational modes have the larger growth rate and will propagate downstream as they are advected. We can also easily understand that this dynamics is not enough to give rise to a global instability that grows in the frame of the laboratory, as the fluid input will quickly replace the initial perturbation with an unperturbed state made up of new particles.

### 5.2.2 Spatial framework

The spatial framework helps understanding what happens in a so-called signalling problem. It corresponds to the spatial evolution in the streamwise direction of a time-periodic sinusoidal perturbation of frequency  $\omega$  located at a fixed station. In this framework,  $\omega$  is a real number while  $k$  is complex.

### Growth rate

In the spatial framework one can also define a (spatial) growth rate, and an unstable eigenmode corresponds to a streamwise growing amplitude. The growth rate is thus  $-\text{Im}(k) = -\text{Im}(k_r + i k_i) = -k_i$ . It is important to note that since the dispersion relation is of order 2, we will find two roots to the equation  $k(\omega)$ , that will be denoted by  $k^I$  and  $k^{II}$ . They are the two solutions of the polynomial  $(c_d - i)k^2 + kU + i\mu - \omega = 0$ . We find:

$$k^{I,II}(\omega) = \frac{-U \pm \sqrt{U^2 - 4(c_d - i)(i\mu - \omega)}}{2(c_d - i)}$$

We can plot the spatial growth rate  $-k_i^{I,II}$  as a function of omega:

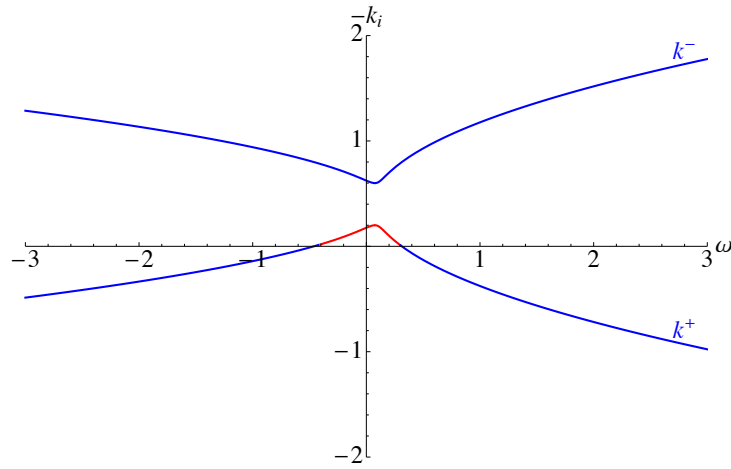


Figure 5.4: The value of the spatial growth rate  $-k_i$  for the two branches  $k^\pm$  as a function of  $\omega$  in the spatial analysis.  $k^-$  is not associated with causal solutions and has no physical meaning. Positive values of the spatial growth rate for the physical branch  $k^+$  are plotted in red. Values chosen for the parameters are  $U = 1$ ,  $\mu = 0.15$ ,  $c_d = -0.5$ .

The jump in the middle of this curve appears because  $k^I$  and  $k^{II}$  exchange roles, one always increasing while the other is decreasing. The two very distinct branches that appear can be labelled through causality arguments. Without delving in the details, these branches have different physical meanings and will be denoted with  $k^+$  and  $k^-$ . The branch  $k^-$  corresponds to waves propagating upstream of the source located at  $x = 0$ . This of course does not bear much physical meaning. However the  $k^+$  branch corresponds to waves propagating in the physical domain  $x > 0$ . If the spatial growth rate  $-k_i^+$  is positive for the physical branch, we have found waves that will propagate. Values of  $\omega$  that lead to positive growth rates  $-k_i^+$  can be found as soon as  $\mu > 0$ , see the red part of the branch  $k^+$  in figure 5.4.

The signalling problem corresponds to the behaviour of a noise amplifier, sinusoidal excitations at a fixed station being propagated downstream. This corresponds to the regime of convective instability. Incidentally, in the absolutely unstable regime, this problem is not well-posed and we cannot study the intrinsic dynamics in the spatial framework. In the next section we will see how to overcome this limitation by using a more general analysis.

### 5.2.3 Space time analysis

As we have previously exposed, both temporal and spatial frameworks are insufficient to predict the growth of an absolutely unstable eigenmode. We have seen that a fundamental aspect of an absolute instability is that it is able to resist the effect of advection, and that the unstable mode can invade the whole domain. This requires the mode to be able to remain at a fixed position in the laboratory frame. This condition can be easily expressed as the group velocity being 0. Another point of view would be to consider the wave as moving upstream against the flow, with a velocity exactly opposite to the advective term. To overcome the limitations of the temporal and spatial frameworks, we have to use a spatiotemporal analysis.

In the spatiotemporal framework, both  $\omega$  and  $k$  are now complex numbers, and the dispersion relation is a mapping from the complex  $k$ -plane to the complex  $\omega$ -plane. By studying the properties of this holomorphic function with complex analysis methods, we will obtain criteria to identify different regimes.

#### Saddle point condition

Without going into too many details, that are available in reference [Hue00], the main result we shall recall is the condition:

$$\frac{\partial \omega}{\partial k}(k^*) = \frac{x}{t}$$

This equation originates from a stationary phase condition, that leads to the identification of a saddle-point at a complex value  $k^*$ . It is a complex condition, while the ratio  $\frac{x}{t}$  is a real number, corresponding to a velocity ( $\frac{x}{t} = V$  defines a ray in the  $(x, t)$ -plane, following this ray is a movement with velocity  $V$ ). Hence the complex ratio  $\frac{\partial \omega}{\partial k}$  has a physical meaning only when it takes real values, being then interpreted as the group velocity.

In the temporal study, we have already identified linearly stable and unstable zones. We recall that the most unstable mode corresponded to the maximum of the curve  $\omega_i(k^t)$ , where  $k^t$  designates the real parameter  $k$  used in the temporal analysis, and wonder what its associated group velocity is. We expect it to be positive, and the associated instability to be of convective nature. The associated wavenumber  $k_{max}^t$  obeys the criterion  $\frac{\partial \omega_i}{\partial k}(k_{max}^t) = 0$ , even with  $k$  complex. We can now compute the corresponding group velocity  $\frac{\partial \omega}{\partial k}(k_{max}^t) = \frac{\partial \omega_r}{\partial k}(k_{max}^t) + 0i = V_{max}$ , which is a real number. In the Ginzburg-Landau example,  $\frac{\partial \omega}{\partial k} = U - 2ik + c_d k$ , and we obtain the expected value at  $\frac{\partial \omega}{\partial k}|_{k_{max}^t=0} = V_{max} = U$ , proving that the most unstable mode predicted using the temporal framework is of convective nature, and is advected away by the surrounding fluid.

#### Zero group velocity condition

We know that an instability having a zero group velocity corresponds to an unstable mode that is able to remain at a fixed position in the frame of the laboratory. Following the definition of the group velocity, we want to find the complex wavenumber  $k_0$  that corresponds to a zero group velocity  $\frac{\partial \omega}{\partial k}(k_0) = 0$ . We are then interested in the associated growth rate  $\omega_i(k_0) = \omega_{0,i}$ . If this value is positive, we have an absolute instability, with a growing mode that is able to maintain itself at a fixed location, and to fully develop

into an instability. On the other hand, if  $\omega_{0,i}$  is negative, the associated instability is of convective nature.

Within a linearly unstable region ( $\omega_{i,max} > 0$ ), the sign of the absolute growth rate  $\omega_{0,i}$  is the criterion that discriminates between a convective instability (noise amplifier without intrinsic dynamics,  $\omega_{0,i} < 0$ ), and an absolute instability (flow oscillator with intrinsic dynamics,  $\omega_{0,i} > 0$ ).

### 5.2.4 Method summary

At each station  $x$  along the flow, we can now proceed in three steps.

1. Identify the parameters for the current station  $x$ . In the case of the LCGL, find the values of  $U$ ,  $\mu$ , and  $c_d$ .
2. Temporal analysis ( $k$  real,  $\omega$  complex): Obtain the sign of  $\omega_{i,max}$  to establish whether the corresponding infinite flow is linearly unstable.
3. Spatiotemporal analysis ( $k$  and  $\omega$  complex): If it is unstable, establish whether the instability is convective or absolute by:
  - (a) Finding the absolute wavenumber  $k_0$  that cancels the complex group velocity  $\frac{\partial \omega}{\partial k}(k_0) = 0$ .
  - (b) Determining the sign of the absolute growth rate  $\omega_{0,i}$

Out of these steps, the most difficult is 3)a. as it requires to find the roots of the complex derivative of a holomorphic function. As mentioned in the introduction of this chapter, dispersion relations are in general polynomials in  $k$ . In the case of the LCGL, this polynomial is of order 2, and the group velocity is a first order polynomial, it is thus easy to obtain the value  $k_0$  that cancels the group velocity. However, when higher order polynomials are involved, it can be a difficult task. This is why the work by Kupfer et al. [KBR87] mentioned in the introduction of this chapter is of importance, as it gives a way of finding the value  $k_0$  by only studying the complex mapping  $\omega(k)$ .

### Cusps in the complex map

In the complex  $\omega$ -plane, the condition  $\frac{\partial \omega}{\partial k}(k) = 0$  leads to an easily identifiable structure. The cancellation of the complex derivative means that both the real and imaginary parts of the function see their values changing slower, and reach some kind of plateau. This happens while varying the value of  $k$ , hence by following a path in the  $k$ -plane the trajectory of  $\omega(k)$  should do something characteristic in the  $\omega$ -plane. Moving along a path in the  $k$ -plane is visualized in the  $\omega$ -plane as the parametric plot  $(\omega_r(k), \omega_i(k))$ . A good way to feel what will happen is to imagine moving along a path in the  $k$ -plane at a constant velocity. Since both the real and the imaginary parts have a zero derivative at the same spot  $k_0$ , when approaching this value the curve in the  $\omega$ -plane will slow down, and reach a point where it stops for an instant, before accelerating again. This situation is typical in the study of parametrized curves, and only a few different scenarios are possible. One can witness a maximum, an inflexion point, or a cusp. In that case, we will want to observe the formation of a cusp, which is a very distinctive and easy to spot structure.



As an illustration of this phenomenon, here is an example from everyday life. Most people will be familiar with the cycloid, the curve formed by a fixed point on a rolling circle, e.g. the valve on the wheel of a bike moving forward. The path  $k$  is the road the bike is moving on. As it follows this straight line, the trajectory of the valve corresponds to the function  $\omega(k)$ . The vertical motion of the valve attached to the wheel corresponds to the vertical axis in the  $\omega$ -plane, hence to the function  $\omega_i(k)$ . In similar manner, the horizontal motion of the valve corresponds to  $\omega_r$ . The vertical motion is easily understood, it is a sine function, with zero velocity at the top and at the bottom of the wheel. When the valve reaches these two points, its vertical movement stops just for an instant. The horizontal motion is just a little bit more complicated, as it is the sum of a cosine function and of the translation of the bike. This movement has a zero velocity when the valve reaches the bottom of the wheel, as it touches the road. Every time the valve reaches the bottom of the wheel (when it touches the road), these two functions simultaneously have a zero velocity. The resulting curve is the cycloid, represented in figure 5.5. One can clearly see the appearance of cusps.

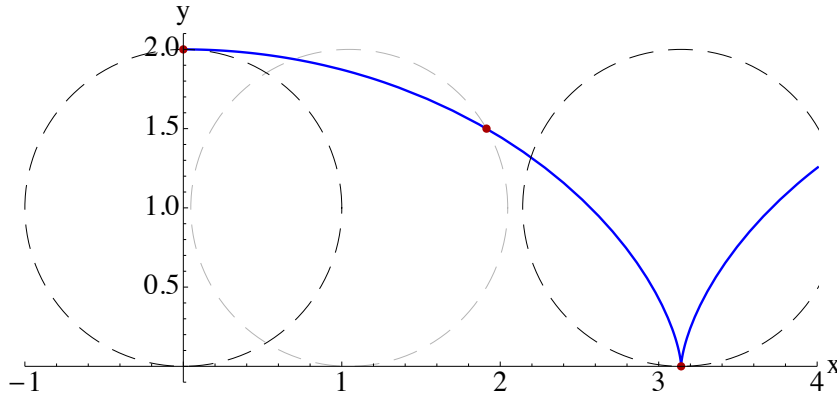
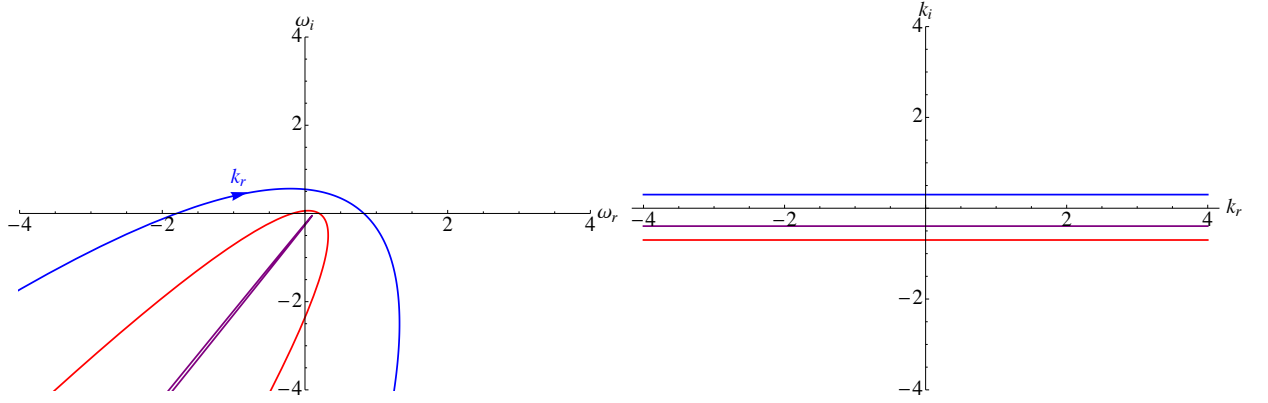


Figure 5.5: Trajectory of the valve on the wheel of a moving bike. The parametrization of this curve is  $t \rightarrow (t + \cos(t), \sin(t))$

We will choose to follow horizontal paths in the  $k$ -plane, which means the value of  $k_i$  is fixed while we vary  $k_r$  through all real values. We can now vary the value of  $k_i$  and see the path in the  $\omega$ -plane deforming into a cusp.



(a) Curves in the  $\omega$ -plane corresponding to the paths chosen. (b) Three different horizontal paths corresponding to different  $k_i$  values are followed.

Figure 5.6: Shape of the path in the complex  $\omega$ -plane as we follow a horizontal path in the  $k$ -plane. Blue path lies above  $k_0$  in the  $k$ -plane. Purple path crosses  $k_0$ , the corresponding trajectory forms a cusp in the  $\omega$ -plane. Red path lies below  $k_0$ .

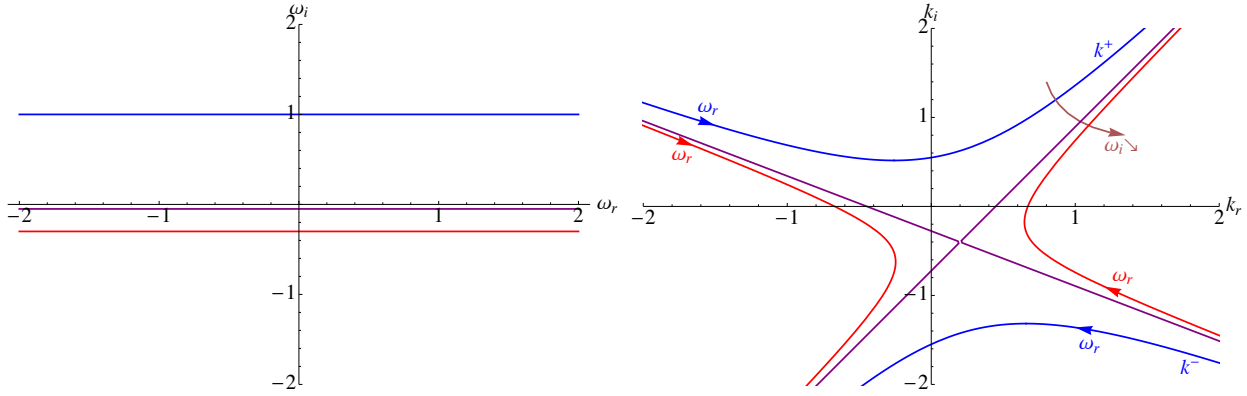
### Pinching in the $k$ -plane

By using this mapping from the  $k$ -plane to the  $\omega$ -plane we have access to the imaginary part of  $k_0$ . We actually don't even need to determine the real part of  $k_0$  as the value  $\omega_{0,i}$  is readily obtained at the extremity of the cusp in the  $\omega$ -plane. It is simply a matter of determining whether it lies above or underneath the horizontal axis to determine if the instability is convective or absolute for a given set of parameters.

However, the dispersion relation can be of higher order than one and present multiple cusps in the  $\omega$ -plane. This is why it is important to study the opposite transformation from the  $\omega$ -plane to the  $k$ -plane. Determining which cusp bears a physical meaning and corresponds to the saddle-point condition is a necessary step. We will follow horizontal paths in the  $\omega$ -plane, and watch the evolution of the branches in the  $k$ -plane. The number of branches is equal to the dispersion relation's polynomial order in  $k$ . First of all, when a horizontal path crosses the location of the cusp in the plane  $\omega$ , branches in the  $k$ -plane also show a specific behaviour. Every cusp corresponds to the pinching of two  $k$  branches. Secondly, we have already mentioned that branches in the  $k$ -plane can be associated with waves propagating either downstream in the physical domain  $x > 0$ ,  $k^+$  branch, or upstream in a virtual domain  $x < 0$ ,  $k^-$  branches. The pinching in the  $k$ -plane can thus happen between two branches of the same kind ( $++$  or  $--$ ), or between a  $k^+$  and a  $k^-$  branch. This last case only has a physical meaning.

Hence authors of Kupfer et al. [KBR87, BF83] devised a geometrical way of determining the location of  $k_0$ . Initially, a horizontal contour is chosen high in the  $\omega$ -plane. If the contour is sufficiently high, corresponding  $k$  branches will be located exclusively in the upper ( $k^+$  branches) or in the lower half ( $k^-$  branches) of the  $k$ -plane. Once these branches have been attributed their correct causality, one can lower the horizontal contour in the  $\omega$  plane until a pinching occurs. If this pinching involves two branches of the same causality, the corresponding cusp is nonphysical. By lowering further the contour, one will find a cusp that corresponds to the first pinching between  $k$  branches of opposite polarities. This unambiguous scheme can be applied to any dispersion relation and precisely localizes the absolute wavenumber  $k_0$ .

In the case of the Ginzburg-Landau equation, only one branch of each causality is present, and for that very reason, only one cusp can be found. The first pinching that happens is thus necessarily associated with the saddle-point and indicates the position of  $k_0$ .



(a) Three different horizontal paths corresponding to different  $\omega_i$  values are followed. (b) Curves in the  $k$ -plane corresponding to the paths chosen.

Figure 5.7: Pinching occurs around the absolute wavenumber  $k_0$  as we follow different contours in the  $\omega$ -plane. Blue path is high in the  $\omega$ -plane,  $k^+$  and  $k^-$  branches are easily identified. Purple path goes right through the cusp and crosses  $\omega_{0,i}$ . Red path lies below the cusp, branches in the  $k$ -plane have merged and  $k^+$  and  $k^-$  branches cannot be defined any more.

### 5.3 Local to global step

In a typical scenario, the base flow under study will see a variation of its parameters along the spatial coordinate  $x$ . The first slices will usually be of stable nature. As the flow becomes linearly unstable, it is generally convectively unstable, and further downstream may become absolutely unstable. These different zone are easily identified by tracking both  $\omega_{i,max}$  and  $\omega_{0,i}$  as functions of  $x$ , which requires to carry out the analysis described above repeatedly for different values of  $x$ .

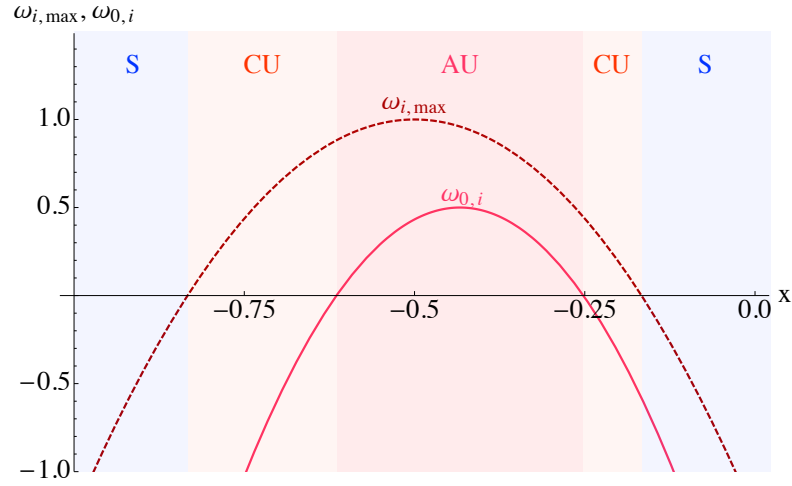


Figure 5.8: A very common situation in the stability of open shear flows. Along the streamwise direction  $x$ , the set of parameters  $R$  takes values that reveal stable and unstable regions, including a pocket of absolute instability. The dependence in  $x$  is chosen arbitrarily simple for the purpose of illustration. Stable zones of the flow,  $\omega_{i,max} < 0$ , are in blue (S). Unstable zones of the flow,  $\omega_{i,max} > 0$ , are in red (U). The unstable region is further separated in a convectively unstable region (CU) with  $\omega_{0,i} < 0$  and an absolutely unstable regions (AU) with  $\omega_{0,i} > 0$ .

This appearance of a positive absolute frequency is an indication of the unstable nature of the flow. However, different values are necessarily obtained for  $\omega_0$  as we move along the spatial coordinate  $x$ . Hence in order to predict the actual frequency of the instability that will appear in the complete system, we have to reconnect all slices, and go from a local to a global analysis.

### 5.3.1 Complex analytical continuation

In order to do so, one must consider the values obtained for  $\omega_0$  as a function of  $x$ . This complex function of a real variable must be analytically continued in order to become a complex map  $\omega_0(X)$ , where  $X$  is now a complex number extending the real axis  $x$ .

This process leads to a complex map with the specific feature of presenting a saddle point, generally not too far from the real  $x$  axis. This means that we can once again find a cusp, now in the complex  $X$  plane, that will be located at a value  $\omega_G$ . The imaginary and real parts of  $\omega_G$  are interpreted as the predicted growth rate  $\omega_{G,i}$  and frequency  $\omega_{G,r}$  of the global mode of instability, i.e. the mode that will appear in the complete system.

Reconstructing a complex function out of the relation  $\omega_0(x)$  is possible because we are considering holomorphic functions. Hence the Cauchy-Riemann equations hold,  $\frac{\partial \omega_{0,r}}{\partial X_r} = \frac{\partial \omega_{0,i}}{\partial X_i}$  and  $\frac{\partial \omega_{0,r}}{\partial X_i} = -\frac{\partial \omega_{0,i}}{\partial X_r}$ . Since we know both the real and imaginary parts along the real path  $X = X_r + 0 * i = x$ , we can approximate the derivatives and furthermore the values of the function in the complex plane. Numerically, a practical method for the analytical continuation of a function is to estimate both the real and imaginary parts of  $\omega_0(x)$  using Padé approximants, and then replacing  $x$  with a complex variable  $X$ . These

approximations are generally better when close to the real axis (small imaginary values for  $X$ ), and the method is thus only robust if the cusp we are searching for is indeed close to the real axis.

This method will be applied in the next chapter to a more complicated dispersion relation corresponding to the falling viscous curtain of part [II](#). It will be used to identify linearly unstable zones in the base flow, and further study whether they correspond to convective or absolute instabilities.

## Contents

<b>6.1</b>	<b>Local stability analysis of the averaged flow . .</b>	<b>92</b>
6.1.1	Slice averaging of the flow . . . . .	92
6.1.2	Width averaged equation of motion . . . . .	94
6.1.3	Stability analysis: temporal and spatial frame- works . . . . .	95
6.1.4	Stability analysis: spatiotemporal framework .	97
6.1.5	Phase diagram . . . . .	103
<b>6.2</b>	<b>Local stability analysis of the two-dimensional flow . . . . .</b>	<b>105</b>
6.2.1	Boundary value problem . . . . .	105
6.2.2	Stretched base flow and predicted global mode	106

# The falling viscous curtain as an unstable open flow

IN THIS chapter, we will revisit the falling viscous curtain problem, which was the main matter of part II, using the tools introduced in chapter 5. The major characteristic of our problem is that instabilities emerge from compressive stresses and lead to a deformation of the curtain, whereas in the case of the flow behind a bluff body for example, instabilities appear because of shear stresses, and lead to a complex flow. This difference doesn't impact how the method should be applied, only the structure of the equations must be expected to differ. We designate as an open compressive flow open flows for which instabilities are due to compressive stresses. We have seen in the previous chapter that the first step of the analysis requires the definition of a synthetic 1D flow infinite in the streamwise direction. In the case of the Ginzburg-Landau equation, the transverse direction  $y$  effectively played no role in the derivation of this one dimensional equation. However in the case of a two-dimensional base flow, the dependence in the transverse direction and the corresponding boundary conditions will have an importance. The values of the set of parameters  $R$  of the one dimensional problem are extracted from the slices of the base flow, and terms featuring a transverse dependence can be kept as is or averaged. The choice of boundary conditions and of the transverse dependence of the flow are thus essential steps that lead to different parameters for the resulting unidimensional flow.

As mentioned in the introduction of this part, the framework for open shear flows instabilities analysis has been applied to a wide range of problems in fluid mechanics, and the question of the choice of a base flow has been extensively discussed [Bar06]. In particular, when one disposes of experimental or numerical data that go beyond the base flow and gives a better understanding of the instability's development, it is wise to use it. In that line of ideas, when studying oscillating flows, the accuracy of frequency prediction using the method is greatly improved by considering the time-averaged of these oscillations as the base flow. We will keep in mind that the averaging done in the first part of the study is an essential step since it contains all the retained physical information.

The out-of-plane equilibrium for the falling viscous curtain features a set of parameters  $R$  with different spatial dependences. It depends implicitly on the aspect ratio  $\beta$  and of Jeffreys number  $Je$  through the values of the pre-stress state responsible for buckling. Parameters  $\frac{\varepsilon^2}{Je}$  and  $Ca^{-1}$  are constants, although capillary effects will be ignored in this chapter. The values of the stress tensor  $\bar{N}_{\alpha\beta}$  that appear in the equation depend on the spatial coordinates  $x$  and  $y$ . The streamwise dependence will be responsible for the dependence on the direction  $x$  of the set  $R$ , while the transverse dependence can be treated in two ways. In §6.1 we will average the base flow across its width, leading to constant values for the tensor  $\bar{N}_{\alpha\beta}$  at each slice. The resulting dispersion relation can be solved analytically as it is a polynomial. In §6.2 we use the method without averaging the base flow and retain the full transverse dependence of each slice. However, this will define a boundary value problem that can only be solved numerically.

## 6.1 Local stability analysis of the averaged flow

The falling viscous curtain's base solution is governed by two parameters, the aspect ratio  $\beta$  and Jeffreys number  $Je$  (we will ignore the effects of capillarity and set the inverse capillary number to zero in this chapter). These two parameters suffice to obtain the planar base solution. In order to study buckling of the curtain, we also take into account its thickness using the parameter  $\frac{\varepsilon^2}{Je}$ . The set of dimensionless parameters  $R$  is thus  $(\beta, Je, \frac{\varepsilon^2}{Je})$ , with the addition of the parameters responsible for buckling, the applied stresses. In this section, we choose to account for these stresses by taking their average value, wishing to simplify the one-dimensional system by eliminating its transverse dependence. We will compute the mean of the stress tensor  $\bar{N}_{\alpha\beta}$  along the transverse direction  $y$ . Note that averaging velocities, then computing stresses wouldn't lead to the same results. Here we want to retain the important physical parameters, which are the stresses.

### 6.1.1 Slice averaging of the flow

By considering symmetries of the stress tensor  $\bar{N}_{\alpha\beta}(x, y)$ , we see that the components  $\bar{N}_{xx}$  and  $\bar{N}_{yy}$  are symmetric with respect to the axis of symmetry  $y = 0$ , while  $\bar{N}_{xy}$  and  $\bar{N}_{yx}$  are antisymmetric. Hence the average of the off-diagonal components (shear components) of the stress tensor will cancel.

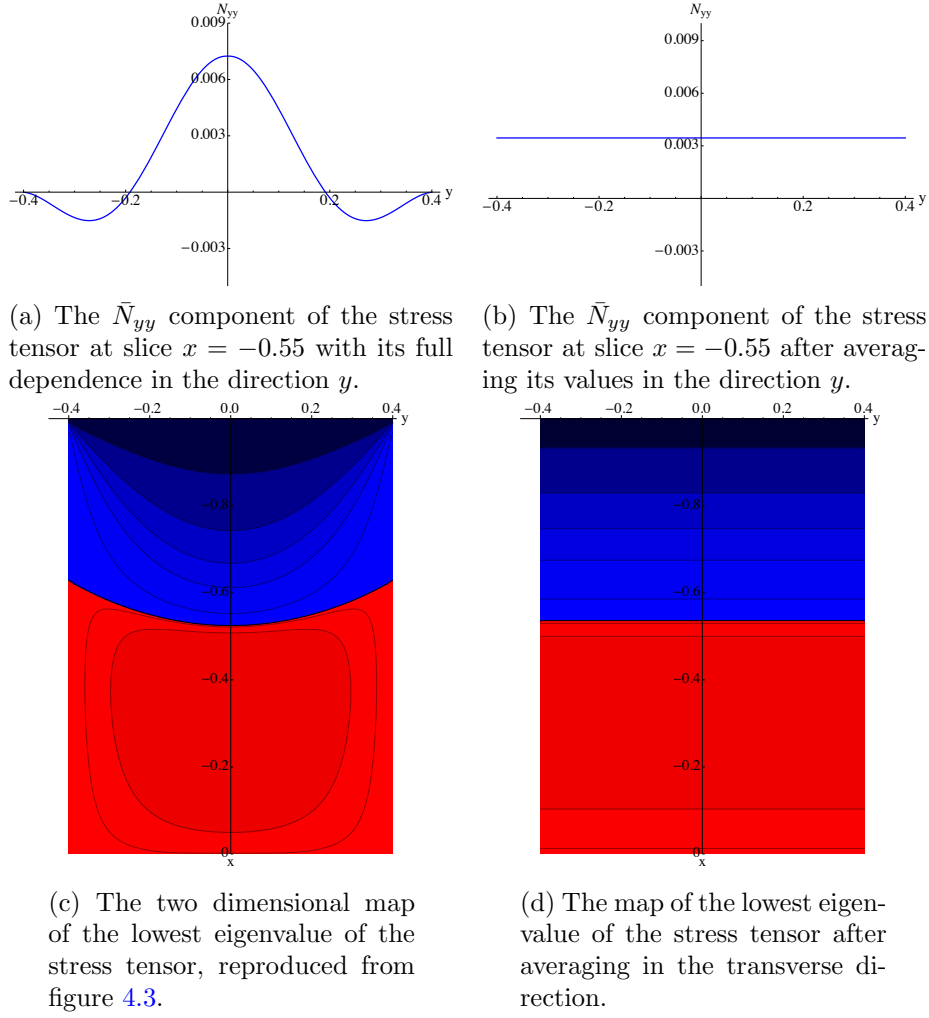


Figure 6.1: Averaging process for a curtain of aspect ratio  $\beta = 0.4$ .

This averaging process can be applied to all components of the stress tensor at each spatial station along the stream-wise direction  $x$ . We can represent the evolution of the averaged stresses along the flow.



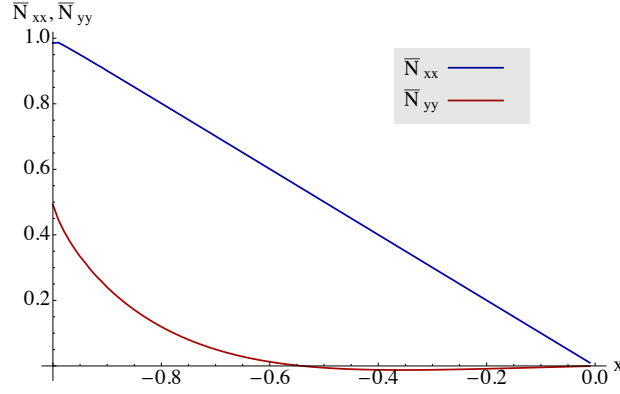


Figure 6.2: Averaged values of the stress tensor as a function of the spatial coordinate  $x$  for  $\beta = 0.4$ . Blue curve: value of the average longitudinal stress  $\bar{N}_{xx}$ , this stress is always tensile. Red curve: value of the average transverse stress  $\bar{N}_{yy}$ , the value of this stress becomes negative for a range of spatial stations, in which compressive stress destabilizes the base flow.

We expect compressive stresses in the transverse direction  $y$  to be responsible for buckling. Hence for the slices where  $\bar{N}_{yy} < 0$ , we can anticipate a linearly unstable flow.

### 6.1.2 Width averaged equation of motion

We are considering a one dimensional flow in the stream-wise direction, with parameters extracted from a slice of the base flow. The latter being averaged in the transverse direction, the associated spatial dependence is lost and the flow is also infinite in the  $y$  direction. We will restore the physical width of the flow by applying specific boundary conditions. We recall the strong form of the out of plane equilibrium (3.15c), ignoring capillary effects, and with averaged values for the stress tensor:

$$\begin{aligned}
 N_{\alpha\beta} H_{,\alpha\beta} - \varepsilon^2 M_{\alpha\beta,\alpha\beta} &= 0 \\
 \bar{N}_{xx} H_{,xx} + \bar{N}_{yy} H_{,yy} - \frac{\varepsilon^2}{\text{Je}} (H_{,\alpha\beta t} + U H_{,\alpha\beta x} + \delta_{\alpha\beta} (H_{,\gamma\gamma t} + U H_{,\gamma\gamma x}))_{,\alpha\beta} &= 0 \\
 \bar{N}_{xx} H_{,xx} + \bar{N}_{yy} H_{,yy} - \frac{\varepsilon^2}{\text{Je}} \left( \frac{\partial^2}{\partial x_{\alpha} x_{\beta}} \frac{DH}{Dt} + \delta_{\alpha\beta} \left( \frac{\partial^2}{\partial x_{\gamma} x_{\gamma}} \frac{DH}{Dt} \right) \right)_{,\alpha\beta} &= 0 \\
 \bar{N}_{xx} H_{,xx} + \bar{N}_{yy} H_{,yy} - \frac{\varepsilon^2}{\text{Je}} \left( 2 \frac{\partial^4}{\partial x^4} \frac{DH}{Dt} + 2 \frac{\partial^4}{\partial y^4} \frac{DH}{Dt} + 4 \frac{\partial^4}{\partial x^2 y^2} \frac{DH}{Dt} \right) &= 0 \\
 \bar{N}_{xx} H_{,xx} + \bar{N}_{yy} H_{,yy} - 2 \frac{\varepsilon^2}{\text{Je}} \left( \frac{\partial^2}{\partial x^2} + \frac{\partial^2}{\partial y^2} \right)^2 \frac{DH}{Dt} &= 0 \quad (6.1)
 \end{aligned}$$

We expressed this equation using operators applied on  $\frac{DH}{Dt} = H_{,t} + U H_{,x}$  such that  $\frac{\partial}{\partial x} \frac{DH}{Dt} = \left( \frac{DH}{Dt} \right)_{,x} = H_{,tx} + U H_{,xx}$ .

We have projected out the  $y$  structure of the base flow by averaging the stress tensor, hence as a first step we chose as the perturbed function  $H(x, y, t) = e^{iqy} \Psi(x, t)$ . The dependence in  $x$  and  $t$  remains arbitrary, but we take into account the averaged aspect of the flow by choosing a transverse wavenumber  $q$  that must be imposed by boundary

conditions. We could skip this step and immediately insert an arbitrary perturbation following the open shear flow framework, but it is important to note that  $q$  and the stream-wise wavenumber  $k$  play different roles.  $q$  corresponds to the eigenmode and is entirely determined by taking the lateral boundary conditions into account, while  $k$  can take complex values and is the variable entering in the dispersion relation  $\omega(k)$ . After inserting in (6.1) we obtain the equation:

$$2 \frac{\varepsilon^2}{\text{Je}} \left( q^2 - \frac{\partial}{\partial x^2} \right)^2 \frac{D\Psi}{Dt}(x, t) + \bar{N}_{yy} q^2 \Psi(x, t) - \bar{N}_{xx} \frac{\partial \Psi}{\partial x^2}(x, t) = 0 \quad (6.2)$$

The structure of equation (6.2) is remarkably close to the previously introduced linear complex Ginzburg Landau (LCGL) equation (5.3). Apart from the complicated operator featuring spatial derivatives that applies to the advective term, other terms have an obvious interpretation. The instability parameter  $\mu$  is the analogue of  $-\bar{N}_{yy}$ , illustrating that compressive stresses in the horizontal direction ( $\bar{N}_{yy} < 0$ ) are responsible for the buckling instability of the curtain. The diffusive parameter  $c_d$  is zero in our situation. The whole equation could be divided by  $\bar{N}_{xx}$  in order to recover the coefficient 1 for the rightmost term with  $c_d = 0$ . This indicates that the ratio of the transverse and longitudinal stresses is the actual instability parameter.

### Dispersion relation

In order to obtain the corresponding dispersion relation, we now specify the spatial and time dependence of the perturbed out of plane displacement by choosing an arbitrary perturbation  $H(x, y, t) = e^{iqy} A e^{i(kx - \omega t)}$ . By inserting this form into equation (6.2) we obtain the dispersion relation:

$$2 \frac{\varepsilon^2}{\text{Je}} (k^2 + q^2)^2 (i k U - i \omega) + \bar{N}_{yy} q^2 + \bar{N}_{xx} k^2 = 0$$

$$\omega = k U - i \frac{\text{Je}}{\varepsilon^2} \frac{(\bar{N}_{xx} k^2 + \bar{N}_{yy} q^2)}{2 (k^2 + q^2)^2} \quad (6.3)$$

The dispersion relation  $D(k, \omega; [\beta, U, \frac{\varepsilon^2}{\text{Je}}, \bar{N}_{xx}, \bar{N}_{yy}]) = D(k, \omega; R) = 0$  is a fifth order polynomial in  $k$ . This comes from the high order spatial derivatives in the equations of elasticity combined with the comoving derivative's advective part, as discussed in §4.2.1.

### 6.1.3 Stability analysis: temporal and spatial frameworks

Now that the dispersion relation for the averaged one dimensional flow has been obtained, we can apply the remaining steps of the stability analysis described in §5.2.4.

#### Temporal framework

We expect slices featuring compressive transverse stresses  $\bar{N}_{yy} < 0$  to be linearly unstable. With  $k$  real, the value of the imaginary part of  $\omega$  is  $\omega_i = -\frac{\text{Je}}{\varepsilon^2} \frac{(\bar{N}_{xx} k^2 + \bar{N}_{yy} q^2)}{2 (k^2 + q^2)^2}$ . We are looking for positive values for the temporal growth rate  $\omega_i$  which is equivalent to the

condition:

$$\begin{aligned}\bar{N}_{xx} k^2 + \bar{N}_{yy} q^2 &< 0 \\ k^2 &< \frac{-\bar{N}_{yy}}{\bar{N}_{xx}} q^2 \\ |k| &< \sqrt{\frac{-\bar{N}_{yy}}{\bar{N}_{xx}}} |q|\end{aligned}\tag{6.4}$$

Since  $\bar{N}_{xx}$  is a positive number for all slices, equation (6.4) has solutions as soon as  $\bar{N}_{yy}$  takes negative values. As anticipated earlier, slices subject to transverse compression are linearly unstable.

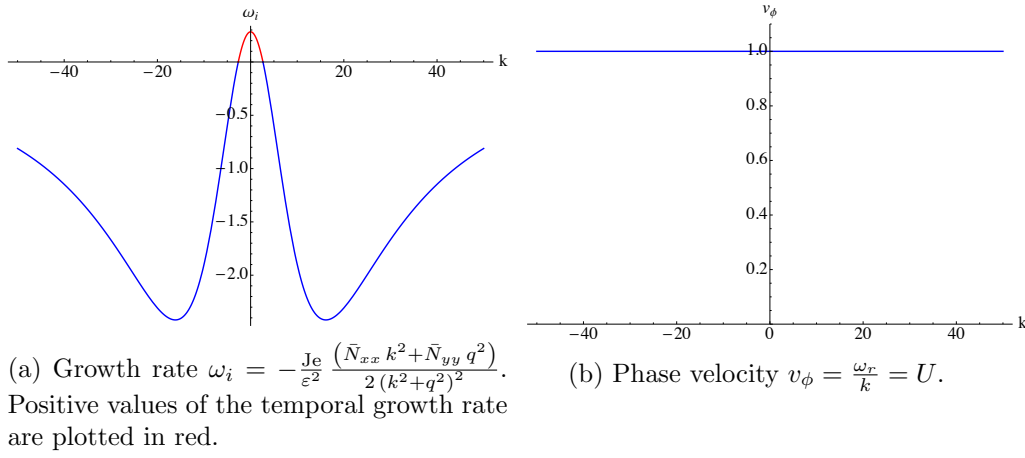


Figure 6.3: Temporal analysis of the falling viscous curtain, based on the pre-stress averaged in the transverse direction. Values chosen for the parameters are  $\beta = 0.4$ ,  $\frac{\varepsilon^2}{\text{Je}} = 10^{-4}$ ,  $q = \frac{2\pi}{\beta}$ . The slice chosen is under transverse compression,  $x = -0.45$ .

Similarly to the LCGL situation, the most unstable wavenumber is  $k = 0$ . In the absence of a diffusive term  $c_d$  in our equation, the phase velocity  $v_\phi = \frac{\omega_r}{k}$  as a function of  $k$  is a constant  $v_\phi = U$ .

### Spatial framework

In the spatial stability analysis, we consider complex values for  $k$  while  $\omega$  is real. The relation  $k(\omega)$  has five roots, and cannot be obtained analytically. We obtain  $k$ -branches using numerical root-finding after setting the parameters for the equation.

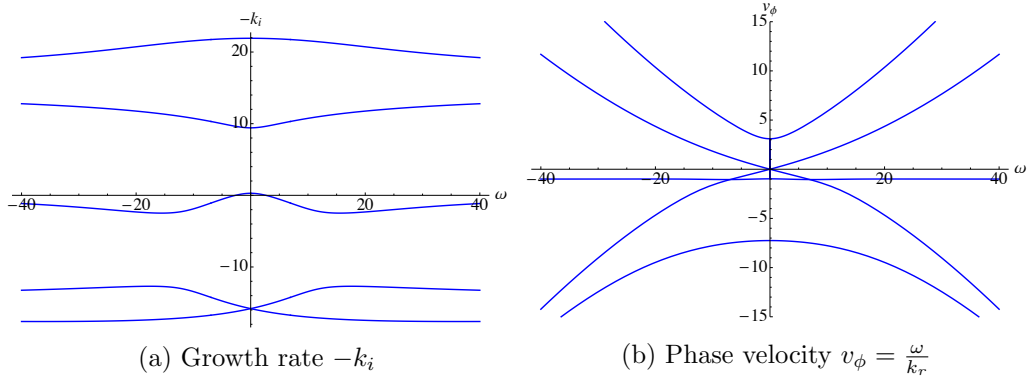


Figure 6.4: Spatial analysis of the falling viscous curtain. The absence of a dispersive coefficient leads to symmetric graphs. Values of the parameters and chosen slice are the same as in figure 6.4.

Both the temporal and spatial analysis cannot predict a growing instability. The linear instability predicted in the temporal framework is however a necessary condition. We will study the averaged one dimensional flow in the spatiotemporal framework in the following paragraphs.

#### 6.1.4 Stability analysis: spatiotemporal framework

##### High order equation and the structure of complex maps

In the spatiotemporal framework, both  $k$  and  $\omega$  are complex numbers. In the case of the LCGL, only one cusp was apparent, it was due to a single cancellation of both the derivatives of  $\omega_r$  and  $\omega_i$  along a path in the  $k$ -plane. The dispersion relation being of higher order in this problem, many cancellations can happen while following a straight horizontal path in the  $k$ -plane. This leads to a more complicated structure for the complex mapping from the  $k$ -plane to the  $\omega$ -plane.

As the dispersion relation is of fifth order, we know that five  $k$  branches will appear for each path in the  $\omega$ -plane. In a reciprocal manner, we expect the trajectory in the  $\omega$ -plane to display several cusps as we move in the  $k$ -plane. Since a cusp appears when two  $k$ -branches pinch each other, out of five branches we can create two pairs, leaving aside the last branch. Hence we expect two pinches to occur, and we should be able to spot two cusps in the  $\omega$ -plane. However, these two cusps are not completely independent of each other as they appear due to changes of the same functions. We will see that they are connected to each other, with the trajectory in the  $\omega$ -plane adopting complicated configurations. These originate from the presence of complex sheets that are projected in the same plane in our visualization.

As a first step, we want to label  $k$ -branches with their corresponding  $k^+$  and  $k^-$  designation. We will choose a horizontal path in the  $\omega$  plane with a rather large value for  $\omega_i$ . The five corresponding branches in the  $k$ -plane are well separated into the upper and lower half planes in figure 6.5b.

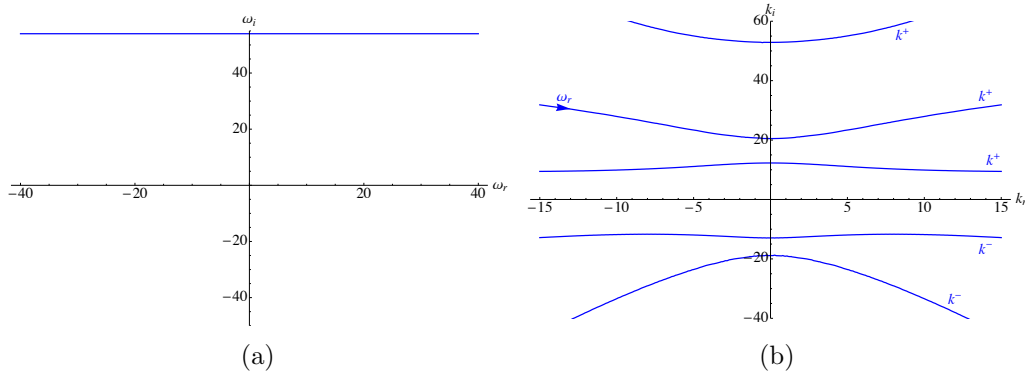


Figure 6.5: Spatiotemporal analysis of the falling viscous curtain. The dispersion relation is of order 5 in  $k$ , and one path in the  $\omega$ -plane maps to five independent trajectories in the  $k$ -plane. A horizontal path is chosen high in the  $\omega$ -plane in order to label the five  $k$ -branches with their corresponding type  $k^+$  or  $k^-$ . Values of the parameters and chosen slice are the same as in previous figures,  $\beta = 0.4$ ,  $\frac{\varepsilon^2}{\text{Je}} = 10^{-4}$ ,  $q = \frac{2\pi}{\beta}$ . The slice chosen is under transverse compression,  $x = -0.45$ .

We identify three branches of the  $k^+$  type, and two  $k^-$  branches on figure 6.5. These branches will pinch each other as the horizontal path in the  $\omega$ -plane crosses a cusp. We will be looking for a pinching between a  $k^+$  and a  $k^-$  branch.

By following a horizontal path in the complex  $k$  plane, we will visualize the different cusps in the  $\omega$ -plane. Figure 6.6 illustrates the apparition of cusps and how they interact as the path is lowered in the  $k$ -plane.

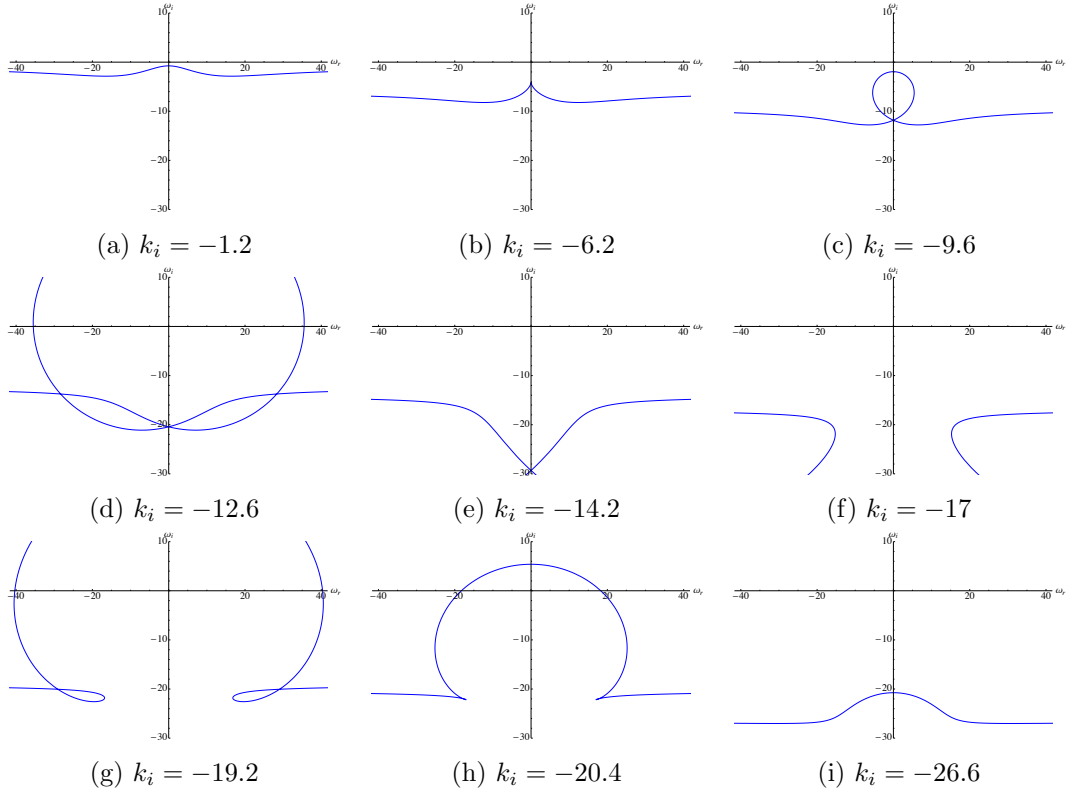
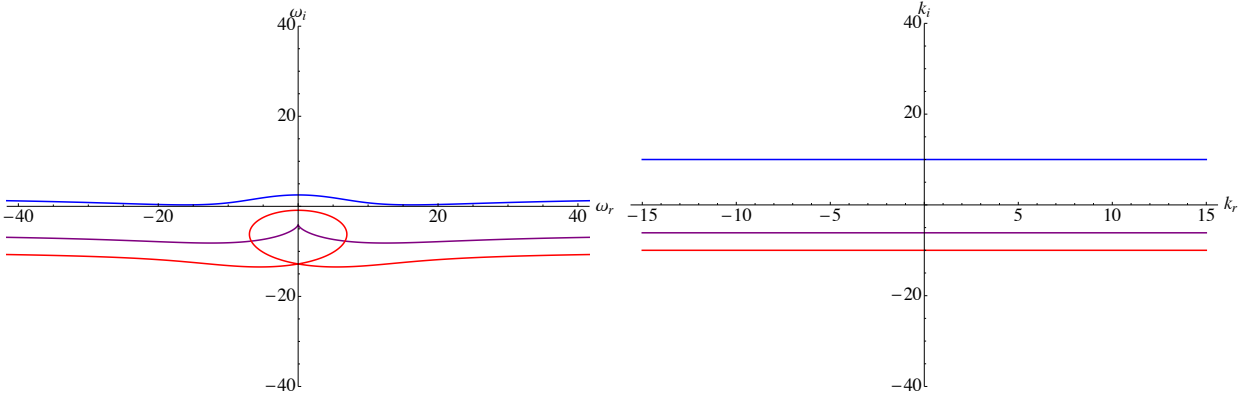


Figure 6.6: Trajectory in the  $\omega$  complex plane as a horizontal path is lowered in the  $k$ -plane for different values of the imaginary part  $k_i$ . Each curve is parameterized by the variable  $k_r$  and starts on the left hand side, exiting on the right. Far from the pinching zone where cusps appear, the trajectory is horizontal with the highest order term being predominant  $\omega \propto k^5$ . Values of the parameters and chosen slice are the same as in previous figures.

### First absolutely unstable mode

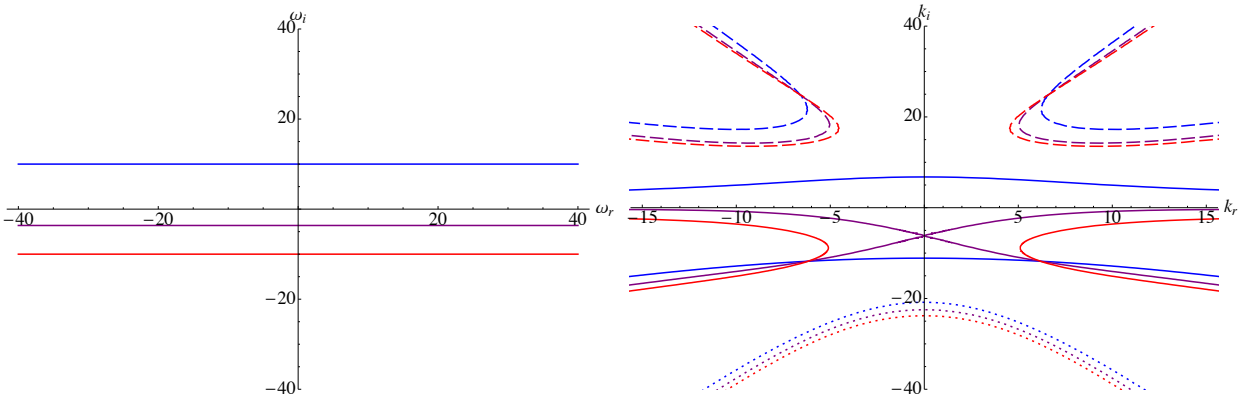
We will apply the geometrical method described in §5.2.4 to obtain the value of  $k_0$ . We choose a horizontal path in the  $\omega$  complex plane and lower it until the first pinching between two branches of opposite polarities occurs. It is important to note that since we have three  $k^+$  branches, we can expect the first pinching to occur between the first pair of  $k^+$  branches, while the second pinching should involve one branch of each type.

We present here the equivalent of figures 5.6 and 5.7, in the case of the falling viscous curtain:



(a) Curves in the  $\omega$ -plane corresponding to the paths chosen. (b) Three different horizontal paths corresponding to different  $k_i$  values are followed.

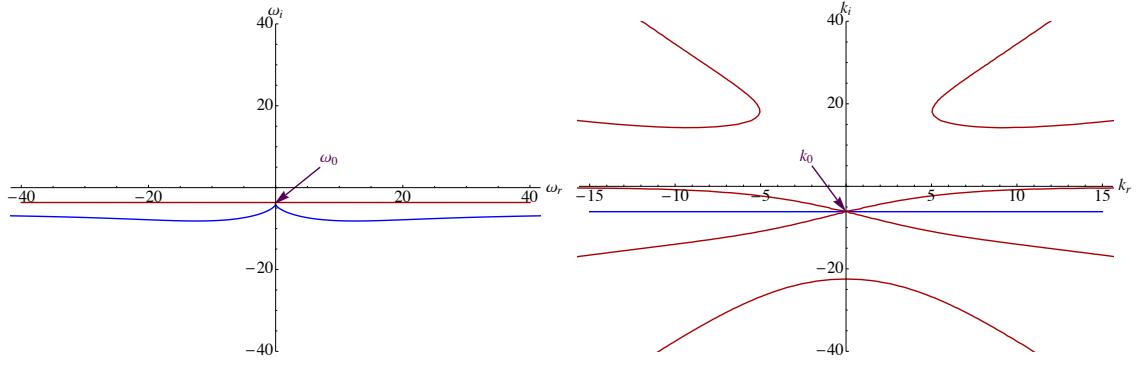
Figure 6.7: Shape of the path in the complex  $\omega$ -plane as we follow a horizontal path in the  $k$ -plane. Blue path lies above  $k_0$  in the  $k$ -plane. Purple path crosses  $k_0$ , the corresponding trajectory forms a cusp in the  $\omega$ -plane. Red path lies below  $k_0$ . Values of the parameters and chosen slice are the same as in preceding figures.



(a) Three different horizontal paths corresponding to different  $\omega_i$  values are followed. (b) Curves in the  $k$ -plane corresponding to the paths chosen.

Figure 6.8: Pinching occurs around the absolute wavenumber  $k_0$  as we follow different contours in the  $\omega$ -plane. Blue path is relatively high in the  $\omega$ -plane, but strictly under the first unphysical cusp due to the interaction between two  $k^+$  branches. They are represented as dashed curves, they have merged and can be ignored. The dotted curve corresponds to a solitary  $k^-$  branch, which does not participate in any cusp formation. Purple path goes right through the cusp and crosses  $\omega_{0,i}$ . Red path lies below the cusp, branches in the  $k$ -plane have merged. Values of the parameters and chosen slice are the same as in preceding figures.

By applying the geometrical method, we can recover the value of  $k_0$  and obtain the absolute growth rate  $\text{Im}(\omega(k_0)) = \omega_{0,i}$ . Figure 6.9 shows the correspondence between the two planes of complex  $\omega$  and complex  $k$  through the dispersion relation  $D(k, \omega; R)$  for the two paths respectively crossing  $\omega_0$  and  $k_0$ .



(a) The dark red horizontal path has equation  $\text{Im}(\omega) = \omega_{0,i}$  and goes through the tip of the cusp. The blue trajectory is the mapping through  $\omega(k)$  of the horizontal path in the  $k$ -plane.

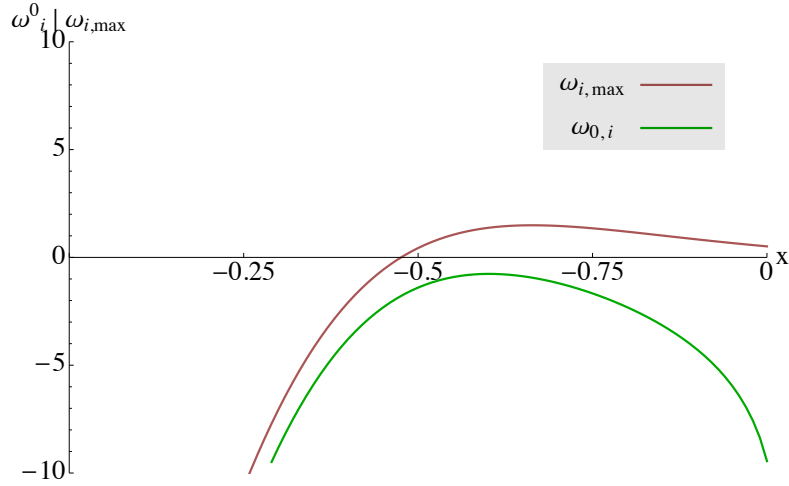
(b) The five  $k$ -branches are the five solutions to the equation  $k(\omega)$  as  $\omega$  follows the horizontal red path defined in the left figure. Because this path was chosen to go through the locus of the cusp, pinching is occurring between a  $k^+$  and a  $k^-$  branch around the location of  $k_0$ .

The horizontal blue path has equation  $\text{Im}(k) = k_{0,i}$  and goes through the position of the absolute wavenumber  $k_0$ .

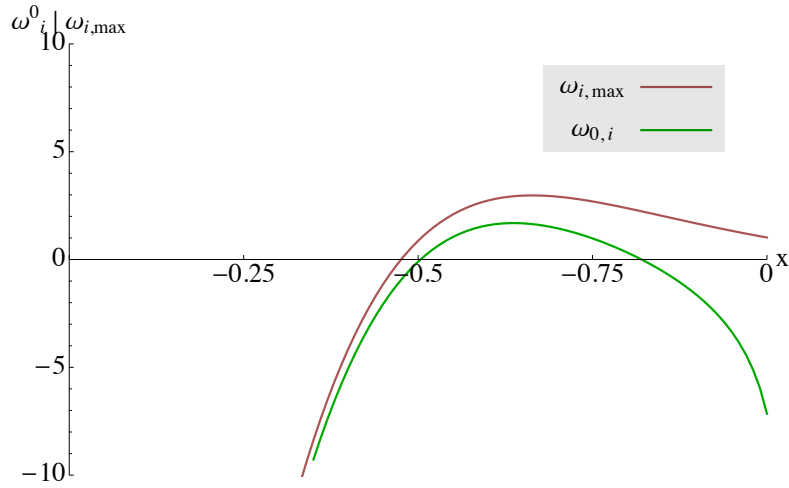
Figure 6.9: Spatiotemporal analysis of the falling viscous curtain, based on the pre-stress averaged in the transverse direction. Values of the parameters are the same as in preceding figures. We obtain  $\text{Im}(\omega(k_0)) = \omega_{0,i} < 0$ , this slice  $x = -0.45$  is convectively unstable.

This unambiguous determination of the location of  $k_0$  leads to the value of  $\omega_{0,i}$  of which the sign determines whether the flow is convectively or absolutely unstable. By applying this analysis to all slices of the averaged base flow, we can determine which parts of the flow are stable or unstable. We further refine this analysis by establishing if the instability is absolute or convective.





(a)  $\frac{\varepsilon^2}{j_e} = 10^{-4.7}$ . The linearly unstable part of the flow corresponds to a convective instability only as the green curve stays below the horizontal axis.



(b)  $\frac{\varepsilon^2}{j_e} = 10^{-5}$ . The linearly unstable part of the flow contains a region of absolute instability as a part of the green curve crosses the horizontal axis.

Figure 6.10: Result of the temporal and spatiotemporal analysis for the falling viscous curtain, values of  $\omega_{i,max}$  and  $\omega_{i,0}$  are plotted as a function of the spatial station  $x$  for different thickness parameters. Values chosen for the parameters are  $\beta = 0.4$ ,  $q = \frac{2\pi}{\beta}$ .

By reducing the thickness of the curtain, the linearly unstable zone changes from being convective only to having a region of absolute instability. In order to obtain a prediction for the threshold of the instability, we have gone through the final step of the analysis, and restore its global characteristics.

As explained in §5.3, we have to derive the analytic continuation of the function  $\omega_0(x)$  into the complex  $X$  plane. However, in our situation, the function  $\omega_{0,r}$  is identically null since all our diagrams are symmetric. Hence for every slice, the spatiotemporal analysis

leads to a cusp located on the vertical axis of the  $\omega$ -plane. This can be observed in figure 6.9a for the slice  $x = -0.45$ , where the value of  $\omega_{0,r}$  is zero. Using the Cauchy-Riemann equations we find that  $\frac{\partial \omega_{0,r}}{\partial X_r} = \frac{\partial \omega_{0,i}}{\partial X_i} = 0$ , and the analytic continuation of  $\omega_i(X)$  is independent of  $X_i$ . We conclude that the saddle-point condition is not well defined and that the maximum of the function  $\omega_{0,i}(x)$  is located at an improper saddle-point, which is actually the top of a hill in one direction, and flat in the other.

In conclusion, we find that the absolute growth rate  $\omega_{G,i}$  is located at the maximum of  $\omega_{0,i}(x)$ , which means that the system is unstable as soon as it is absolutely unstable in a finite region. By tracking when the green curve of the above figure crosses the horizontal axis, we can determine the threshold of instability of the system.

### 6.1.5 Phase diagram

After averaging the base flow, the first step is to choose a value for the transverse wavenumber  $q$ . The most unstable wavenumber is the smallest, hence we have to choose the smallest value for  $q$  that respects boundary conditions. This corresponds to the longest wavelength possible, and we choose the value  $q = \frac{\pi}{2\beta}$ . This corresponds to the first buckling mode with an out-of-plane displacement cancelling on the sides. However, we know from the numerical global stability analysis of chapter 4 and from its results in figure 4.4 that the transverse wavelength that appears is not the longest possible one. To fit with this result, we can artificially set the value of  $q$  to larger values, so that the resulting mode has the same wavelength as the one observed in the global numerical analysis. To obtain these values for  $q$ , we evaluate for each aspect ratio the wavelength  $\lambda_g(\beta)$  of the global modes by measuring the distance between two cancellations of the out-of-plane displacement  $\tilde{H}(x, y)$  along the transverse direction  $y$ . From this distance we obtain  $\lambda_g$  and  $q_g(\beta) = \frac{2\pi}{\lambda_g(\beta)}$ .

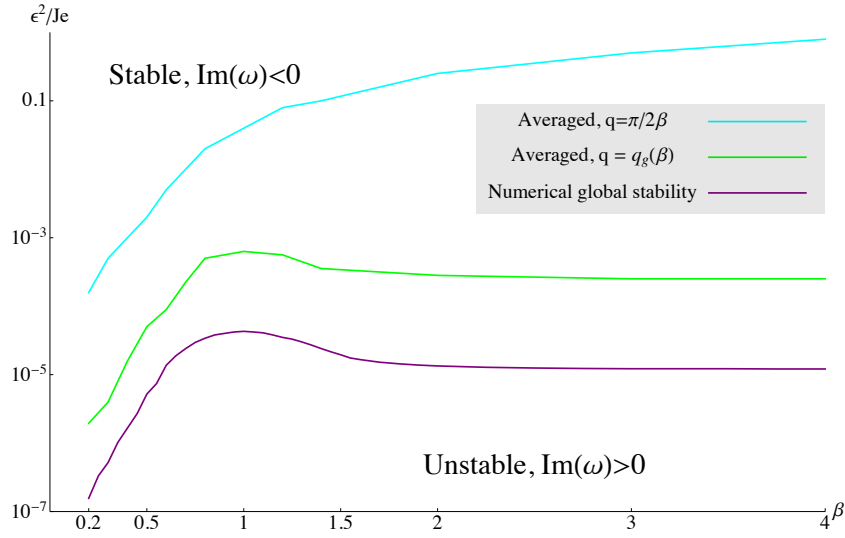


Figure 6.11: Result of the open flow stability analysis applied to the falling viscous curtain with averaged stresses in the transverse direction. The light blue curve was obtained for a value of  $q = \frac{\pi}{2\beta}$  corresponding to the fundamental buckling mode, that spans half a wavelength across the width of the curtain. The green curve was obtained by setting  $q$  to a value  $q_g(\beta)$  so that it reproduces the wavelength appearing in the results of the numerical global stability, see figure 4.4. The purple curve is the phase diagram obtained in the numerical global stability analysis, see §4.3.

The phase diagram corresponding to the most unstable mode of longest wavelength does not reproduce the phase diagram resulting from the global numerical stability analysis. By artificially choosing a shorter wavelength in order to study eigenmodes with the same transverse wavelength as the predicted global mode, we can recover the general shape of the stability threshold in the phase diagram, see the form of the green curve in figure 6.11.

These results steer towards two important conclusions. First, the infinite flow does not seem to be a good approximation for the base compressive flow, as no wavelength selection process is retained. The analysis in slices means that we have to study an infinite flow both in the stream-wise and in the transverse directions, and this eliminates any transverse dependence that could contribute to wavelength selection. Secondly, it can be argued that averaging the transverse dependence of the flow is a strong hypothesis, especially for larger aspect ratios  $\beta$  for which stress maps (see figure 4.4) clearly indicate that compressive stresses are localized in small regions, with strong inhomogeneity along the width of the curtain. This crude approximation may contribute to the difference observed between the phase diagram corresponding to the global stability analysis (in purple) and the one coming from the averaged local stability analysis (in green). Inserting the value  $q_g(\beta)$  in order to reproduce the wavelength obtained in the numerical global study is only sufficient to recover the general shape of the phase diagram. However, a quantitative difference remains, the gap between the two predicted thresholds is of an order of magnitude on average. It is worth noting that a linear stability analysis such as this one only intends to lead to a necessary condition, giving a more pessimistic, larger thickness threshold than the one of the real system. We indeed obtain such a condition,

albeit very conservative, and predicting the appearance of the fundamental mode. If we have additional knowledge about what buckling mode will be preferred by the real system, we can use the averaged study and insert a pre-calculated value for  $q$ . This leads to a necessary condition with improved precision.

This averaged study presented the great advantage of letting us carry the whole set of computations in a completely analytical manner. We obtained an explicit expression for the dispersion relation, the averaging in the width makes boundary conditions easy to apply and boil down to a choice for  $q$ , and the complex mapping  $\omega(k)$  and its inverse could be easily drawn out. Once again, the instability criterion obtained with the averaged study is only a necessary condition and the actual instability threshold always lies underneath it in the phase diagram.

We will now restore the transverse dependence for stresses, however this will prevent us from solving the equation analytically and requires a numerical study, implying a generally more complicated analysis.

## 6.2 Local stability analysis of the two-dimensional flow

By retaining the full dependence of the base flow in the transverse direction we hope to predict more precisely the threshold of instability of the compressed falling viscous curtain. We will apply the stability analysis of open flows without averaging the base flow in the transverse direction. This means that the set of parameters  $R$  that must be determined at each spatial station  $x$  now contains the values of the stress tensor that are functions of the coordinate  $y$ . We also have to take into account the exact boundary conditions on the sides.

### 6.2.1 Boundary value problem

We now have to assume a more general form for the transverse dependence of the unstable mode. After slicing the flow, we still study an infinite flow in the stream-wise direction, but that now bears a finite width along with free stress boundary conditions on the lateral edges. Hence, we choose a perturbation of the form  $H(x, y, t) = \Phi(y) e^{i(kx - \omega t)}$ .

The next step is to insert this form in the equation of motion for the out-of-plane displacement  $H(x, y, t)$ , while taking into account the applied boundary conditions. This operation defines a boundary value problem on the function  $\Phi(y)$ , that can be expressed as a generalized eigenvalue problem. We will use the previously introduced finite elements scheme in order to solve it. Since boundaries are stress-free on both sides of the curtain, the finite elements scheme can be used to solve the weak form associated with the out-of-plane displacement  $H$  without applying any kinematic boundary condition.

After specifying the set of parameters and choosing a slice, we select a value for the complex wavenumber  $k$  and obtain the eigenvalue  $\omega$  along with the corresponding eigenvector  $\Phi(y)$ . By sampling the complex  $k$ -plane in this manner, we can obtain the trajectories in the  $\omega$ -plane corresponding to a given path in the  $k$ -plane.

### Phase diagram

Since we solve numerically and obtain values of  $\omega$  as a function of  $k$ , we cannot use the previously described geometrical method. However, we can sample the space of  $k$  values, and find cusps in the  $\omega$  plane. When this is done, it is possible to visualize the

inverse relation by selecting all data points in a line crossing the location of the cusp, and looking at the corresponding path in the  $k$ -plane. It must correspond to the pinching of two  $k$ -branches, forming a cross. This helps determining the exact location of the cusp and we can read its imaginary part in order to determine whether the flow is convectively or absolutely unstable.

We determine the most unstable slice for each aspect ratio  $\beta$ , then focus on varying the value of the destabilizing parameter  $\frac{\epsilon^2}{Je}$  in order to find when the absolute growth rate  $\omega_{0,i}$  becomes positive, marking the transition to an absolute instability.

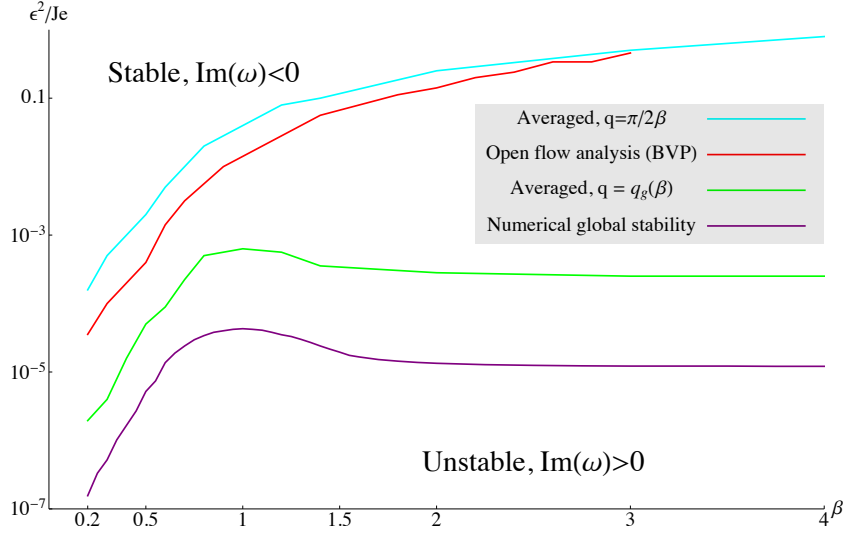


Figure 6.12: Result of the open flow stability analysis applied to the falling viscous curtain with full dependence of stresses in the transverse direction. Light blue (fundamental mode, averaged stresses), green ( $q = q_g(\beta)$ , averaged stresses), and purple (numerical global analysis) diagrams are the same as in figure 6.11. The red curve is the phase diagram obtained by numerically solving the boundary value problem (open flow analysis of the curtain taking into account the transverse dependence of stresses).

For every aspect ratio, the most unstable mode selected by solving the eigenvalue problem features the longest wavelength possible within the width of the curtain. The boundary value problem does not lead to shorter wavelength wrinkling modes. This indicates that the wavelength selection in the original two-dimensional problem isn't only due to the transverse dependence of the flow, but also to the stream-wise evolution of the flow. This originates in the nature of the equations of elasticity that feature a Laplace operator, hence coupling the vertical and horizontal deformations and stresses.

### 6.2.2 Stretched base flow and predicted global mode

Due to the nature of the equations governing the out-of-plane buckling of the curtain, the variation of stresses in the stream-wise direction plays an important role in the selection of the transverse wavelength. When using the framework for the study of open flows instabilities, we consider an infinite flow in the stream-wise direction at each slice. This method does not give good results if the stream-wise variation is too quick, as it is fundamentally a WKBJ approximation, that supposes a slowly varying background

flow. We conclude that the background flow presents gradients of stresses in the stream-wise direction that are too quick for the slice by slice local stability approach to give good results. If the variation of longitudinal stresses in the base flow was slow enough, the open compressive flow framework should be able to predict the most unstable mode correctly.

We would like to test this hypothesis, and will modify the base flow in order to reduce artificially stream-wise gradients of stress. This can be done by dilatation of the axis  $x$ , the effect of such a transformation is to attenuate stress gradients in the direction  $x$  only, while the transverse variations of the stress are kept identical. We can then expect the transverse wavelengths of the flow, due to the stress map or to its physical size to recover importance, as predicted by the local stability analysis of the open flow.

We will transform the domain of study by multiplying the coordinate  $x$  by a dilatation factor  $\xi$ . The domain becomes  $x \in [-\xi, 0]$ ,  $y \in [-\beta, \beta]$ . We designate the velocities in the elongated domain by  $u_{\alpha}^{\xi}$ . We will map the gradients of velocities  $\bar{u}_{\alpha}^{(0)}$  from the original domain to the elongated domain in the  $x$  direction and we have the relations  $u_{\alpha,\beta}^{\xi}(x, y) = \bar{u}_{\alpha,\beta}^{(0)}(\frac{x}{\xi}, y)$ , where  $\bar{u}_{\alpha}^{(0)}$  corresponds to the base flow obtained in §4.1.

In that situation, the stress tensor in the elongated flow  $N_{\alpha\beta}^{\xi}$  is related to  $\bar{N}_{\alpha\beta}^{(0)}$  through the relation  $N_{\alpha\beta}^{\xi}(x, y) = \bar{N}_{\alpha\beta}^{(0)}(\frac{x}{\xi}, y)$ . We can see that the gradients of the stress rate tensor will be reduced in the streamwise direction only:

$$\begin{aligned} N_{\alpha\beta,x}^{\xi}(x, y) &= (N_{\alpha\beta}^{(0)}(\frac{x}{\xi}, y))_{,x} = \frac{1}{\xi} N_{\alpha\beta,y}^{(0)}(\frac{x}{\xi}, y) \\ N_{\alpha\beta,y}^{\xi}(x, y) &= (N_{\alpha\beta}^{(0)}(\frac{x}{\xi}, y))_{,y} = N_{\alpha\beta,y}^{(0)}(\frac{x}{\xi}, y) \end{aligned}$$

With this transformation applied on the base flow, we use the numerical global stability analysis to solve the out-of-plane equilibrium equations obtained in §3.3.4.

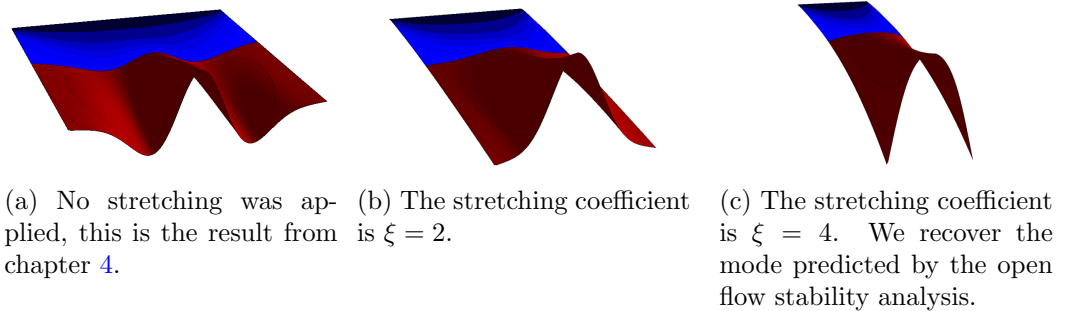


Figure 6.13: Shape of the most unstable buckling mode obtained with a numerical global stability analysis using elongated velocity gradients in the  $x$  direction. The aspect ratio of the unmodified domain is  $\beta = 0.4$ .

We can see that stretching the flow in the vertical direction has a clear effect on the eigenmode obtained through a numerical global stability analysis. The standard flow with no artificial stretching buckles in a mode presenting three extrema, emphasizing the fact that a characteristic length is underlying in the stress map. It is interesting to note that by stretching the flow in the vertical direction twice, a mode of lower order appears, however it is still not the fundamental mode. The flow has to be scaled by a factor of 4 in the vertical direction to recover the fundamental mode, presenting only one

extrema. This is exactly the mode predicted by the local stability analysis of the infinite flow, both analytically by choosing the most unstable value for  $q$ , and also numerically with free boundary conditions.

By slowing the streamwise development of the flow in this way, we can recover the modes predicted by the local stability analysis of open flows. The coupling between the streamwise and the transverse directions is due to the elastic origins of the viscous membrane equations, that feature a Laplacian operator. The open flows stability analysis assumes a slowly evolving flow in the streamwise direction, and it appears that the gradients of stresses in that direction for a falling viscous curtain are too important.

## Partial conclusion

The study of the stability of open flows requires to take into account the advection velocity that sweeps fluid particles along with the flow. This advective effect permanently injects new particles that replace the material in the volume of the flow, while some particles are evacuated at the outlet. When an instability develops in such a flow, it can be advected away by this phenomenon that replaces the perturbation with renewed, unperturbed fluid elements. Hence, instabilities in open flows must be able to crawl back up the flow and resist the advective effect, which leads to a specific instability criterion. A framework enabling the study of open flows unstable with respect to shear stress has been developed by the fluid mechanics community and was described in detail in chapter 5. We applied its methods to a mathematical model capturing the essential phenomena encountered in fluid dynamics: the linear complex Ginzburg-Landau equation.

This framework for the stability analysis of open flows isn't specific to instabilities driven by shear, and we presented in this chapter how it can be transposed to the out-of-plane equilibrium of a viscous sheet under compressive stress. The instability of the falling viscous curtain described in part II is a mechanical instability that changes the shape of the free surface of the flow. This buckling instability is due to compressive stresses in the base flow that appear parallel to the transverse direction.

The stress map of the base flow is two-dimensional, which means that when we extract the parameters of the local stability analysis at a specific slice, stresses appear as functions of the transverse direction  $y$ . The stability analysis will lead to a dispersion relation  $\omega(k)$  featuring an unknown function of the transverse direction  $y$ , which represents the shape of the buckling mode. This problem can be simplified by making assumptions on the shape of this function. However, by taking into account boundary conditions corresponding to free edges for the curtain, it can also be solved numerically as a boundary value problem.

In the first step of the study §6.1, we considered an averaged pre-stress map in the transverse direction. By getting rid of the dependence in the  $y$  variable of the base flow, the extracted infinite flow of the local stability analysis is also invariant by translation along the  $y$  direction. This means that we can insert sinusoidal modes in both the  $x$  and  $y$  directions. The associated wavenumbers are respectively called  $k$  and  $q$ . In that situation, the smallest values of  $q$  are the most unstable, which means that the buckling mode selected according to the averaged local stability analysis is the mode of longest wavelength that accommodates the width of the system. Hence we expect buckling to occur adopting a deformed shape corresponding to the fundamental mode. However, we know from the results of the numerical global stability that the observed buckling mode is of higher order and spans multiple wavelengths across the width of the curtain (figure 4.4). We tried to improve the results of the averaged local stability analysis by artificially selecting a larger value for  $q$ , which imposes a buckling mode with the correct wavelength. The results of this averaged analysis were shown in figure 6.11. From these phase diagrams, we can gather two important conclusions. First, the most unstable mode according to the averaged local stability is the fundamental one. This means that this analysis does not correctly predict the wavelength that was observed in the global stability analysis. Secondly, if we artificially select a transverse wavenumber  $q$  that reproduces the observed buckling mode, the phase diagram obtained using the local open flow stability analysis is in much better agreement with the one coming from the numerical global stability. We can see in figure 6.11 that the discrepancy is of an



order of magnitude approximately in the parameter  $\frac{\varepsilon^2}{J_e}$ . The averaged local stability let us obtain a necessary condition for buckling, but does not predict precisely the threshold of instability. It does not either predict the wavelength observed in the global numerical study.

In the second step of the study §6.2, the transverse dependence of the base flow is restored along with the free edges boundary conditions. As mentioned earlier, this problem is solved numerically, by expressing the boundary value problem as a generalized eigenvalue problem that we implement in a finite elements library. This numerical resolution outputs both the eigenvalue and the eigenvector, which gives the spatial dependence of the associated buckling mode in the transverse direction  $y$ . The mode predicted is always the fundamental one, having the largest wavelength that fits in the domain. We hoped that retaining the transverse dependence of the base flow would be enough to correctly explain the wavelength selection process, however this is not the case. The open stability analysis, because of its underlying WKBJ approximation cannot take into account strong gradients along the streamwise direction, and we conclude that these may be responsible for the wavelength selection it failed to capture.

# Conclusion

The focus of this PhD work was on the buckling stability of a thin structure made up of a viscous fluid and in open flow. We have seen throughout the presentation of the results that this problem lies at the boundary between fluid and solid mechanics. As a consequence of this, methods from both these fields have been applied, sometimes requiring adaptation, and led to a numerical and analytical study.

We considered a vertical sheet made up of a viscous fluid and falling into a bath. This curtain is formed by an inlet injecting viscous fluid at the top of the domain and creating an open flow. The resulting thin structure is falling under the effect of gravity, and has been seen to develop regions of compressive stress. Those can engender a mechanical instability in the structure as the sheet can buckle under compression, losing its planar geometry and deforming in the out-of-plane direction.

Studying a thin structure made up of a fluid and sensitive to out-of-plane buckling requires the use of specific models. On the one hand a viscous flow develops in-plane velocities in two dimensions, while on the other hand buckling causes a displacement of the free surface of the sheet. This required the use of elaborate kinematics to model the curtain, mixing velocities and displacements. We used a viscous membrane model; inspired by the solid mechanics of thin structures it uses the Stokes-Rayleigh analogy to transpose the concepts of stretching and bending stress to a viscous problem. By using the principle of virtual work, we could derive the equations of the two-dimensional flow developing in the sheet under the effect of gravity (eq. 3.16). The principle of virtual work leads to equations in weak form, that represent a quantity that cancels when static equilibrium is reached. These formulations offer the important advantage of being easy to implement in a numerical finite elements scheme (§2.1). Because they simplify the usage of the numerical tool, weak formulations are particularly adapted to the study of continuum mechanics and especially of thin structures. Another advantage of using weak forms is that the associated static equilibrium requirement enforces natural boundary conditions at the edges of the integration domain. Only kinematic boundary conditions have to be explicitly included in the numerical solver (§1.4). By imposing boundary conditions corresponding to the advection velocity at the top boundary and to free stress on other edges (tab. 3.1), we obtained the two-dimensional flow that develops in the viscous curtain as it falls down under the effect of gravity. Using this velocity field, we visualized the values of the local stress tensor and obtained the map of pre-stress in the curtain. This two-dimensional stress map has been derived for viscous sheets of various aspect ratios, and compressive regions have been observed in all of them (fig. 4.3). For larger aspect ratios  $\beta$ , the compressive regions were observed to localize in the lower corners of the curtain. The appearance of compressive stresses was explained by analogy with the Poisson's effect of solid mechanics. Because the curtain is being stretched in the vertical direction, a horizontal flow appears which drives material elements closer to each other, giving rise to compressive stress (§4.1.1). After obtaining those stress maps and noticing that regions of compressive stresses develop in the curtain, we expect the thin structure to be unstable and to buckle if it is thin enough. Buckling of a viscous layer has already been an active subject of research, but it was only observed in configurations featuring a direction of invariance. The buckling

of a viscous membrane subjected to a fully two-dimensional pre-stress with only one axis of symmetry was a new development. In order to obtain the equations for the out-of-plane equilibrium we used once again the principle of virtual work and studied the appearance of a deflection  $H(x, y, t)$ . As we study an open flow, this derivation must take into account the fact that material elements are being advected at a prescribed velocity, and we used comoving derivatives. The resulting equations feature a fifth order spatial derivative, making numerical implementation trickier (§4.2.2). After defining the kinematic boundary conditions, that are also affected by the open nature of the flow (§3.2.3), we used a simple idea from discontinuous Galerkin methods associated with  $C^1$  elements to overcome this difficulty. The solutions of this numerical global stability analysis are high order buckling modes, spanning multiple wavelengths along the width of the curtain (fig. 4.4). This wrinkling phenomenon is rather unexpected as one would instead anticipate the appearance of a fundamental buckling mode, as is the case for an unstable *Elastica*. Because the buckling instability involves a fluid thin structure, we also considered capillary effects. They tend to reduce the surface of the interfaces of a liquid system, and are observed to stabilize the curtain as they limit its out-of-plane deflections (fig. 4.8). Because of the unexpected appearance of buckling modes of shorter wavelength than the fundamental mode, we suspect that this wavelength is related to a characteristic length scale present in the stress map.

Although the numerical resolution is a very powerful tool, we wanted to get a better understanding of the instability and be able to predict the conditions under which it manifests. This is the reason why we turned to an analytical method, a local stability analysis able to predict the onset of the instability. The fact that the thin viscous curtain is in open flow affects the development of instabilities in the system. The permanent advection velocity drags along with it any instability that develops, and in order to grow, an unstable mode must be able to remain at a fixed location in space by crawling up the flow. Local stability analysis requires to take this effect into account, and we used a framework developed for the study of unstable open shear flows unstable under the effect of shear stresses (chap. 5). We had to adapt the method and applied it to the out-of-plane equilibrium equations. The local stability analysis was first led on an averaged pre-stress map, enabling us to carry a completely analytical derivation and to obtain a prediction for the instability threshold. We recall that once again, the high order of the equations had important consequences (§6.1.4). Following this analysis, the most unstable mode is the fundamental buckling mode, of largest wavelength. Restoring the transverse dependence of the flow led to similar results. Hence the prediction for the instability threshold is poor as it does not even correspond to the correct buckling mode. We tried to improve on this prediction by using our knowledge of the expected buckling mode, we assumed a solution possessing the observed wavelength and used it in the averaged open flow stability analysis. This leads to a phase diagram that reproduces the general shape of the one obtained numerically, but with an important error on the predicted instability threshold of around an order of magnitude (fig. 6.12).

We presume that the wavelength selection process is mainly driven by gradients in the streamwise direction, which are assumed to be small in the framework of open flow stability analysis. The strain gradient in the streamwise direction has been verified to play a very important role, as the global stability analysis in an artificially stretched domain leads to the fundamental buckling mode (fig. 6.13). In the falling viscous curtain, the gradient of stress in the streamwise direction varies too rapidly, and since vertical and horizontal directions are coupled by the viscous membrane equations, the local stability

analysis fails to capture the wavelength selection process and cannot predict accurately the threshold of the buckling instability.

We could therefore verify that the stress gradients in both the longitudinal and transverse directions play an important role in the wavelength selection for the buckling of the falling viscous curtain. In future work, we would like to get a quantitative evaluation of their respective effects. By using manufactured flows featuring controlled gradients, we should be able to predict the conditions in which one direction becomes dominant for the wavelength selection process. This knowledge can be extended into a criterion estimating *a priori* the accuracy of a local stability method. Based on the operators appearing in the equations and the magnitude of their different components, we could evaluate whether the approximations required by an analytical study are acceptable or would lead to inaccurate results.

Another natural evolution for this problem would be to explore new geometries involving the open flow of a viscous sheet, and featuring compressive stresses. Inspired by open shear flows, we can imagine the flow of a viscous layer encountering a rigid obstacle, like a cylinder for example. We can expect compressive stresses to appear ahead of the obstacle, as the fluid is forced to move around the obstacle. Some compressive regions may also appear in the wake of the cylinder.

Moving back to the roots of the falling viscous curtain, we remember that all thermal effects that play a very important role in the actual glass-making process were ignored in this study, as we restricted ourselves to a constant and homogeneous viscosity. We can restore the dependence of the viscosity on the temperature, by imposing a temperature profile along the height of the curtain. On the one hand, this effect should be expected to be stabilizing, as a higher viscosity makes buckling more difficult, but on the other hand, the hardening of the fluid could lead to a freezing of a buckling pattern in formation.

We also recall that we have assumed a small effect of gravity while advection velocity was important. The limit  $Je \ll 1$  enabled the assumption of small deformations of the curtain and we could consider a rectangular domain for the flow. By restoring values of order 1 for Jeffreys number, large deformations of the curtain must be expected, which leads to a free boundary value problem. Determining simultaneously the geometry and the velocities of the flow is more difficult but opens the study to a larger range of parameters.

Last but not least, the numerical study presented in this work only resolved the steady planar flow of the curtain as well as a global linear stability analysis. This is enough to predict the onset of the instability and its threshold as a function of the parameters of the flow. However it gives no insight about the nonlinear post-buckling behaviour of the curtain. A direct numerical simulation would be necessary to obtain the complete time dependent dynamics of the system. Two codes appear as good candidates in this endeavour, Discrete Viscous Sheets [BUAG12] and Gerris [Pop03]. The former is particularly adapted to the thin geometry we consider, however it has not yet been entirely validated and preliminary work to this end is necessary. The open nature of the flow can also be expected to make implementation more difficult. The software Gerris on the other hand is perfectly able to take into account all the physical components of the problem. However, the thin geometry may cause complications as large scale differences between dimensions of the domain can hinder convergence and drive the computational cost up.



# **IV**

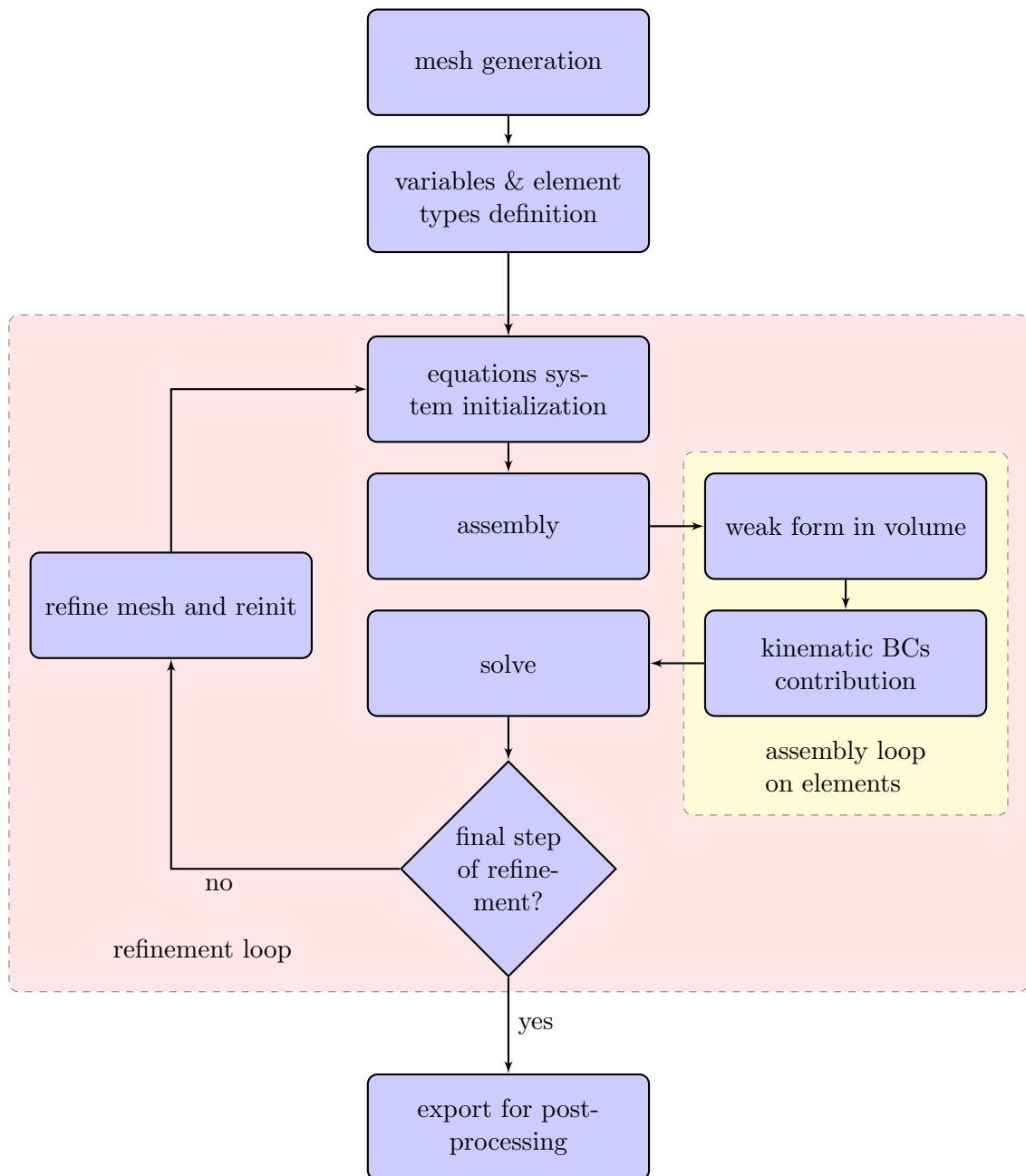
## **Appendices**



## Appendix

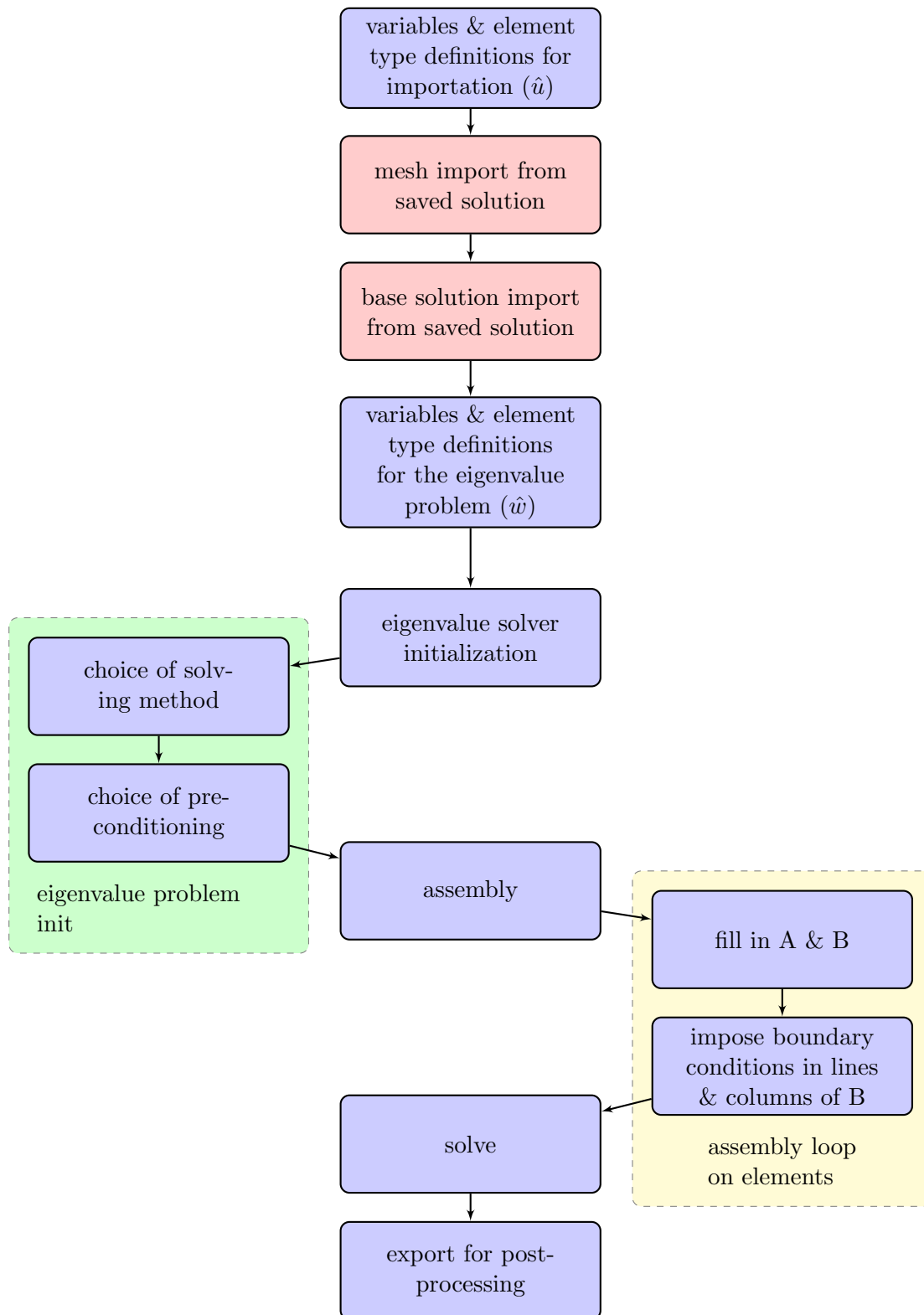
# A Program structure of the finite elements solver

The following flow chart represents the structure of the program used to solve for base solution, see §2.2 and §4.1.





The following flow chart represents the structure of the program used to solve an eigenvalue problem, see §2.3 and §4.2.



## **Appendix**

# **B**

## **Article draft**

The following is a mid-2014 draft for an article regrouping results from part [II](#), for the latest updated results please refer to the contents of this manuscript.

# Stability of a viscous curtain falling in a vertical open flow

C. Perdigou<sup>a</sup>, B. Audoly<sup>b,a</sup>

<sup>a</sup>UPMC Univ. Paris 06, UMR 7190, Institut Jean le Rond d'Alembert, Paris, France

<sup>b</sup>CNRS and UPMC Univ. Paris 06, UMR 7190, Institut Jean le Rond d'Alembert, Paris, France

---

## Abstract

*Keywords:* solid mechanics, viscous sheet, curtain, Rayleigh Stokes analogy, buckling, compressive flows

---

## 1. Introduction

Viscous flows have received a lot of attention in academic research because of the very large amount of possible industrial applications. Their importance appears at many different scales, from microscopic biological phenomena to the movement of continents in earth sciences, they are at the core of many scientific fields. An interesting feature of viscous fluids is that they build up stress when deformed, as they need some time to relax. This has caught the attention of experimentalists and in a seminal work by G.I. Taylor in 1958, he experimented with a thin layer of viscous fluid, floating on a denser fluid [25]. By diving a disk in the volume of the viscous fluid and rotating it, he revealed that above a critical angular velocity, a steady wave pattern forms on the surface of the liquid. This buckling occurs because of the shear stresses that build up with the rotation of the disk. Additional studies in a Couette configuration later led to heuristic conclusions [24] and the scaling laws obtained were confirmed with theoretical developments by Benjamin and Mullin [2]. A strong model for the behaviour of thin viscous sheet was introduced by Ribe in 2002 [21]. Commentary on an article by Slim et al. in 2012 [22, 27] by the same author further expands on this theory, revealing the importance of a priori non physical asymptotic terms. In another important clarification to this article, Bhattacharya et al. [3] use the Foppl-von K arm an equations in the axisymmetric configuration.

Whether in a Couette configuration or when studying an infinite strip submitted to shear, all previous studies have in common an axis of symmetry that gives the pre-buckled state strong symmetries. In the present article, and contrary to previous investigation no strong symmetry is present, and the problem is fully two-dimensional.

Modelling of viscous sheets has many applications, and this study was motivated by a glass forming process first patented in 1967 by S.M. Dockerty [8]. In this process, a triangular gutter is filled with molten glass, which overflows and slowly covers its external hull. Upon reuniting at

the bottom of the triangle, a thin sheet of glass is formed. We study the flow that develops as the glass falls freely forming a liquid curtain. This thin sheet of viscous fluid presents extensive and compressive zones which make the system sensitive to buckling. The attainable size for a glass panel made using this technique is thus in question, as the thin curtain could be destroyed by a buckling instability. Buckling of the fluid curtain appears as wrinkling of its surface caused by compressive stresses. This phenomenon has been the subject of numerous previous studies in the case of elastic membranes.

Wrinkled elastic membranes have been studied extensively because they are of interest in a wide array of engineering applications. Originally the analysis of membranes was carried out using tension field theory, e.g. gravity induced wrinkles in variously shaped membranes in [18]. An experimental display by Cerda et al. recently caught the attention of the scientific community [5, 10]. By stretching a rectangular elastic sheet clamped on its short edges, wrinkles appear along the width of the sheet. By preventing strains due to Poisson's effect from appearing near clamped edges, a strongly compressed state develops in the direction orthogonal to that of stretching. These stresses are relaxed by a buckling phenomenon that leads to wrinkling. Assuming homogeneous compression scaling laws can be predicted for the wavelength and the amplitude of the wrinkles.

Other than Friedl et al. [10], significant numerical results were obtained on this problem a few years later, notably by Kim et al. [12], Nayyar et al. [19] and in the Ph.D. thesis of Zheng [29]. In Puntel et al. [20], authors are able to give a better analytical understanding of the wrinkling of stretched thin sheets assuming in the context of a small slope approximation. This approximation is later relaxed in numerical experiments by Kim et al. [12]. They find that sheets always display an even number of wrinkles, which is also the case of our symmetric buckled solutions. They also reference Fischer et al. [9] as taking into account an inhomogeneous pre-buckled state in their discussion of the so-called "towel buckling". Authors of [9] express the

---

Email address: [perdigou@dalembert.upmc.fr](mailto:perdigou@dalembert.upmc.fr) (C. Perdigou)

wrinkles as a cosine with a strong decaying amplitude towards free edges. Experimental investigation as well as the numerical results obtained in those references all display strong resemblance to the results obtained in the case of our study.

Levering on this strong background both in the field of wrinkled elastic membranes and buckled viscous sheets, we will be able to predict when the viscous curtain we study will buckle. The models we use are typical in the study of viscous membranes, while the geometry and the numerical results are very close to problems of wrinkling of elastic membranes. Alliance of gravity induced instabilities and wrinkling of a viscous fluid was already studied in a very elegant experiment by Debrégeas et al. [7] with theoretical description by da Silva et al. [6]. They observed a bubble bursting at the surface of a viscous fluid. As the bubble is poked at its apex, the hole that forms expands slowly because of viscous stresses, which gives time to the bubble to fall and flatten under the effect of gravity. This phenomenon creates hoop stresses that lead to a buckling phenomenon in the shape of radial wrinkles. A similar experiment was studied by Boudaoud et al. [4] where a small viscous disk at the surface of water is poked and forms wrinkles due to hoop stresses. Our study differs from these previous work for two main reasons. First, we study a stationary flow. A common property of these previous references is that they consider the viscous membrane as static, and feature no flow at all (wrinkling happens on a time scale smaller than the viscous relaxation). Secondly, we take into account a full blown two dimensional problem, and have no strong symmetries unlike the axisymmetric configurations of the previous references.

In order to predict when the viscous curtain under study will buckle, we first need to model the viscous flow that develops during its free fall. In section 2 we will use a solid mechanics thin plate model to describe the flow in the curtain, and its out of plane buckling. These equations will be solved in section 3 to obtain the pre-buckled state, i.e. the stationary flow that develops as the curtain falls. The buckling modes can be obtained numerically, and we will describe in section 4 how the out of plane equilibrium is solved. After section 2 capillarity will be neglected, we will see in section 5 its stabilizing effect and small corrections to the results obtained throughout the article.

## 2. Model equations adapted to the falling sheet

In this section we present the model equations for viscous films where flow is driven by gravity forces. We will consider surface tension to apply and consider boundary conditions with an injection velocity.

### 2.1. Assumptions and notations

We use Cartesian coordinates  $(x, y, z)$ : the three dimensions of the model are one transverse to the sheet ( $z$  axis), one in the width of the sheet ( $y$  axis) and one aligned

with the direction of gravity ( $x$  axis) as represented in figure 1.

The top of the sheet, where the fluid is injected, corresponds to  $x = -\mathcal{H}$  and the bottom, where the fluid exits to  $x = 0$ . In the  $y$  direction, the position of the centre of the sheet is  $y = 0$  and the position of the edges are  $y = \pm\mathcal{H}\beta$ . When symmetries allow, we will apply a corresponding boundary condition, and restrain our study to the domain  $x \in [-\mathcal{H}; 0]$  and  $y \in [0; \mathcal{H}\beta]$ .

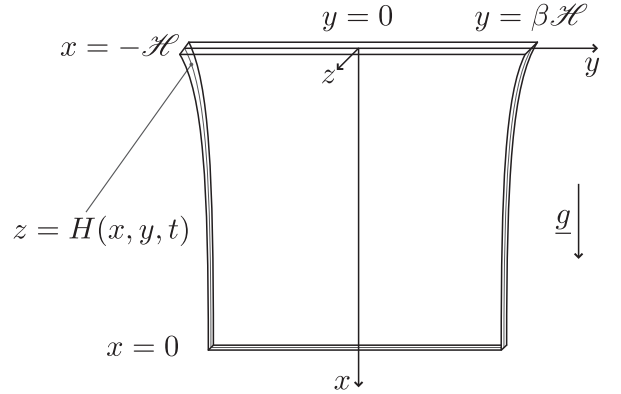


Figure 1: Frame of reference and geometry of the falling sheet.

Greek letters will be used to denote generic indices in the plane of the sheet (directions  $x$  and  $y$ ), we will also assume summation over repeated indices.  $\phi_{,x}$  denotes the partial derivative of the generic function  $\phi$  with respect to the variable  $x$ .

At any time  $t$ , let  $z = H(x, y, t)$  be the position of the sheet's centre surface, and  $h(x, y, t)$  its thickness. All the variables are time-dependent. To handle shorter notations we will not precise the time dependence next to each variable in the following. The velocity field is two dimensional and is denoted by  $\underline{u}(x, y, z) = (u_x(x, y, z), u_y(x, y, z))$ .

The surface tension  $\gamma$  between the liquid and ambient air is assumed to be constant. The density of the sheet material is denoted by  $\rho$  and its dynamic viscosity by  $\mu$ . Volume forces corresponding to the effect of gravity and of capillarity are respectively of order  $\rho g$  and  $(\gamma H^*/\mathcal{H}^2)/h^*$ , where  $g$  is the acceleration of gravity,  $H^*$  is the typical transverse displacement,  $h^*$  the typical thickness (or slit thickness) and  $\mathcal{H}$  the height of fall. We compare these forces to viscous forces  $\mu U/\mathcal{H}^2$ , using Jeffreys' number:

$$\text{Je} = \frac{\rho g \mathcal{H}^2}{\mu U}, \quad (1)$$

and the inverse capillary number:

$$1/\text{Ca} = \frac{\gamma}{\mu U}. \quad (2)$$

We assume that  $h^*$  and  $H^*$  are of the same order  $h \sim (\epsilon \mathcal{H})$  which means out of plane displacements are

small. As we are only interested in viscous fluids, we ignore inertial terms in the limit where the Reynolds number  $Re = \rho U \mathcal{H} / \mu$  is small.

We are in the case where both the Jeffreys  $Je$  and inverse capillary  $Ca^{-1}$  numbers are small; transverse forces should be considered of order  $\epsilon$ . The variables are made dimensionless and scaled with the small parameter  $\epsilon = h^* / \mathcal{H}$ , where  $U$  is the injection velocity at the top of the sheet:

$$\begin{aligned} h &= \epsilon \mathcal{H} h' & H &= \epsilon \mathcal{H} H' & t &= \frac{\mathcal{H}}{U} t' \\ x &= \mathcal{H} x' & y &= \mathcal{H} y' & z &= \epsilon \mathcal{H} z' \\ u_x &= U u'_x & u_y &= U u'_y \\ d_{\alpha\beta} &= \frac{U}{\mathcal{H}} d'_{\alpha\beta} & \dot{K}_{\alpha\beta} &= \frac{\epsilon U}{\mathcal{H}^2} \dot{K}'_{\alpha\beta} & \hat{\epsilon}_{\alpha\beta} &= \frac{1}{\mathcal{H}} \hat{\epsilon}'_{\alpha\beta} \\ N_{\alpha\beta} &= 2 \mu U \epsilon N'_{\alpha\beta} & M_{\alpha\beta} &= 1/6 \mu U \epsilon^4 \mathcal{H} M'_{\alpha\beta} \end{aligned}$$

With these scaling and dropping the prime notation in the following, the domain of study becomes  $x \in [-1, 0]$  and  $y \in [-\beta, \beta]$  (See figure 1).

## 2.2. Kinematics

When searching for the base flow that establishes in the curtain in section 3, the two unknowns are the in-plane Eulerian velocities  $(u_x, u_y)$ . This base solution should be planar and stationary. The global buckling modes of this base solution are obtained in section 4 with the Eulerian out of plane deflection of the sheet's centre surface,  $H(x, y)$  as the unknown. The following derivation of the equations of equilibrium of a thin viscous sheet are obtained by adopting an Eulerian framework for in plane velocities and the out of plane displacement. This approximation relies on Jeffrey's number being small, and as the effect of gravity is small velocities can be linearised around the vertical advection speed  $U$ . The out of plane displacement remains of the order of the thickness in our study. We will first consider the advection of a small material segment  $d\mathbf{l} = (dx, dy, dz)$ . We must consider total derivatives in time, adopting the Eulerian specification of flow fields. Evaluating the deformation of the small material segment, in the in-plane coordinates  $x$  and  $y$ :

$$\frac{Ddx_\alpha}{Dt} = u_{\alpha,\beta} dx_\beta \quad (3)$$

In the out of plane direction  $z$ , the displacement of the sheet's centre surface  $H(x, y, t)$  is considered small, see section 2.1. In that limit, the projection of the material element  $dz$  can be linearly approximated as  $dz \approx H_{,\alpha} dx_\alpha$ . The deformation of the third component of the small material segment is:

$$\frac{Ddz}{Dt} = (H_{,\alpha t} + u_\gamma H_{,\gamma\alpha}) dx_\alpha + H_{,\gamma} (u_{\gamma,\alpha} dx_\alpha) \quad (4)$$

To obtain the stretching strain rate tensor  $\underline{d}$ , we apply it to the linear material element:

$$\underline{d\mathbf{l}} \cdot \underline{d\mathbf{l}} = \underline{d\mathbf{l}} \cdot (d_{ij} e_i \otimes e_j) \cdot \underline{d\mathbf{l}} = d_{ij} dx_i dx_j \quad (5)$$

And identify this expression with:

$$\begin{aligned} \frac{1}{2} \frac{Dd\mathbf{l}^2}{Dt} &= d_{ij} dx_i dx_j \\ &= dx_\alpha \frac{Ddx_\alpha}{Dt} + dz \frac{Ddz}{Dt} \\ &= dx_\alpha u_{\alpha,\beta} dx_\beta \\ &\quad + H_{,\alpha} dx_\alpha (H_{,\beta t} + u_\gamma H_{,\gamma\beta} + H_{,\gamma} u_{\gamma,\beta}) dx_\beta \end{aligned} \quad (6)$$

Which leads us to the expression of the components of the effectively 2D stretching strain rate tensor  $\underline{d}$ :

$$d_{\alpha\beta} = u_{(\alpha,\beta)} + H_{,(\alpha} H_{,\beta)t} + u_\gamma H_{,(\alpha} H_{,\beta)\gamma} + u_{\gamma,(\alpha} H_{,\beta)} H_{,\gamma} \quad (7)$$

Where parenthesis denote symmetrization of enclosed indices. To obtain the bending strain rate tensor  $\underline{\dot{K}}$ , we derive the expression of the bending strain tensor's components. For a nearly flat sheet, the bending strains are equal to the curvature, and thus  $K_{\alpha\beta} = H_{,\alpha\beta}$ . Considering the total derivative, one can write the bending strain rate tensor in components:

$$\dot{K}_{\alpha\beta} = \frac{D(H_{,\alpha\beta})}{Dt} = H_{,\alpha\beta t} + u_\gamma H_{,\alpha\beta\gamma} \quad (8)$$

## 2.3. Constitutive relations for viscous sheets

In the case of a viscous flow where inertia is negligible, the Stokes-Rayleigh analogy [?] can be used to obtain an equivalent linear elasticity formulation. Laminar viscous flows and linear elasticity have identical constitutive relations given a few modifications [?]. Elastic displacements are analogous to the viscous flow velocities, strains are changed into strain rates and elastic moduli are replaced with viscous moduli. Linear constitutive relations for the viscous fluid sheet can be written in the form:

$$N_{\alpha\beta} = 2 (d_{\alpha\beta} + \delta_{\alpha\beta} d_{\gamma\gamma}) \quad (9)$$

$$M_{\alpha\beta} = \frac{1}{6} (\dot{K}_{\alpha\beta} + \delta_{\alpha\beta} \dot{K}_{\gamma\gamma}) \quad (10)$$

With  $\underline{\delta}$  the Kronecker delta,  $\underline{N}$  the membrane stress tensor and  $\underline{M}$  the bending stress tensor.

## 2.4. Boundary conditions applied on the falling film

The viscous curtain is falling in an open medium, of negligible friction, hence it is considered stress free on its side. This means stresses will go to zero, and bending momenta will balance. These boundary conditions are naturally enforced in the numerical implementation.

The bottom of the curtain falls in a bath of the same liquid. In the stationary regime we study we expect it to reach the surface with a velocity comprising only a vertical component. At  $x = 0$ ,  $u_y = 0$ . The liquid bath will permit movements at the bottom of the curtain, we impose no kinematic boundary conditions and keep natural ones for the out of plane deflection  $H$ .

The problem has an axis of symmetry for the in-plane velocities at  $y = 0$ , and out of plane displacements are either symmetric or antisymmetric in each half of the curtain.

The presence of an injector at the top prescribes a purely vertical speed,  $u_x = U$  and  $u_y = 0$  on the  $x = -1$  border. This injector also prescribes specific boundary conditions for the out of plane displacement.

Injecting some liquid at speed  $U$  at the top of the curtain constrains the out of plane displacement. Exiting the injector, the sheet stays flat and we have  $H = 0$  and  $H_{,x} = 0$ . The presence of an advective term changes a lot the structure of the equations, and setting  $U \neq 0$  implies that we take into account total derivatives. In other words, when the injection speed is non zero, our equations gain one order in space derivatives and we need to introduce an additional boundary condition. This boundary condition necessarily appears at the injector, and derives from previously imposed conditions. Since  $H$  and  $H_{,x}$  are identically zero, even in the situation where  $U = 0$ , one can write  $\frac{dH}{dt} = 0$  and  $\frac{dH_{,x}}{dt} = 0$ . When the advection speed becomes  $U \neq 0$ , these two equations become:

$$\begin{aligned}\frac{DH}{Dt} &= H_{,t} + U H_{,x} = 0 \\ \frac{DH_{,x}}{Dt} &= H_{,xt} + U H_{,xx} = 0\end{aligned}$$

Maintaining the two boundary conditions on  $H$  and  $H_{,x}$ , the second equation leads to  $H_{,xx} = 0$ , which is our additional boundary condition at  $x = 0$  when  $U \neq 0$ . This completes the set of kinematic boundary conditions on the displacement  $H$  and appears in table (1).

### 2.5. Equilibrium equations

By applying the principle of virtual work, we can derive an integral quantity to be minimized by the stationary viscous flow.

External and internal forces add contributions to the global energy of the curtain, which can be written in weak form as:

$$\int -N_{\alpha\beta} \hat{\epsilon}_{\alpha\beta} - \varepsilon^2 M_{\alpha\beta} \hat{w}_{,\alpha\beta} + \text{Je} \hat{u}_x - \frac{1}{\text{Ca}\varepsilon} \hat{\epsilon}_{\alpha\alpha} = 0 \quad (11)$$

With  $\hat{\epsilon}_{\alpha\beta} = \hat{u}_{(\alpha,\beta)} + H_{,(\alpha} \hat{w}_{,\beta)}$ , where  $\hat{u}_\alpha$  and  $\hat{w}$  are virtual displacements in the plane and out of plane directions, that will be used as unknowns in the numerical simulations.

Using integration by parts we recover the equations that derive from the equilibrium balance of forces. We obtain three equations, the first one corresponds to a vertical balance, that involves the effect of gravity on the extension of the sheet, equation (12a). The horizontal balance is a simple equilibrium condition (12b). The third equation we obtain (12c) is an out of plane equilibrium that involves stresses in the sheet, leading to buckling that must fight

capillary forces.

$$N_{x\beta,\beta} + \text{Je} = 0 \quad (12a)$$

$$N_{y\beta,\beta} = 0 \quad (12b)$$

$$(N_{\alpha\beta} H_{,\alpha})_{,\beta} - \varepsilon^2 M_{\alpha\beta,\alpha\beta} + \frac{1}{\text{Ca}\varepsilon} H_{,\alpha\alpha} = 0 \quad (12c)$$

Obtaining these equations requires integrating by parts the weak form (11) assuming kinematic boundary conditions. During the process of integration by parts, boundary terms that appear are either cancelled by the kinematic boundary conditions, or must be retained as additional equations to be solved simultaneously, these are called the natural boundary conditions (see table 1).

## 3. Steady planar base solution

In this section, we derive the velocity field that develops in the falling viscous curtain. We consider the sheet to remain flat, and will consider the corresponding stationary flow. This steady planar flow will be used in section 4 as the base solution of a stability analysis. We will see at the end of this section why this planar flow may be unstable with respect to out-of-plane displacements.

### 3.1. Stresses in the plane flow

We study the flow that develops in the vertically flowing curtain. We want to obtain the velocity field, and we solve for  $u_x$  and  $u_y$  in half of the curtain, considering its symmetry with respect to the vertical x-axis. The velocities obey the kinematic equations (12a) and (12b) that involve the effect of gravity.

The stretching tensor  $N_{\alpha\beta}$  and the velocities are related by the constitutive relations (9).

Boundary conditions are described in table 1, the x-axis being an axis of symmetry.

The equation we solve numerically is obtained by setting  $H(x, y, t) = 0$  and its corresponding virtual displacement  $\hat{w} = 0$  in equation (11). We also neglect the effect of capillarity in the following, by setting  $\text{Ca}^{-1} = 0$ . Its small influence will be restored and analysed in the concluding part number 5 of this article.

As mentioned earlier, the effect of gravity is considered small, this means that Jeffrey's number  $\text{Je}$  (which compares the strength of gravity with viscous forces) is considered small. The curtain is injected at speed  $U$ , and we study a linear response to the small effects of gravity's pull measured by  $\text{Je}$ . Practically, modifications to the velocities in the curtain will be of order 1 in the parameter  $\text{Je}$ . This also means that horizontal velocities are small and that the curtain can be considered to remain a rectangle during its fall. We thus transform an a priori variable geometry with open edges in a linearised rectangular domain. The deformation due to horizontal velocities is evaluated in paragraph 3.2 and verified to be very small.

	base solution		stability analysis	
	kinematic	natural	kinematic	natural
free lateral edges		$N_{xy} = 0$ $N_{yy} + \frac{1}{Ca\varepsilon} = 0$		$-N_{xy} H_{,x} - 2 N_{yy} H_{,y}$ $+\varepsilon M_{yx,x} + \varepsilon M_{yy,y}$ $-\frac{1}{Ca\varepsilon} H_{,y} = 0$ $-\varepsilon M_{xy} = 0$ $-\varepsilon M_{yy} = 0$
top (injection)	$u_x = U$ $u_y = 0$		$H = 0$ $H_{,x} = 0$ $H_{,xx} = 0$	
bottom	$u_y = 0$	$N_{xx} = 0$		$-2 N_{xx} H_{,x} - N_{yx} H_{,y}$ $+\varepsilon M_{xx,x} + \varepsilon M_{xy,y}$ $-\frac{1}{Ca\varepsilon} H_{,x} = 0$ $-\varepsilon M_{xx} = 0$ $-\varepsilon M_{yx} = 0$
centreline (axis of symmetry)	$u_y = 0$	$N_{xy} = 0$	$* \begin{cases} H_{,y} = 0 \\ H = 0 \end{cases}$	$-N_{xy} H_{,x} - 2 N_{yy} H_{,y}$ $+\varepsilon M_{yx,x} + \varepsilon M_{yy,y}$ $-\frac{1}{Ca\varepsilon} H_{,y} = 0$ $-\varepsilon M_{xy} = 0$

Table 1: Boundary conditions for half of the curtain. The base solution being symmetric with respect to the  $x$  axis, numerics solve for half of the curtain. Additional boundary conditions due to the centreline are given in the last row. The stability analysis is also solved for a half curtain, with centreline kinematic boundary conditions on the displacement  $H$  (indicated by a  $*$ ) corresponding to the symmetric and anti-symmetric cases respectively.

We introduce a notation for the quantities implied in the base solution as perturbations of order  $Je$ :

$$N_{\alpha\beta}^{(0)} = Je \bar{N}_{\alpha\beta}^{(0)}$$

$$u_{\alpha}^{(0)} = U \delta_{\alpha x} + Je \bar{u}_{\alpha}^{(0)}$$

The equations for the velocities  $u_x^{(0)}$  and  $u_y^{(0)}$  in the flow are exactly analogous to the equations depicting an elastic plate under applied load in the direction  $x$ . This kind of problem is often solved by fitting series coefficients, accounting for stresses and boundary conditions. This method of resolution can be impractical if boundary conditions are hard to satisfy and can converge slowly. We prefer a finite element solver that will be used to obtain the results presented throughout this paper. We implement a 2D linear finite elements scheme to solve this standard linear elasticity problem. We will obtain the analogue of the displacement field, i.e. the velocities everywhere in the flow. We solve the equation in weak form  $\int -N_{\alpha\beta}^{(0)} \hat{u}_{(\alpha,\beta)} + Je \hat{u}_x = 0$  that can be written after dividing by  $Je$ :

$$\int -\bar{N}_{\alpha\beta}^{(0)} \hat{u}_{(\alpha,\beta)} + \hat{u}_x = 0 \quad (13)$$

with  $\bar{N}_{\alpha\beta}^{(0)} = 2(\bar{u}_{(\alpha,\beta)}^{(0)} + \delta_{\alpha\beta} \bar{u}_{\gamma,\gamma}^{(0)})$  and boundary conditions from table 1.

### 3.2. Reconstruction of particle trajectories

We have assumed that the thickness of the viscous sheet remains constant over the length of the fall. As we have just seen, volume elements are compressed in the

horizontal direction as they stretch along the vertical axis. Conservation of volume requires that both the width and the thickness of the curtain actually shrink. In order to evaluate the amount of deformation that is induced, and the validity of our assumptions, we use the incompressibility equation to obtain the shape of the edges.

$$\frac{dy}{dx} = -\frac{u_y(x, \beta)}{u_x(x, \beta)} \approx -\frac{u_y(x, \beta)}{U} \quad (14)$$

By integrating this differential relation along the height of the curtain, we can obtain the deformation of the sheet, as shown in figure 2. As the effect of gravity is small compared to the advective term, the ratio  $\frac{u_y}{U}$  is small, and of the order of the Jeffrey's number. Hence the shrinking effect is small in both the width and the thickness of the curtain, which can be considered constant along the height of the fall.

### 3.3. Compressive stresses

We have just seen that the steady planar flow appearing in the viscous curtain tends to shrink the curtain.

By analogy with an elastic problem, and since the equations describing the flow are strongly similar to the ones describing a stretched elastic sheet, we can explain the presence of these compressive strains by a Poisson's effect. When stretched, an elastic sheet with positive Poisson's ratio will also compress in the two directions orthogonal to the imposed displacement.

The equation we solve represents the balance of gravity and stretching stresses in the curtain. Upon accelerating downwards, an horizontal velocity also develops in

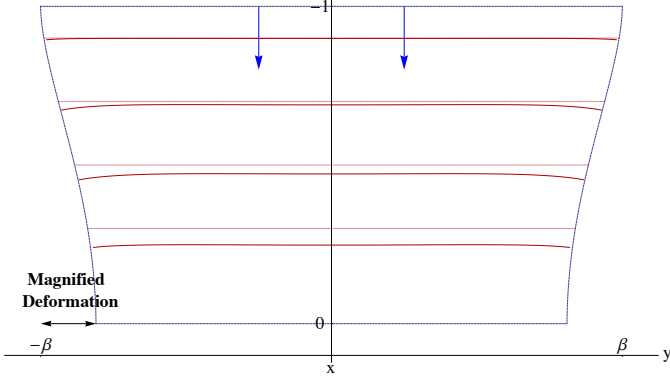


Figure 2: Shrinking of the curtain due to incompressibility. As velocities that develop in the horizontal direction are small, the overall deformation of the sheet is small. This is also true for the thickness. Lateral deformations are magnified five times. Lines in the flow represent particles that were injected at the same time.

the curtain, directed towards its centreline. Considering a fluid element, it is being stretched vertically, and through an analogous Poisson's effect it will preserve its volume by contracting sideways. As a consequence, fluid particles are driven closer to each other and lead to a compressed state.

In order to visualize where the curtain is under compressive stresses, we plot the smallest eigenvalue of the local stress tensor on a colour map. We denote the ordered principal stresses of tensor  $N_{\alpha\beta}$  by  $N_I$  and  $N_{II}$  with  $N_I < N_{II}$ , such that  $\det(\underline{N} - \lambda \underline{I}) \propto (\lambda - N_I)(\lambda - N_{II})$ . Red zones of figure 3 represent compressed zones where  $N_I < 0$ , while blue colour indicates a stretched state ( $N_I > 0$ ). In the red zone, the viscous sheet is stretched vertically, but compressed in the horizontal direction. In the blue zone, it is stretched in both directions. Obtaining figure 3 presents some difficulties since convergence is difficult in the top corners, where the injection device ends. The numerical implementation requires the use of adaptive mesh refinement in order to selectively refine the mesh where convergence is difficult. For a curtain of aspect ratio  $\beta = 0.4$  and a mesh refined 5 times, we obtain a mesh of around  $10^4$  elements. It has been mentioned previously that these kind of problems are often approached analytically by using series convergence. In this problem, the refinements requirements are important and series convergence requires an homogeneous grid, which leads to very long calculations. The adaptive mesh refinement available in the finite elements method doesn't face this limitation.

As displayed in figure 3, stresses in the vertical  $x$  direction are always stretching, while compressive stresses appear in the horizontal  $y$  direction. Compressive stresses in thin structures are sources of instability, and if the curtain is thin enough the coupling between stretching and bending tensors should lead to buckling. By pursuing the elastic analogy, this mechanical buckling phenomenon should be displayed by a thin elastic sheet. It is indeed the case and

was experimentally revealed by Cerda et al. [5].

#### 4. Linear stability analysis and numerical implementation

In the previous section, we have obtained the velocity field that develops in the case of a steady planar flow. This planar solution may be unstable with respect to perturbations in the velocities, and in the out of plane displacement of the curtain. We will derive the linearly perturbed equations of the curtain in this section, and obtain an out-of-plane equilibrium that will be solved numerically.

##### 4.1. Linear perturbations

We will perturb equation (11) by adding increments of the quantities  $u_x$ ,  $u_y$  and  $H$ . These linear perturbations can be written  $u_x = u_x^{(0)} + u_x^{(1)}$ , where  $^{(0)}$  denotes the base solution, and  $^{(1)}$  first order perturbations. We will not perturb the equation with respect to the quantity  $h$  since it is already a small quantity, and its perturbation would be of higher order than one. In the same line of ideas, first order perturbation means that we do not need to consider advection by the complete velocity field  $(u_x^{(0)}, u_y^{(0)})$  we computed but only by the vertical advection speed  $U$ , since the complete field is a small perturbation of it.

The perturbed weak form (11) becomes:

$$\int N_{\alpha\beta}^{(1)} \hat{\epsilon}_{\alpha\beta}^{(0)} + N_{\alpha\beta}^{(0)} \hat{\epsilon}_{\alpha\beta}^{(1)} + \varepsilon^2 M_{\alpha\beta}^{(1)} \hat{w}_{,\alpha\beta} = 0 \quad (15)$$

In this equation  $N_{\alpha\beta}^{(1)}$  depends only on the tensor  $d_{\alpha\beta}$  linearised to first order which becomes  $d_{\alpha\beta}^{(1)} = u_{(\alpha,\beta)}^{(1)}$ . Similarly,  $M_{\alpha\beta}^{(1)}$  depends on the tensor  $\dot{K}_{\alpha\beta}^{(1)} = H_{,\alpha\beta t}^{(1)} + u_{\gamma}^{(0)} H_{,\alpha\beta\gamma}^{(1)}$  which is equal to  $H_{,\alpha\beta t}^{(1)} + U H_{,\alpha\beta x}^{(1)}$  when we retain only first order terms. The virtual displacements become  $\epsilon_{\alpha\beta}^{(0)} = \hat{u}_{\alpha,\beta}$  and  $\epsilon_{\alpha\beta}^{(1)} = H_{,\alpha}^{(1)} \hat{w}_{,\beta}$ .

Equation 15 can then be rewritten as:

$$\begin{aligned} & \int 2(u_{(\alpha,\beta)}^{(1)} + \delta_{\alpha\beta} u_{(\gamma,\gamma)}^{(1)}) \hat{u}_{\alpha,\beta} \\ & + N_{\alpha\beta}^{(0)} H_{,\alpha}^{(1)} \hat{w}_{,\beta} \\ & + \frac{\varepsilon^2}{6} \left( H_{,\alpha\beta t}^{(1)} + U H_{,\alpha\beta x}^{(1)} + \delta_{\alpha\beta} (H_{,\gamma\gamma t}^{(1)} + U H_{,\gamma\gamma x}^{(1)}) \right) \hat{w}_{,\alpha\beta} = 0 \end{aligned}$$

This weak form can quickly be identified as the sum of two uncoupled problems on the independent virtual displacements  $\hat{u}$  and  $\hat{w}$ . The first term is the only one to involve perturbations in the velocities, it corresponds to a planar homogeneous elastic perturbation. This is necessarily solved by the null solution  $u_{\alpha}^{(1)} = 0$ .

The only perturbed quantity that leads to a non trivial problem is  $H^{(1)}$  and we can write  $H^{(1)} = \hat{H}(x, y) e^{-i\omega t}$  as a description of the perturbed modes. By keeping the other two terms of the equation we obtain an out-of-plane



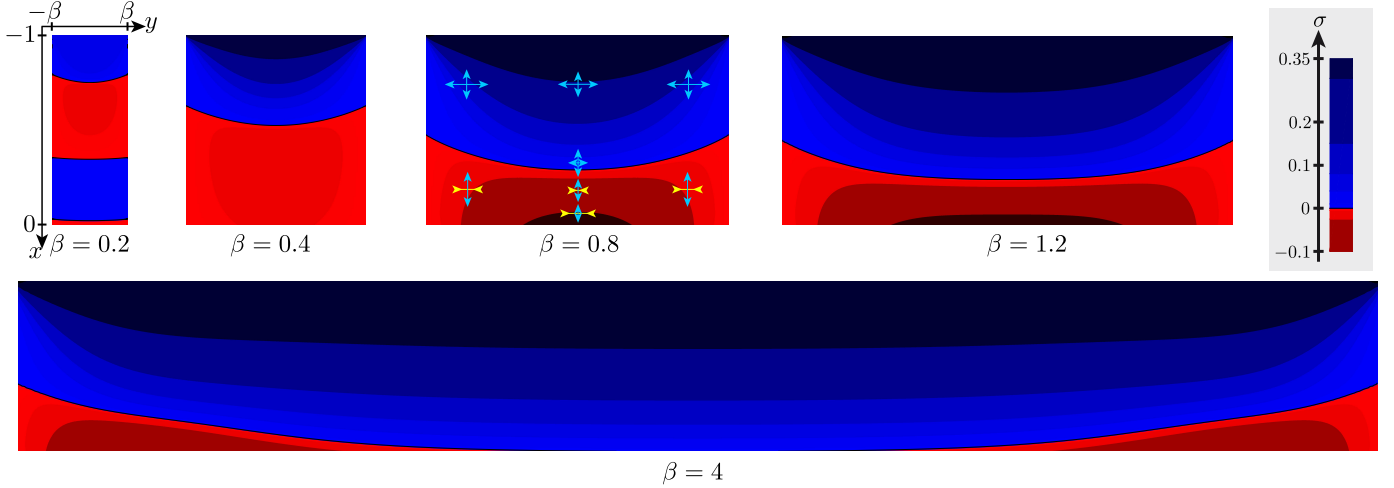


Figure 3: Visualization of the most negative eigenvalue (denoted by  $N_I$  in section 3.3) of the local stress tensor  $N_{\alpha\beta}$ , for different aspect ratios  $\beta$ . Red zones are under compression, while blue zones are stretched. These images are made adopting the Lagrangian framework, actual shape of the curtain isn't visible.

equilibrium, balancing the stretched planar configuration of the curtain with out-of-plane movements that involve bending effects.

We will refer to the constitutive relation (10) as  $M_{\alpha\beta} = L_{\alpha\beta\sigma\tau} \dot{K}_{\sigma\tau}$  where  $L_{\alpha\beta\sigma\tau} = \frac{1}{6}(\delta_{\alpha\sigma} \delta_{\beta\tau} + \delta_{\alpha\beta}(\delta_{\gamma\sigma} \delta_{\gamma\tau}))$ . By inserting the decomposed form of  $H^{(1)}$  we obtain an eigenvalue problem:

$$\bar{N}_{\alpha\beta}^{(0)} \tilde{H}_{,\alpha} \hat{w}_{,\beta} + \frac{\varepsilon^2 U}{\text{Je}} L_{\alpha\beta\sigma\tau} \tilde{H}_{,\sigma\tau x} \hat{w}_{,\alpha\beta} = i \frac{\omega}{\text{Je}} L_{\alpha\beta\sigma\tau} \tilde{H}_{,\sigma\tau} \hat{w}_{,\alpha\beta} \quad (16)$$

In this equation  $\bar{N}_{\alpha\beta}^{(0)}$  denotes the stretching stress tensor computed with  $\text{Je} = 1$ , and the scaling in  $\text{Je}$  is explicitly denoted. This equation defines an eigenvalue problem that will be solved numerically, in the next section we will detail how its implementation can be done.

#### 4.2. High order elements

One may notice that the weak form of the out-of-plane problem involves third order derivatives, that are due to advective terms. These terms turn into fifth order derivatives when developed into their strong form, meaning that standard numerical implementation is not possible.

By using  $C^1$  elements in our numerical scheme, we could solve equations involving second order derivatives on both the test and trial functions. This translates into fourth order derivatives when written out in strong form. In order to take into account a third order derivative of the test function, we will use an idea inspired by the discontinuous Galerkin method, as described in [28].

The main idea we extract from the discontinuous Galerkin method is to assign each derivation order to a different variable. By defining a new variable and constraining it to the first derivative of another, its first derivative becomes the second order derivative of the original variable. A  $C^0$  finite element scheme gives access to first order derivatives.

By adding an independent variable to the problem, and one constraint equation to solve, we can gain one derivative order in the main equation. With a  $C^1$  finite elements scheme, fewer variables are required, but the process is exactly the same. By adding new variables and one constraint equation for each variable, one can gain derivation orders.

The drawback is that each new constraint equation also introduces a penalty parameter, that cannot be quantified a priori. In the numerical scheme we use, only one penalty parameter is introduced and has to be adjusted.

#### 4.3. Generalized eigenvalue problem

The equation we obtained describes time dependent modes. In order to obtain the most unstable mode, we will solve an eigenvalue problem, written in compact form:

$$A(\beta, \frac{\varepsilon^2 U}{\text{Je}}) \tilde{H} = \frac{i\omega}{\text{Je}} B \tilde{H} \quad (17)$$

This very simplified form is obtained after the finite elements method's discretization process is applied to the variable  $\tilde{H}$ . In the finite elements scheme  $\tilde{H}$  is evaluated with trial functions and  $\hat{w}$  using the test functions. When this process is over, the equivalent algebraic problem involves finding the large vector  $\tilde{H}$  given the matrices  $A$  and  $B$ .  $A$  contains all the time independent terms of the equation written as an operator applied on the vector  $\tilde{H}$ , while  $B$  contains the time dependent terms.

The most unstable mode is given by the highest growth rate  $\text{Im}(\omega)$ . The corresponding eigenvector is depicted in figure 4. One can notice that the eigenmodes are of growing amplitude in the locally compressed zone, which indicates a good correlation between the local analysis of section 3 and the global analysis presented now.

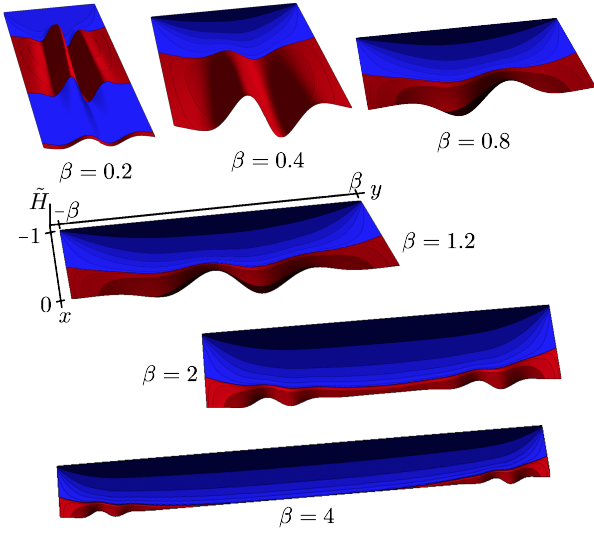


Figure 4: Shape of the most unstable buckling mode of the curtain for various aspect ratios. Growth rates of these mode become positive when the thickness  $\epsilon$  is small enough. Here we chose growth rates slightly positive. For the thickness values see the phase diagram of figure 5

By analogy with a buckling experiment, one would expect the most unstable mode to have the longest wavelength possible within the width of the system. This is not the case, and for all aspect ratios several wavelengths span the width of the curtain. This phenomenon is thus closer to wrinkling than buckling, which means that stretching and bending both play an important role and are in competition. The shape of the eigenmodes we obtained are very close to the numerical predictions available for the analogous elastic problem described earlier [? ].

The numerical resolution of an eigenvalue problem returns a large number of eigenmodes, equal to the dimension of the matrix. In order to identify physical modes, that correspond to smooth solutions to the equation, we need to stand far enough of the threshold. Grid modes are densely packed with close to zero eigenvalues and make the detection of zero crossing modes difficult near the threshold. Nonetheless, corresponding eigenmodes are very easy to discriminate due to their highly jagged aspect.

#### 4.4. Phase diagram

The growth rate of the eigenmodes represented in figure 4 becomes positive only if the curtain is thin enough. This instability threshold on the thickness depends on the aspect ratio of the viscous sheet, and we can plot a phase diagram in the space  $(\beta, \frac{\epsilon^2}{Je})$ .

The most unstable aspect ratio is around  $\beta = 1$ , a curtain twice as large as it is high. We obtain purely imaginary growth rates for  $\beta < \beta^*$ , the corresponding unstable mode will grow or be dampened depending on the sign of

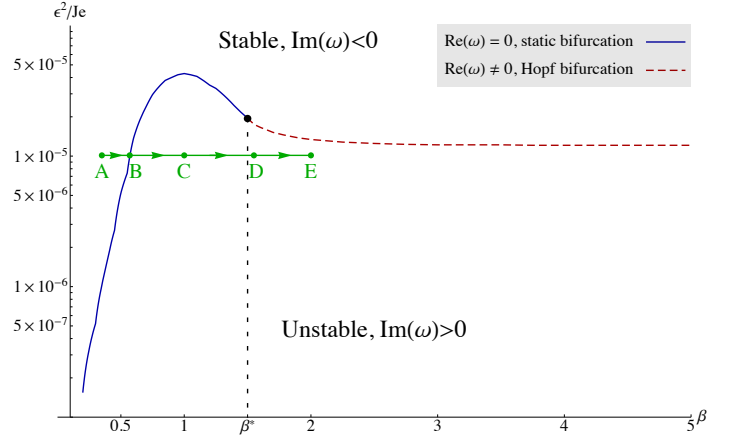


Figure 5: Instability threshold for the thickness squared as a function of the aspect ratio. The blue line indicates a purely imaginary growth rate while the dashed red line indicates a growth rate with non zero real part. The green path going from A to E is used to track the evolution of the growth rate in figure 6.  $\beta^*$  is the aspect ratio separating modes with zero and non zero real parts, which correspond to oscillatory modes.

$\text{Im}(\omega)$ . Growth rates with a non zero real part indicate an oscillatory mode of growing amplitude. The position of the aspect ratio  $\beta^*$  depends on the value chosen for Jeffrey's number and separates two types of bifurcations. A pitchfork bifurcation will lead to purely imaginary growth rate, while a Hopf bifurcation leads to the oscillatory modes with non zero real part.

Travelling along a path of constant thickness A→E indicated on figure 5, we expect the eigenvalues to reach positive values when crossing the instability threshold at point B. We expect a maximum of the eigenvalue's imaginary part at point C, at a non zero real to appear upon crossing of point D. The eigenvalues of the most unstable mode are represented on figure 6 as we move along the previously described path A→E.

## 5. Capillarity

When deriving the numerical solutions of our equations in section 3, we neglected the effects of capillarity by setting  $Ca = \infty$ . We now restore the effects of capillarity and show that its influence is stabilizing, but does not change the qualitative behaviour of our system.

### 5.1. Stabilizing effect

Capillary action tends to minimize the surface occupied by a liquid. While its effect is small, especially in a very viscous liquid, it tends to reduce the section of the curtain and will lead to a faster reduction of its width. The thickness of the viscous sheet is expected to increase under this effect. In terms of out of plane deflection, the capillary term in the equations is proportional to the surface of the sheet, which means it will prevent the occurrence of

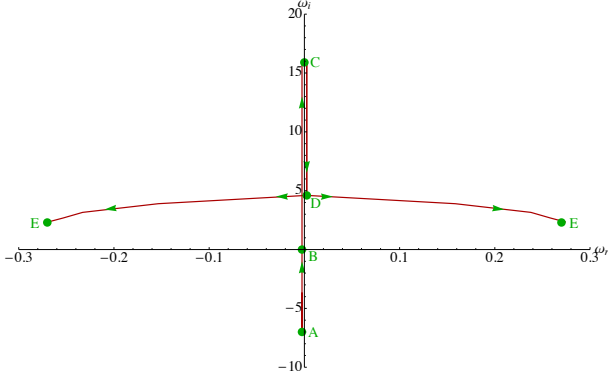


Figure 6: Motion of the growth rate of the most unstable eigenmode in the complex plane, as we follow the path from A to E in the phase diagram of figure 5. B is the frontier between stable and unstable aspect ratios for the chosen thickness  $\varepsilon^2 = 10^{-5}$ . C corresponds to the most unstable aspect ratio, and D marks the frontier between the fixed and oscillatory eigenmodes.

buckling. By following these two qualitative guesses, we expect the base flow to not change much when capillary effects are restored, while we expect the non-linear buckling to happen for thinner sheets, increasing the buckling threshold.

### 5.2. Equations including capillarity

Taking capillary effects into account will not affect the method used, as it only consists in restoring the term involving  $Ca$  in our equations. In section 3 the important equation is the weak form presented in equation (13). When considering a non-zero Capillary number this equation becomes:

$$\int -N_{\alpha\beta} \hat{\epsilon}_{\alpha\beta} + Je \hat{u}_x - \frac{1}{Ca \varepsilon} \hat{u}_{\alpha,\alpha} = 0 \quad (18)$$

As mentioned earlier, this term only has a small influence on the base flow that develops in the curtain. For a chosen aspect ratio, we can compare the local stress maps with and without capillary forces. We can observe on figure 8

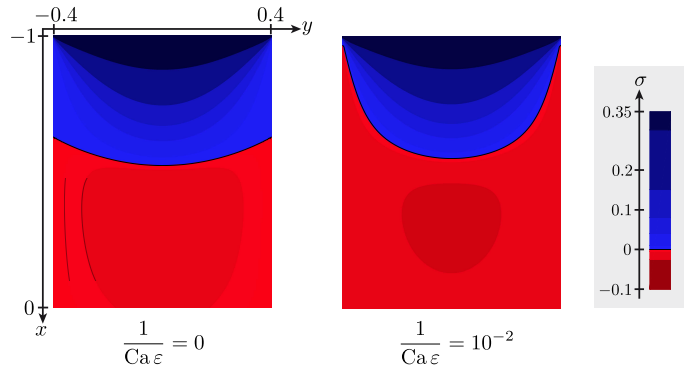


Figure 7: Local stress maps for aspect ratio  $\beta = 0.4$  with no capillary effect (left) and restored capillary number  $Ca$  (right).

that the effect of capillary effects are mostly visible on the sides of the curtain. As capillary forces tend to reduce the width of the curtain, compressive stresses are present earlier near the edges of the curtain. However, the overall stress map is mainly unchanged.

Additional modifications due to capillary strains appear when studying the stability of the curtain. Indeed, we also have to restore a term in the weak form governing the out of plane equilibrium (15):

$$\int N_{\alpha\beta}^{(1)} \hat{\epsilon}_{\alpha\beta}^{(0)} + N_{\alpha\beta}^{(0)} \hat{\epsilon}_{\alpha\beta}^{(1)} + \varepsilon^2 M_{\alpha\beta}^{(1)} \hat{w}_{,\alpha\beta} - \frac{1}{Ca \varepsilon} \hat{\epsilon}_{\alpha\alpha}^{(1)} = 0 \quad (19)$$

Similarly to the previous situation, we have two uncoupled problems to solve. One for the virtual velocities  $\hat{u}_x$  and  $\hat{u}_y$ , the other for the virtual displacement  $\hat{w}$ . Following the exact same argument, the first problem has a null solution, while the second one leads to solutions with non zero out of plane displacements. Boundary conditions are unchanged, and were already exposed with their full dependence in the parameter  $Ca$ . Numerical implementation follows the same method as described earlier.

### 5.3. Stabilized phase diagram

In order to see the stabilizing effect due to capillary strains, we computed an updated phase diagram taking into account a parameter  $\frac{1}{Ca \varepsilon Je} = 0.01$ .

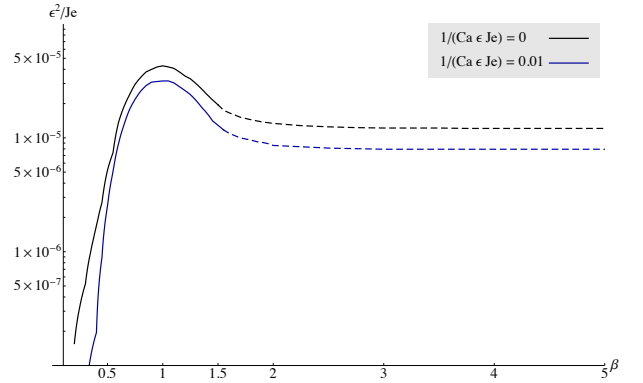


Figure 8: Movement of the instability threshold in the phase diagram when restoring capillary forces.

## 6. Conclusion

We considered a vertical sheet made up of a viscous fluid and falling into a bath. This curtain is formed by an inlet injecting viscous fluid at the top of the domain and creating an open flow. The resulting thin structure is falling under the effect of gravity, and has been seen to develop regions of compressive stress. Those can engender a mechanical instability in the structure as the sheet can buckle under compression, losing its planar geometry and deforming in the out-of-plane direction. We used a viscous

membrane model, inspired by the solid mechanics of thin structures it uses the Stokes-Rayleigh analogy to transpose the concepts of stretching and bending stress to a viscous problem. By using the principle of virtual work, we could derive the equations of the two-dimensional flow developing in the sheet under the effect of gravity. By imposing boundary conditions corresponding to the advection velocity at the top boundary and to free stress on other edges, we obtained the two-dimensional flow that develops in the viscous curtain as it falls down under the effect of gravity. Using this velocity field, we visualized the values of the local stress rate tensor and obtained the map of pre-stress in the curtain. After obtaining those stress maps we expect the thin structure to be unstable and to buckle if it is thin enough. Buckling of a viscous layer has already been an active subject of research, but it was only observed in configurations featuring a direction of invariance. The buckling of a viscous membrane subjected to a fully two-dimensional pre-stress with only one axis of symmetry was a new development. In order to obtain the equations for the out-of-plane equilibrium we used once again the principle of virtual work and studied the appearance of a deflection. As we study an open flow, this derivation must take into account the fact that material elements are being advected at a prescribed velocity, and we used comoving derivatives. The resulting equations feature a fifth order spatial derivative, making numerical implementation more difficult. Because the buckling instability involves a fluid thin structure, we also considered capillary effects. They tend to reduce the surface of the interfaces of a liquid system, and are observed to stabilize the curtain as they limit its out-of-plane deflections. Because of the unexpected appearance of buckling modes of shorter wavelength than the fundamental mode, we suspect that this wavelength is related to a characteristic length scale present in the stress map.

## References

- [1] George Barnes. Liquid Rope-Coil Effect. *American Journal of Physics*, 26(4):205, 1958.
- [2] T. Brooke Benjamin and T. Mullin. Buckling instabilities in layers of viscous liquid subjected to shearing. *Journal of Fluid Mechanics*, 195(-1):523, April 1988.
- [3] S. Bhattacharya, R. V. Craster, and M. R. Flynn. Buckling of a thin, viscous film in an axisymmetric geometry. *Physics of Fluids*, 25(4):043102, 2013.
- [4] A Boudaoud and S Chaieb. Singular thin viscous sheet. *PHYSICAL REVIEW-SERIES E*, 64(5):50601, 2001.
- [5] E Cerda, K Ravi-Chandar, and L Mahadevan. Thin films: Wrinkling of an elastic sheet under tension. *Nature*, 419(6907):579–580, 2002.
- [6] Rava da Silveira, Sahraoui Chaieb, and L. Mahadevan. Rippling Instability of a Collapsing Bubble. page 11, August 2000.
- [7] G. Debrégeas. The Life and Death of "Bare" Viscous Bubbles. *Science*, 279(5357):1704–1707, March 1998.
- [8] SM Dockerty. sheet forming apparatus. *US Patent 3,338,696*, 1967.
- [9] F.D. Fischer, F.G. Rammerstorfer, N. Friedl, and W. Wieser. Buckling phenomena related to rolling and levelling of sheet metal. *International Journal of Mechanical Sciences*, 42(10):1887–1910, October 2000.
- [10] N Friedl, F.G Rammerstorfer, and F.D Fischer. Buckling of stretched strips. *Computers & Structures*, 78(1-3):185–190, November 2000.
- [11] RW Griffiths and JS Turner. Folding of viscous plumes impinging on a density or viscosity interface. *Geophysical Journal International*, 95(2):397–419, November 1988.
- [12] Tae-Yeon Kim, Eric Puntel, and Eliot Fried. Numerical study of the wrinkling of a stretched thin sheet. *International Journal of Solids and Structures*, 49(5):771–782, March 2012.
- [13] SP Lin. Stability of a viscous liquid curtain. *Journal of Fluid Mechanics*, 104:111–118, 1981.
- [14] SP Lin. Breakup of liquid sheets and jets. 2003.
- [15] SP Lin and G Roberts. Waves in a viscous liquid curtain. *Journal of Fluid Mechanics*, 112:443–458, 1981.
- [16] D.W. Lloyd, W.J. Shanahan, and M. Konopasek. The folding of heavy fabric sheets. *International Journal of ...*, 20(8):521–527, January 1978.
- [17] L. Mahadevan and Joseph B. Keller. Periodic Folding of Thin Sheets. *SIAM Review*, 41(1):115–131, January 1999.
- [18] EH Mansfield. Gravity-induced wrinkle lines in vertical membranes. *Proceedings of the Royal Society of ...*, 375(1762):307–325, 1981.
- [19] Vishal Nayyar, K. Ravi-Chandar, and Rui Huang. Stretch-induced stress patterns and wrinkles in hyperelastic thin sheets. *International Journal of Solids and Structures*, 48(25-26):3471–3483, December 2011.
- [20] Eric Puntel, Luca Deseri, and Eliot Fried. Wrinkling of a Stretched Thin Sheet. *Journal of Elasticity*, 105(1-2):137–170, 2011.
- [21] N. M. Ribe. A general theory for the dynamics of thin viscous sheets. *Journal of Fluid Mechanics*, 457(April 2002), April 2002.
- [22] Neil M. Ribe. All bent out of shape: buckling of sheared fluid layers. *Journal of Fluid Mechanics*, 694:1–4, February 2012.
- [23] M Skorobogatiy and L Mahadevan. Folding of viscous sheets and filaments. *EPL*, pages 532–538, 2000.
- [24] Shawqi M Suleiman and Bruce R Munson. Viscous buckling of thin fluid layers. *Physics of Fluids*, 24(1):1–5, 1981.
- [25] G Taylor, O Meteorology, and T Flow. The Scientific Papers of Sir geoffrey ingram taylor. *Mechanics of Solids*, ed. GK Batchelor, Cambridge ..., 1958.
- [26] B Tchavdarov. Buckling of thin liquid jets. *Journal of Fluid ...*, 253, 1993.
- [27] JA Teichman. Wrinkling and sagging of viscous sheets. 2002.
- [28] Yan Xu and Chi-Wang Shu. A Local Discontinuous Galerkin Method for the Camassa-Holm Equation, 2008.
- [29] Ling Zheng. Wrinkling of dielectric elastomer membranes. 2009, 2009.



# Bibliography

- [ABL09] Luisa Arlotti, Jacek Banasiak, and Bertrand Lods. A New Approach to Transport Equations Associated to a Regular Field: Trace Results and Well-posedness. Mediterranean Journal of Mathematics, 6(4):367–402, 2009.
- [AP10] B Audoly and Y Pomeau. Elasticity and Geometry: From hair curls to the nonlinear response of shells. Oxford University Press, USA, 2010.
- [Arn90] Douglas N. Arnold. Mixed finite element methods for elliptic problems. Computer Methods in Applied Mechanics and Engineering, 82(1-3):281–300, 1990.
- [ATB14] C. Albert, A. Tezuka, and D. Bothe. Global linear stability analysis of falling films with inlet and outlet. Journal of Fluid Mechanics, 745:444–486, March 2014.
- [BAA<sup>+</sup>14a] Satish Balay, Shrirang Abhyankar, Mark F. Adams, Jed Brown, Peter Brune, Kris Buschelman, Victor Eijkhout, William D. Gropp, Dinesh Kaushik, Matthew G Knepley, Lois Curfman McInnes, Karl Rupp, Barry F. Smith, and Hong Zhang. PETSc Web page, 2014.
- [BAA<sup>+</sup>14b] Satish Balay, Shrirang Abhyankar, Mark F. Adams, Jed Brown, Peter Brune, Kris Buschelman, Victor Eijkhout, William D. Gropp, Dinesh Kaushik, Matthew G. Knepley, Lois Curfman McInnes, Karl Rupp, Barry F. Smith, and Hong Zhang. PETSc Users Manual. Technical Report ANL-95/11 - Revision 3.3, Argonne National Laboratory, 2014.
- [Bar58] George Barnes. Liquid Rope-Coil Effect. American Journal of Physics, 26(4):205, 1958.
- [Bar06] D Barkley. Linear analysis of the cylinder wake mean flow. Europhysics Letters (EPL), 75(5):750–756, September 2006.
- [BB97] L. Brevdo and Thomas J. Bridges. Local and global instabilities of spatially developing flows: cautionary examples. Annual Review of Fluid Mechanics, 22:473–537, 1997.
- [Ber75] Abraham Bers. Linear Waves and Instabilities. In Plasma Physics - Les Houches Summer School, pages 117–215. 1975.
- [BF83] I B Bernstein and L Friedland. Handbook of Plasma Physics. MN Rosenbluth and RZ Sagdeev eds, 1(3.2):367–418, 1983.
- [BGMS97] Satish Balay, W. D. Gropp, L. C. McInnes, and B. F. Smith. Efficient management of parallelism in object-oriented numerical software libraries. Modern software tools in scientific computing, pages 163–202, 1997.

- [BHMM05] F Brezzi, T J R Hughes, L D Marini, and A Masud. Mixed discontinuous Galerkin methods for Darcy flow. Journal of Scientific Computing, 22(1):119–145, 2005.
- [Bio64] M A Biot. Theory of Viscous Buckling of Multilayered Fluids Undergoing Finite Strain. Physics of Fluids, 7(6):855, 1964.
- [BM88] T. Brooke Benjamin and T. Mullin. Buckling instabilities in layers of viscous liquid subjected to shearing. Journal of Fluid Mechanics, 195:523, April 1988.
- [BN78] J. D. Buckmaster and A. Nachman. The buckling and stretching of a viscida II. Effects of surface tension. The Quarterly Journal of Mechanics and Applied Mathematics, XXXI(2):157–168, 1978.
- [BNT75] J. D. Buckmaster, A. Nachman, and L. Ting. The buckling and stretching of a viscida. Journal of Fluid Mechanics, 69(1):1–20, 1975.
- [Bri64] Richard J Briggs. Electron-stream interaction with plasmas. Res. Mono. MIT, Cambridge, MA, 1964.
- [BS05] Susanne C Brenner and Li-Yeng Yeng Sung. C 0 interior penalty methods for fourth order elliptic boundary value problems on polygonal domains. Journal of Scientific Computing, 22-23:83–118, 2005.
- [BUAG12] Christopher Batty, Andres Uribe, Basile Audoly, and Eitan Grinspun. Discrete viscous sheets. ACM Transactions on Graphics, 31(4):1–7, 2012.
- [CFGB05] Y. Couder, E. Fort, C. H. Gautier, and a. Boudaoud. From bouncing to floating: Noncoalescence of drops on a fluid bath. Physical Review Letters, 94(17):1–4, 2005.
- [CGM<sup>+</sup>05] B Castaing, C Godrèche, P Manneville, B Castaing, C Godrèche, and P Manneville. Hydrodynamics and nonlinear instabilities. 2005.
- [Cho05] Jean-Marc Chomaz. GLOBAL INSTABILITIES IN SPATIALLY DEVELOPING FLOWS: Non-Normality and Nonlinearity. Annual Review of Fluid Mechanics, 37(1):357–392, January 2005.
- [CRCM02] E Cerda, K Ravi-Chandar, and L Mahadevan. Thin films: Wrinkling of an elastic sheet under tension. Nature, 419(6907):579–580, 2002.
- [DdL02a] Olivier Doaré and Emmanuel de Langre. Local and global instability of fluid-conveying pipes on elastic foundations. Journal of fluids and structures, 16(1):1–14, 2002.
- [DdL02b] Olivier Doaré and Emmanuel de Langre. The flow-induced instability of long hanging pipes. European Journal of Mechanics, A/Solids, 21(5):857–867, 2002.
- [DHCM96] Stephane Le Dizes, Patrick Huerre, Jean Marc Chomaz, and Peter A Monkewitz. Linear Global Modes in Spatially Developing Media. Philosophical Transactions of the Royal Society A: Mathematical, Physical and Engineering Sciences, 354(1705):169–212, 1996.

- [Doc67] Stuart M Dockerty. Sheet forming apparatus, 1967.
- [DRQKGD07] C. Duprat, C. Ruyer-Quil, S. Kalliadasis, and F. Giorgiutti-Dauphiné. Absolute and convective instabilities of a viscous film flowing down a vertical fiber. Physical Review Letters, 98(24):244502, June 2007.
- [EGH<sup>+</sup>02] G Engel, K Garikipati, T J R Hughes, M G Larson, L Mazzei, and R L Taylor. Continuous/discontinuous finite element approximations of fourth-order elliptic problems in structural and continuum mechanics with applications to thin beams and plates, and strain gradient elasticity. Computer Methods in Applied Mechanics and Engineering, 191(34):3669–3750, 2002.
- [FRF00] N Friedl, F.G G Rammerstorfer, and F.D D Fischer. Buckling of stretched strips. Computers & Structures, 78(1-3):185–190, November 2000.
- [FRFW00] F.D. D Fischer, F.G. G Rammerstorfer, N. Friedl, and W. Wieser. Buckling phenomena related to rolling and levelling of sheet metal. International Journal of Mechanical Sciences, 42(10):1887–1910, October 2000.
- [GT88] RW Griffiths and JS Turner. Folding of viscous plumes impinging on a density or viscosity interface. Geophysical Journal International, 95(2):397–419, November 1988.
- [HM85] P Huerre and PA A Monkewitz. Absolute and convective instabilities in free shear layers. Journal of Fluid Mechanics, pages 151–168, 1985.
- [How96] P. D. Howell. Models for thin viscous sheets. (1970):24–29, 1996.
- [HR06] Vincent Heuveline and Rolf Rannacher. Adaptive FEM for eigenvalue problems with application in hydrodynamic stability analysis. Journal of Numerical Mathematics, 0(0):1–32, 2006.
- [HRV05] Vicente Hernandez, Jose E Roman, and Vicente Vidal. SLEPc. ACM Transactions on Mathematical Software, 31(3):351–362, 2005.
- [Hue00] Patrick Huerre. Open Shear Flow Instabilities. In Perspectives in Fluid Dynamics, pages 159–229. Cambridge University Press, 2000.
- [Jef25] H. Jeffreys. LXXXIV. The flow of water in an inclined channel of rectangular section. Philosophical Magazine Series 6, 49(August 1913):793–807, 1925.
- [KBR87] Kenneth Kupfer, Abraham Bers, and A. K. Ram. The cusp map in the complex-frequency plane for absolute instabilities. Physics of Fluids, 30(10):3075, 1987.
- [KPF12] Tae-Yeon Yeon Kim, Eric Puntel, and Eliot Fried. Numerical study of the wrinkling of a stretched thin sheet. International Journal of Solids and Structures, 49(5):771–782, March 2012.



- [KPSC06] Benjamin S. Kirk, John W. Peterson, Roy H. Stogner, and Graham F. Carey. `\texttt{libMesh}`: A C++ Library for Parallel Adaptive Mesh Refinement/Coarsening Simulations. Engineering with Computers, 22(3–4):237–254, November 2006.
- [KSHW95] M. Khor, J. Sheridan, K. Hourigan, and M. Welsh. Characterisation of the instability in the near-wake of a circular cylinder. In Proceedings of the 12th Australasian Fluid Mechanics Conference, pages 33–36, 1995.
- [Lin81] S. P. Lin. Stability of a viscous liquid curtain. Journal of Fluid Mechanics, 104:111–118, 1981.
- [LLTS10] David Lo Jacono, Justin S. Leontini, Mark C. Thompson, and John Sheridan. Modification of three-dimensional transition in the wake of a rotationally oscillating cylinder. Journal of Fluid Mechanics, 643:349–362, 2010.
- [LR81] S. P. Lin and G Roberts. Waves in a viscous liquid curtain. Journal of Fluid Mechanics, 112:443–458, 1981.
- [LR04] S. P. Lin and K. J. Ruschak. Breakup of Liquid Sheets and Jets, volume 57. Cambridge University Press, 2004.
- [LSK78] D.W. Lloyd, W.J. Shanahan, and M. Konopasek. The folding of heavy fabric sheets. International Journal of Mechanical Sciences, 20(8):521–527, January 1978.
- [LTH10] J. S. Leontini, M. C. Thompson, and K. Hourigan. A numerical study of global frequency selection in the time-mean wake of a circular cylinder. Journal of Fluid Mechanics, 645:435, February 2010.
- [Man81] E. H. Mansfield. Gravity-Induced Wrinkle Lines in Vertical Membranes. Proceedings of the Royal Society A: Mathematical, Physical and Engineering Sciences, 375(1762):307–325, 1981.
- [MBL10] L Mahadevan, R Bendick, and Haiyi Liang. Why subduction zones are curved. Tectonics, 29(6):TC6002, 2010.
- [MH82] Peter A Monkewitz and Patrick Huerre. Influence of the velocity ratio on the spatial instability of mixing layers. Physics of Fluids, 25(7):1137, 1982.
- [MH86] R. Mark and P. Hutchinson. On the structure of the Roman Patheon. The Art Bulletin, 1986.
- [MK99] L. Mahadevan and Joseph B. Keller. Periodic Folding of Thin Sheets. SIAM Review, 41(1):115–131, January 1999.
- [MN87] P. A. Monkewitz and L. N. Nguyen. Absolute instability in the near-wake of two-dimensional bluff bodies. Journal of Fluids and Structures, 1(2):165–184, April 1987.

- [NAM<sup>+</sup>03] Bernd R. Noack, Konstantin Afanasiev, Marek Morzyski, Gilead Tadmor, and Frank Thiele. A hierarchy of low-dimensional models for the transient and post-transient cylinder wake. Journal of Fluid Mechanics, 497:335–363, December 2003.
- [NRCH11] Vishal Nayyar, K. Ravi-Chandar, and Rui Huang. Stretch-induced stress patterns and wrinkles in hyperelastic thin sheets. International Journal of Solids and Structures, 48(25-26):3471–3483, December 2011.
- [OILW08] K. B. Ø lgaard, Anders Logg, and G. N. Wells. Automated code generation for discontinuous galerkin methods. SIAM Journal on Scientific Computing, 31(2):849–864, 2008.
- [PAB11] G. Pfingstag, B. Audoly, and A. Boudaoud. Linear and nonlinear stability of floating viscous sheets. Journal of Fluid Mechanics, 683:112–148, 2011.
- [PBC06] Suzie Protière, Arezki Boudaoud, and Yves Couder. Particlewave association on a fluid interface. Journal of Fluid Mechanics, 554:85, 2006.
- [PDF11] Eric Puntel, Luca Deseri, and Eliot Fried. Wrinkling of a Stretched Thin Sheet. Journal of Elasticity, 105(1-2):137–170, 2011.
- [PH01] Benoît Pier and Patrick Huerre. Nonlinear self-sustained structures and fronts in spatially developing wake flows. Journal of Fluid Mechanics, 435:145–174, 2001.
- [Pie02] Benoît Pier. On the frequency selection of finite-amplitude vortex shedding in the cylinder wake. Journal of Fluid Mechanics, 458:407–417, May 2002.
- [Pop03] Stéphane Popinet. Gerris: A tree-based adaptive solver for the incompressible Euler equations in complex geometries. Journal of Computational Physics, 190(2):572–600, 2003.
- [Ram63] Hans Ramberg. Fluid dynamics of viscous buckling applicable to folding of layered rocks. AAPG Bulletin, 47(3):484–505, March 1963.
- [Rib02] Neil M. Ribe. A general theory for the dynamics of thin viscous sheets. Journal of Fluid Mechanics, 457:255–283, April 2002.
- [Rib04] Neil M. Ribe. Coiling of viscous jets. Proceedings of the Royal Society A: Mathematical, Physical and Engineering Sciences, 460(2051):3223–3239, 2004.
- [Rib08] Neil M. Ribe. Linearized model for a falling viscous curtain. 2008.
- [Rib12] Neil M. Ribe. All bent out of shape: buckling of sheared fluid layers. Journal of Fluid Mechanics, 694:1–4, February 2012.
- [RP09] Yves Renard and Julien Pommier. Description of finite element and integration methods 2009.
- [RQ12] Christian Ruyer-Quil. Instabilities and modeling of falling film flows. Technical report, 2012.

- [RQK12] Christian Ruyer-Quil and Serafim Kalliadasis. Wavy regimes of film flow down a fiber. Physical Review E, 85(4):1–51, October 2012.
- [RSRvdH07] Neil M. Ribe, E. Stutzmann, Y. Ren, and R. van der Hilst. Buckling instabilities of subducted lithosphere beneath the transition zone. Earth and Planetary Science Letters, 254(1–2):173–179, 2007.
- [Rus08] Torgeir Rusten. Chapter: 6. In The Finite Element Method in Solid Mechanics II. 2008.
- [SGB<sup>+</sup>10] E Sizova, T Gerya, M Brown, L. L. Perchuk, and L L Perchu. Subduction styles in the Precambrian: Insight from numerical experiments. Lithos, 116(3-4):209–229, 2010.
- [SH01] Peter J. Schmid and Dan S. Henningson. Stability and Transition in Shear Flows, volume 142. Springer, 2001.
- [Shu09] Chi-Wang Shu. Discontinuous Galerkin Methods: General Approach and Stability. In Numerical solution of partial differential equations, pages 149–202. 2009.
- [SL07] Denis Sipp and Anton Lebedev. Global stability of base and mean flows: a general approach and its applications to cylinder and open cavity flows. Journal of Fluid Mechanics, 593:333–358, November 2007.
- [SM81] Shawqi M Suleiman and Bruce R Munson. Viscous buckling of thin fluid layers. Physics of Fluids, 24(1):1–5, 1981.
- [SM07] M Skorobogatiy and L Mahadevan. Folding of viscous sheets and filaments. Europhysics Letters (EPL), 52(5):532–538, 2007.
- [SS88] J Storch and G Strang. Paradox lost: natural boundary conditions in the ritz-galerkin method. International Journal for Numerical Methods in Engineering, 2(November 1987):2255–2266, 1988.
- [STM12] Anja C. Slim, Jeremy Teichman, and L. Mahadevan. Buckling of a thin-layer Couette flow. Journal of Fluid Mechanics, 694:5–28, 2012.
- [Tay58] G. I. Taylor. The Scientific Papers of Sir geoffrey ingram taylor. Cambridge University Press, 1958.
- [The03] Vassilios Theofilis. Advances in global linear instability analysis of non-parallel and three-dimensional flows. Progress in Aerospace Sciences, 39(4):249–315, May 2003.
- [The11] Vassilios Theofilis. Global Linear Instability. Annual Review of Fluid Mechanics, 43(1):319–352, January 2011.
- [THRS06] M. C. Thompson, K. Hourigan, K. Ryan, and G. J. Sheard. Wake transition of two-dimensional cylinders and axisymmetric bluff bodies. Journal of Fluids and Structures, 22(6-7):793–806, 2006.
- [TW07] B. Thiria and J. E. Wesfreid. Stability properties of forced wakes. Journal of Fluid Mechanics, 579:137, May 2007.

- [TYR93] B. Tchavdarov, A. L. Yarin, and S. Radev. Buckling of thin liquid jets. Journal of Fluid Mechanics, 253:593, 1993.
- [WD07] Garth N Wells and Nguyen Tien Dung. A C0 discontinuous Galerkin formulation for Kirchhoff plates. Computer Methods in Applied Mechanics and Engineering, 196(35-36):3370–3380, 2007.
- [XS08] Yan Xu and Chi-Wang Shu. A Local Discontinuous Galerkin Method for the CamassaHolm Equation. SIAM Journal on Numerical Analysis, 46(4):1998–2021, 2008.
- [YS02] Jue Yan and Chi-Wang Shu. Local Discontinuous Galerkin Methods for Partial Differential Equations with Higher Order Derivatives. Journal of Scientific Computing, 17(1-4):27–47, 2002.
- [Zhe09] Ling Zheng. Wrinkling of Dielectric Elastomer Membranes. PhD thesis, 2009.

